First Principles Studies of Semiconductor Epitaxial Growth

Thesis by

Bao-Liang Tsai

In Partial Fulfillment of the Requirements

for the Degree of

Doctor of Philosophy

California Institute of Technology

Pasadena, California

1997

(Submitted June 2, 1997)

To My Parents

Acknowledgements

I would like to thank first my advisor Bill Goddard for his guidance and support during my many years here at Caltech. He has truly been an inspiration to me in the quest for science ever since I took his Chem 120 class in my first year. I feel extremely lucky having him as my thesis advisor. I am also very grateful to his wonderful secretary Debbie Chester for making my life as a graduate student much easier.

Caltech is a place where great people gather. I will always remember the friends I made in the Goddard group and on campus. I have enjoyed discussing research with Ching-Hwa Kiang, Changmoon Park, and Naoki Karasawa. Thanks especially to Woh-Jer Lee, Wen-Ching Wang, and Michael Werner for helping me walk through the many difficulties in life. They are the people I owe a lot to.

Finally I would like to thank Jenna Zinck of Hughes Research Labs, along with Frank and Paula Grunthaner of JPL for providing such challenging and intellectually rewarding projects for my thesis work. They have been of great help in offering advice and insight for my research during the many meetings I had with them.

Thesis Abstract

This thesis conducts investigations mainly on the structures, energetics, and recations of semiconductor as well as oxide surfaces using first principles cluster model approach.

The first part of the research work addresses the issues in the epitaxial growth of $Hg_{1-x}Cd_xTe$ (MCT) materials. Hg divalent compounds were studied thoroughly using a variety of quantum chemical methods in order to understand the energetics of Hg precursors for growth. The (001) growth surfaces were then examined in detail using cluster model calculations. Based on these results, a novel metal-organic molecular beam epitaxial (MOMBE) growth strategy with favorable energetics for growing MCT using $H_2C{=}CH{-}CH_2{-}Hg{-}C{\equiv}C{-}CH_3$ is proposed. It is hoped that with this new growth strategy, the Hg vacancy and p-doping problems that currently exist in growth can be avoided.

The second part of the thesis discusses the molecular beam epitaxial (MBE) growth of cubic GaN on the (001) surface using various N sources. Surface reconstructions and the interactions of gas-phase atomic and molecular nitrogens with the surface were elucidated using cluster models. Using these results an energy phase diagram for the growth of GaN has been constructed. It suggests that excited state molecular N_2 ($^3\Sigma_u^+$) is the most favorable of all N species for growth of high quality GaN because it can undergo a dissociative chemisorption process. Ground state atomic N (^4S) is also good for growth. The doublet excited states N (^2D and ^2P) might cause surface N abstraction, leading to N vacancies in the material.

Finally, a $Fe(OH)_3(H_2O)_3$ GVB cluster model of crystalline $\alpha{-}Fe_2O_3$ was developed. This simple model can describe the local geometry and bonding of Fe in the bulk oxide. Using quantum mechanical calculations, the orientation of the oleic imidazoline (OI) molecule bonding to the oxide surface has been determined.

OI class of molecules are used extensively for corrosion inhibitor in oil field pipeline applications. It is found in this work that OI can make very strong bonding to the Fe of the iron oxide. In aqueous environments they can replace water on the pipe surface to form a protective layer to prevent corrosion.

Table of Contents

Part I

First Principles Studies of $Hg_{1-x}Cd_xTe$ Epitaxial Growth

Chapter I

Brief Review of Epitaxial $Hg_{1-x}Cd_xTe$ Growth

Abstract

This chapter presents a brief overview of available epitaxial growth techniques available for growing $Hg_{1-x}Cd_xTe$ materials. The current obstacles encountered in growth and the possible causes of these problems are discussed. A theoretical approach to understand the growth process and to address the growth problems is also outlined.

I.1 Introduction

Mercury cadmium telluride $Hg_{1-x}Cd_xTe$ (MCT) materials have been of great industrial interest for the last thirty years because of their dominating presence in the field of infrared device applications.[1] $Hg_{1-x}Cd_xTe$ (where $x = 0 \sim 1$) is a compositionally uniform ternary semiconductor made from combination of $HgTe$ and $CdTe$ binary alloys. When x increases from 0 to 1, it exhibits a transition from a semi-metallic behavior in $HgTe$ to a semiconducting behavior in $CdTe$. The bandgap can be readily tuned over the spectral range of $0.8 \sim 30\mu m$ by changing the alloy composition. Most applications for infrared imaging sensors and focal plane arrays are in the $3 \sim 5\ \mu m$ and $8 \sim 14\ \mu m$ regimes, corresponding to $x = 0.3$ and 0.2, respectively.

The majority of MCT device applications are very demanding from the material point of view. The realization of such devices depends on the ability to grow high-quality material in controllable conditions. The major issues associated with device applications have been materials and process related. In order for these optoelectronic devices to perform properly, they require high crystal quality, good compositional control, low defect density, and reproducible electrical properties in the material. In addition to the requirements mentioned above, the fabrication of devices usually involves growing thin layers of different materials on top of one another. Compositionally uniform epilayers of MCT can be grown by sequentially epitaxial addition of alternate $HgTe$ and $CdTe$ layers under the optimum growth conditions for the respective binaries, followed by diffusion in the interdiffused multilayered process (IMP)[2] at elevated temperatures. A range of gas-phase epitaxial growth techniques have been developed to grow such layers. These include molecular beam epitaxy (MBE), metal-organic chemical vapor deposition (MOCVD), metal-organic vapor phase epitaxy (MOVPE), and metal-organic molecular beam epitaxy (MOMBE). The major distinction among these four techniques, as indicated by

the word "metal-organic," is that MBE utilizes elemental source to grow thin films while the other three methods adopt the organometallic source approach. Each technique has its own advantages and disadvantages. They are briefly reviewed as followed.

I.2 MBE Growth of $Hg_{1-x}Cd_xTe$

Since the first demonstration of the MBE growth of MCT by Faurie and Million in 1981,[3] MBE has become the most extensively used technique to grow high-quality abrupt heterojunctions and advanced device structures for MCT.[4] MBE normally operates under ultra-high vacuum (UHV) conditions in order to eliminate gas-phase side reactions and make the deposition process clean and straightforward. MBE uses atomic or molecular elemental sources obtained from evaporation of elements in thermal effusion cells. Therefore it is able to grow materials at low temperatures ($< 200°C$) so as to minimize the interdiffusion at the interface, making it the only growth technique capable of producing MCT superlattice and multi-quantum well device structures. Low growth temperatures also improve the control of stoichiometry in the grown layers and reduce uncontrolled vacancy doping with metal sublattices. Despite its success, however, MBE has a few fundamental limitations also because of the fact that elemental sources are used.

The intrinsic problem brought about by the evaporation of solid elements to obtain source materials is that one has little control over source specifications, flux regulation and stability, and source reproducibility. These requirements are crucial throughout the growth process for obtaining MCT layers with a high degree of compositional uniformity. Group IIB elements are evaporated as individual atoms whereas for the Group VI element Te polyatomic molecules are always found in the gas phase. Thermal evaporation alone is unable to produce monomer Te species. The dominant product is dimer Te_2, which is difficult to effectively incorporate into the growth surface. Although high temperature cracking furnaces are often used to

decompose dimer Te_2 into monomer Te before entering the growth chamber, this procedure requires very high temperatures ($\sim 3000K$).[5] These high temperatures are not desirable for MBE because of deleterious outgasing and significant radiative heating of the substrate surface. Another serious limitation of MBE is that when the source material depletes, the growth has to be interrupted, waiting for the growth chamber to be opened and the source to be replenished. The UHV condition is normally destroyed during the process. This greatly undermines the consistency and integrity of the thin film grown.

Additionally, the very low sticking coefficient (on the order of 10^{-3}) of elemental Hg to the growing film requires Hg beam flux about 1000 times that of the Cd and Te_2 beams, which can often cause high dislocation densities and twinning.[6] Even with such a high flux, the as-grown material often leads to a significant concentration of Hg vacancies, requiring after-growth annealing at high temperatures ($\sim 300°C$) under substantial Hg overpressure ($\sim 10^{-4}$ Torr) conditions for $15 \sim 20$ hours in order to remove Hg vacancies and maintain the desired stoichiometry and electronic property in the film. This may lead to interfaces between layers of different x that are not sufficiently sharp to attain maximum device performance. Furthermore, p-doped materials usually have a considerable compensation (about a factor or two) problem, probably because the presence of Hg vacancies during growth leads to the p-type dopant (normally As) incorporating into Hg sites rather than the desired Te sites ($\frac{1}{4}$ of the As on the Hg sites would lead to 50% compensation). This makes it difficult to form high quality p-type materials. Even though Hg vacancies themselves are electronically active and exhibit p-type characteristics, they however are not good p-type dopant because these vacancies diffuse easily within the lattice, undermining the reliability of devices.

I.3 MOCVD, MOVPE, and MOMBE Growth of $Hg_{1-x}Cd_xTe$

Because of the growth limitations encountered in MBE, it is obvious that

using gaseous organometallic precursors as source materials would be an attractive alternative to MBE since it can circumvent many of the problems that MBE has. The use of gaseous sources allows flow fluxes to be precisely and reproducibly controlled and monitored. The chemical species that reach the growth surface are well defined and their supply is continuous and unlimited. Furthermore, it also provides the ability for one to chemically "tailor" the characteristics of the organometallic precursors so as to modify growth kinetics via surface chemical processes to achieve optimal results.

Since the pioneer work of Manasevit and Simpson (1971)[7] in growing $CdTe$ with organometallic molecules, epitaxial growth techniques utilizing organometallic sources (mainly MOCVD, MOVPE, and MOMBE) have shown great success in growing MCT materials. Each of the three approaches nevertheless operates under a slightly different condition, and has its own growth characteristics and applications. They are discussed below.

I.3.1 Metal-organic Chemical Vapor Deposition (MOCVD)

In the process of MOCVD,[8] vapors of organometallic compounds are introduced to the growth chamber and then pyrolyzed on or in close proximity to a heated substrate to form deposition layers. The actual decomposition mechanism and pathway are rarely understood because of the complex gas-gas and gas-surface reactions involved. While the deposited material is often amorphous or polycrystalline in MOCVD, because of its simplicity, low cost, mild operating conditions, and the possibility of large scale processing, MOCVD can be considered the most cost-effective method for the growth of MCT epitaxial films. A typical MOCVD growth of MCT uses dimethycadmium (DMCd), diethyltelluride (DETe) and elemental mercury as precursors. Elemental mercury is used because organomercury compounds are of great safety concern since they are often hazardous and very stable. A typical growth temperature of approximately $400 \sim 420°C$ is required for

MOCVD.

I.3.2 Metal-organic Vapor Phase Epitaxy (MOVPE)

The distinction between MOVPE and MOCVD has been blurred or even become non-existent in the literature over the years because there are too many similarities between these two. Strictly speaking, in MOVPE growth organometallic precursors are brought into the growth chamber gradually with an inert carrier gas (normally H_2 or He). This way gas-phase reactions are largely eliminated to simplify surface growth kinetics. In addition, unlike MOCVD, single crystalline materials can be grown with MOVPE because a substrate crystal is used to orient the growing layer so that it adopts the same crystal structure of the substrate. Common metal alkyls and elemental Hg are used for growth in MOVPE, as in the case of MOCVD.

I.3.3 Metal-organic Molecular Beam Epitaxy (MOMBE)

MOMBE is a relatively new vapor phase growth technique for growing single crystal materials,[9] and can be regarded as a hybrid technique between MBE and MOVPE. It adopts the ultra-high vacuum environment of conventional MBE, which has the advantage of growing precise and advanced device structures. Coupled with the use of organometallic gaseous sources, it circumvents the limitations of solid source MBE and provides the chemical diversity and flexibility in growth kinetics. Since there is no complication coming from gas-phase reactions, MOMBE is especially suitable for the studying of surface growth mechanism because of the good control over the chemical growth species. With the proper selection of precursor molecules, MOMBE has the potential to replace MBE in growing high-quality semiconductor heterojunctions and superlattices.

I.4 Current Obstacles in $Hg_{1-x}Cd_xTe$ Growth

Even with the various growth techniques available, growing MCT materials are still plagued with many practical difficulties. The above mentioned Hg vacancy and p-doping problems exist among all techniques and are mainly due to the elemental Hg used. It was hoped that with MOMBE's flexibility on choices of precursors, many of the obstacles would be overcome. Unfortunately, current precursors do not fully exploit the advantage. The surface cracking of commercially available precursor compounds is inefficient at the MCT growth temperatures of $200 \sim 400°C$. Consequently, MOMBE reagents for growing MCT are typically pre-cracked prior to impinging upon the growth surface,[10] resulting in growth kinetics that are similar to the MBE case.

I.5 Overview of Research Work

In order to gain a better understanding of $Hg_{1-x}Cd_xTe$ epitaxial growth and to address the growth problems, first principles molecular orbital study of the growth chemistry was conducted. The goal is to develop new molecular precursors and growth strategies for MCT. Since most of the problems appear to be Hg related, extensive calculations were done on Hg compounds and other related Group IIB compounds. The results are detailed in Appendix B and Chapter II. In Chapter III, MCT semiconductor surfaces and growth mechanism were studies using cluster models. A novel MOMBE growth strategy was also proposed.

Chapter I References

1. R. D. Feldman, D. Lee, A. Partovi, R. P. Stanley, A. M. Johnson, A. M. Glass, and J. Hegarty, *Crit. Rev. Solid State Mater. Sci.* **16**, 477 (1992).
2. D. D. Edwall, J. Bajaj, and E. R. Gertner, *J. Vac. Sci. Technol.* **A8**, 1045 (1990).
3. J. P. Faurie and A. Million, *J. Crystal. Growth* **54**, 582 (1981).
4. V. S. Varavin, S. A. Dvoretsky, V. I. Liberman, N. N. Mikhailov, Y. G. Sidorov. *J. Crystal. Growth* **159**, 1161 (1996).
5. K. C. Mills, *Thermodynamic Data for Inorganic Sulphides, Selenides, and Tellurides* , London: Butterworth, (1974).
6. A. Million, I. DiCioccio, J. P. Galliard, and J. Piaguat, *J. Vac. Sci. Technol.* **6**, 2813 (1988).
7. H. M. Manasevit and W. I. Simpson, *J. Electrochem. Soc* **118**, 647 (1971).
8. P. Capper, P. A. C. Whiffin, B. C. Easton, C. D. Maxey, and I. Kenworthy, *Mater. Lett.* **6**, 356 (1988).
9. C. K. Tu, H. K. Doug, and N. Y. Li, *Mater. Chem. Phys.* **40**(12), 260 (1995).
10. D. Rajavel and J. J. Zinck, *J. Electronic Mater.* **22**, 803 (1993).

Chapter II

Quantum Chemical Studies of Hg Divalent Compounds

Abstract

In this chapter the results of our investigation on the energetics of Hg divalent compounds using a variety of quantum chemical methods are reported. We have evaluated the performances of these methods and basis set effects. The QCISD(T) method coupled with TZDP basis and a 20-valence-electron effective core potential (ECP) for Hg are found to enable the accurate reproduction of experimental geometries and bond energies. Based on these results, group additivity parameters for Hg have been developed for estimating the heats of formation of organomercury compounds.

II.1 Introduction

The linear arrangement of two ligands bonded to one central atom is the most common form of coordination found in Group IIB (Zn, Cd, Hg) gas-phase compounds because of the ns^2 valence configuration of Group IIB. This linear coordination of two is especially predominant in the chemistry of mercury than for zinc, cadmium, or any other element. The main reason is due to the relativistic stabilization of the Hg $6s$ orbital, which reduces the charge separation in the intermolecular interactions between HgX_2 molecules containing electronegative substituents X.[1] Relativistic effects also account for the fact that mercury is the only liquid metal at ambient temperatures and has unique metallic properities.[2]

Understanding the energetics involved in the metal-organic growth process of $Hg_{1-x}Cd_xTe$ can lead to optimization of growth parameters and improvement of material quality. A thermodynamic analysis of the precursor compounds should provide useful information with respect to the selection of appropriate precursors and chemical reaction pathways. The knowledge of accurate bond dissociation energies of precursor compounds is therefore consequential. Although experiment can give accurate heats of formation for a variety of systems, it is often difficult to measure individual bond energies, especially when there are unstable radical species involved in the bond-breaking process. While *ab initio* calculations provide an attractive alternative to experiment, high level of theories and extensive one-particle basis sets are required in order to achieve energies with chemical accuracy (within 1 $\sim$ 2 kcal/mol). The greater the electron correlation treatment and the basis set, the more expensive (requiring more computational resources) the calculation becomes, making the study of complex systems very difficult or even impossible. Therefore the objective here is not only to understand the energetics of Hg compounds, but also to find out what level of calculation leads to energies with satisfactory accuracy while maintaining computational feasibility. This aspect

is especially important when we move forward to study gas-surface reactions using large surface cluster models (Chapter III), where high-accuracy methods are simply too expensive to be applicable and a reasonably "compromised" method has to be used.

This chapter is devoted to examining the electronic structures and the nature of metal-ligand bonding of Group IIB (mainly, Hg) divalent compounds. A measure of the performance of various quantum chemical approximations will also be investigated. In the end applications based on the calculation results will be discussed.

II.2 Computational methods

Calculations were based on various levels of *ab initio* theoretical methods including Hartree-Fock (HF),[3] Møller-Plesset second order (MP2),[4] quadratic configuration interaction singles and doubles with triples perturbation (QCISD(T)),[5,6] and coupled cluster singles plus doubles with triples perturbation (CCSD(T)).[7] Density functional theory (DFT)[8] approximation was also used. During calculations the core electrons of Hg atom are represented by effective core potentials (ECP).[9] Two sets of ECP's were used for Hg: one includes the inner s and p shell electrons in the ECP (68-electron core); the other does not (60-electron core). Both sets of ECP's contain relativistic effects. Basis sets with various sizes were used in order to study their accuracies. The specific details of calculations are described in Appendix A. All calculations have been performed using Gaussian 92/DFT program package.[10]

II.3 Calculations of HgX and HgX_2 Compounds

The goal of the calculation here is to understand the energetics of Hg compounds. In addition, we also hope to be able to select an appropriate theoretical tool to study large systems containing Hg so that the issues of MCT growth can be addressed. Therefore molecular properties of simple HgX and HgX_2 ($X = H, F, Cl$)

compounds, for which good experimental data are available, were calculated with various quantum chemical methods and basis set/ECP schemes to evaluate different computational approaches. These methods range from primitive HF to sophisticated configuration interaction (CI). The basis sets used vary from concise double-zeta (DZ) to extensive triple-zeta double polarization (TZDP). Please refer to Appendix A for detailed description of basis sets and ECP's used since hereafter they will only be represented by denotations.

II.3.1 Geometry Optimization

Geometry optimization calculations were carried out at various theoretical levels. No f polarization functions were used on Hg in the calculations because the current version Gaussian program does not compute energy gradients with the presence of f functions. It has been found by Bencini *et al.*[11] that the inclusion of f functions reduces the calculated bond distances by $\sim$ 1 percent due to angular correlation of the mercury $5d$ shell.

II.3.1.1 Geometries of HgX Compounds

Table II.1 summarizes the $Hg-X$ bond distances of HgX compounds obtained at various theoretical levels. The bond distances calculated with $[Xe4f^{14}]$-core ($Q_{Hg} = 12$) pseudopotentials and DZ basis sets (12A and 12B) are generally too large compared to the experimental bond distances. The added d polarization function for the non-metal in 12B did shorten the bond by 0.3 $\sim$ 0.7 Å, leading to a better experimental agreement than for 12A. For 12A and 12B, electron correlation actually increases the calculated bond distances except for MP2, which overall leads to shorter bond distances. QCISD(T) and CCSD(T) show compatible results as expected. The triples perturbation only has slight effect on the bond length. The B3LYP/DFT method greatly overestimates bond distances as much as 0.17 Å in HgH. With the better basis 12B, MP2 appears to have the best agreement with

Table II.1. Calculated and Experimental Bond Distances (Å) for HgX

Method	$Hg-H$	$Hg-F$	$Hg-Cl$
HF/12A	1.814	2.085	2.494
MP2/12A	1.828	2.102	2.489
QCISD/12A	1.885	2.117	2.516
QCISD(T)/12A	1.892	2.121	2.520
CCSD/12A	1.886	2.117	2.516
CCSD(T)/12A	1.891	2.120	2.520
B3LYP/12A	1.977	2.175	2.578
HF/12B	1.793	2.026	2.448
MP2/12B	1.767	2.025	2.431
QCISD/12B	1.807	2.036	2.454
QCISD(T)/12B	1.814	2.039	2.462
CCSD/12B	1.809	2.034	2.457
CCSD(T)/12B	1.813	2.038	2.462
B3LYP/12B	1.964	2.118	2.568
HF/20A	1.772	2.051	2.426
MP2/20A	1.712	2.047	2.390
QCISD(T)/20A	1.735	2.051	2.410
CCSD(T)/20A	1.736	2.049	2.413
B3LYP/20A	1.798	2.117	2.438
HF/20B	1.761	2.039	2.424
MP2/20B	1.693	2.036	2.389
QCISD(T)/20B	1.718	2.044	2.415
CCSD(T)/20B	1.718	2.042	2.416
B3LYP/20B	1.776	2.106	2.483
exptl[12]	1.725	–	2.42

experiment among all, including high-level CI methods. This is probably due to cancellation of errors caused by the inadequacy of MP2 theory and basis sets.

With the combinations of $[Kr4d^{10}4f^{14}]$-core ($Q_{Hg} = 20$) pseudopotentials and more extensive TZ basis sets, 20A and 20B, the calculated bond distances are generally shorter and in better agreement with experiment. The results from QCISD(T) and CCSD(T) calculations are almost identical, and are within 0.01Å of experimental values. Of all the methods MP2 consistently gives the shortest bond lengths while B3LYP always overestimates them. Unlike in the 12A and 12B calculations, electron correlation here has shortened bond distances and reduced computational errors to agree better with experiment. This demonstrates that the effect of CI on the calculation result not only depends on the theory itself, it also has a great deal to do with the particular basis set or pseudopotential used. Sometimes it would be tempting to ascribe certain computational result to electron correlation based simply on a few calculations. Cautions have to be taken to eliminate the basis set and pseudopotential factors that often are interrelated with the theoretical method and thus obscure the result. In this case, it appears that the Hg core-valence correlation coming from the outer-core ($5s$ and $5p$) electrons plays a significant role in bond lengths. When these electrons are included in the active space (as in 20A and 20B), the high-level CI methods no longer behave erroneously as in the case of 12A and 12B, and the accuracy greatly improves.

II.3.1.2 Geometries of HgX_2 Compounds

The calculated geometries and available experimental data for HgX_2 compounds are listed in Table II.2. High-level methods such as QCISD(T) and CCSD(T) were not used since their calculations for geometry optimization would be too expensive even for simple HgX_2 compounds, making these methods unsuitable for calculating larger organomercury molecules later on in this chapter. Only the HF, MP2, and B3LYP methods are evaluated here. The bond distances obtained

Table II.2. Calculated and Experimental Bond Distances (Å) for HgX_2 at $D_{\infty v}$ symmetry

Method	HgH_2	HgF_2	$HgCl_2$
HF/12A	1.698	1.993	2.379
MP2/12A	1.712	2.022	2.381
B3LYP/12A	1.768	2.033	2.440
HF/12B	1.696	1.940	2.335
MP2/12B	1.701	1.951	2.327
B3LYP/12B	1.766	1.999	2.401
HF/20A	1.676	1.949	2.312
MP2/20A	1.646	1.958	2.286
B3LYP/20A	1.669	1.969	2.313
HF/20B	1.661	1.933	2.305
MP2/20B	1.633	1.944	2.283
B3LYP/20B	1.655	1.956	2.309
exptl[13]	–	1.96	2.27

from 12A and 12B are generally still too large although the inclusion of d functions in 12B did help reduce the errors. With 20A and 20B the calculated bond lengths shorten as in the case of HgX compounds. All three methods, especially MP2, give good agreement with experiment. The use of more extended basis sets (20B) does not necessarily improve the overall accuracy. At every level of basis set, B3LYP performs much better in HgX_2 than in HgX compounds where bond lengths are calculated to be too large. This may be due to the inability of B3LYP to handle open-shell radical compounds well because the B3LYP parameters were obtained from stable organic compounds.

From the calculations of HgX and HgX_2, we can conclude that larger basis sets and more sophisticated electron correlation procedures coupled with a larger valence space (more active electrons) are necessary for obtaining the correct shorter bond distances. For the current case, good bond distance results can be obtained at the MP2/20A level. This finding is important for the present study as later on we will be investigating larger organomercury compounds. The size of these compounds do not allow for the use of large-scale configuration interaction or couple-cluster methods for structure optimizations. For the following bond energy calculations, the MP2/20A geometries will be used in all cases.

II.3.2 Bond Energy Calculation

For the linear divalent MX_2 type of compounds, D_1 and D_2 correspond to the first and second bond energies, respectively.

$$M - X \xrightarrow{D_1} M + X \qquad (II.1)$$

$$XM - X \xrightarrow{D_2} XM + X \qquad (II.2)$$

As a measure of the performance of the different approximations, the HgH_2 bond energies were calculated at various combinations of theories and basis/ECP schemes. The MP2/20A optimized geometries were used for all energy calculations. The calculated and experimental bond energies are listed in Table II.3. Since there is no experimental data available for D_2, and the D_2 result from the best level of current calculation (CCSD(T)/20B) is used as a reference to evaluate the various methods. The HF method performs very poorly in the energy result as can be expected. Even with the use of high-quality TZDP basis set and 20-valence-core ECP, very little improvement is shown. This result manifests HF's problematic nature of lacking dynamic electron correlation when calculating energetics. For all electron correlation methods, the inclusion of outer-core electrons (as in 20A and

Table II.3. Calculated[a,b] and Experimental Bond Energies (kcal/mol) for the HgH_2 Compound

Method	D_1	D_2	$D = D_1 + D_2$
HF/12B(f)	6.35 (7.68)	53.21 (54.36)	59.56 (62.04)
MP2/12B(f)	5.53 (-4.61)	66.94 (62.48)	72.47 (57.87)
QCISD(T)/12B(f)	5.50 (1.66)	67.67 (66.13)	73.17 (67.79)
CCSD(T)/12B(f)	5.14 (1.77)	67.73 (66.20)	72.87 (67.97)
B3LYP/12B(f)	5.96 (7.02)	63.47 (63.66)	69.43 (70.68)
HF/20A(2f)	7.94 (9.33)	58.75 (58.71)	66.69 (68.04)
MP2/20A(2f)	16.18 (5.38)	80.27 (77.32)	96.45 (82.70)
QCISD(T)/20A(2f)	16.53 (11.96)	81.52 (78.44)	98.05 (90.40)
CCSD(T)/20A(2f)	16.50 (11.99)	81.53 (78.47)	98.03 (90.46)
B3LYP/20A(2f)	14.64 (16.12)	80.67 (80.31)	95.31 (96.42)
HF/20B(2f)	5.10 (5.45)	57.81 (58.35)	62.91 (63.80)
MP2/20B(2f)	15.09 (2.98)	76.11 (76.65)	91.20 (79.63)
QCISD(T)/20B(2f)	14.25 (9.15)	79.15 (77.90)	93.40 (87.05)
CCSD(T)/20B(2f)	14.25 (9.34)	79.19 (77.76)	93.43 (87.10)
B3LYP/20B(2f)	12.17 (12.62)	78.76 (79.19)	90.93 (91.81)
exptl[14]	10.35	–	–

[a] Energies were calculated with MP2/20A geometries.
[b] Values in parenthesis were calculated with f function(s) on Hg.

20B) gives much better bond energies, indicating again the importance of core-valence correlation for Hg. To make sure that this improvement is indeed due to the core-valence correlation but not the better basis sets used in 20A and 20B, in an independent study, we took the 68-electron core ECP in 12B coupled with a TZDP basis (as in 20A(2f)) to calculate bond energies. The results are very close to those obtained from 12B(f). This would rule out the basis set factor on the energy.

The absence of f polarization functions on Hg significantly overestimates the bond energies calculated at the MP2, QCISD(T), and CCSD(T) levels, indicating contributions from angular correlation. The B3LYP result, on the other hand, is not affected much by the f functions, which is consistent with typical B3LYP calculations on other systems. Given the TZDP basis set and 20-valence-core ECP, MP2 overall gives mediocre to acceptable bond energies. The failure of MP2 in calculating bond energies for many transition metal compounds is well documented and is intimately connected to the involvement of d-orbitals in bonding.[15] B3LYP provides reasonable (better than MP2) energy results at only a fraction of computational cost that MP2 needs. QCISD(T) and CCSD(T) offer very similar results that compare well with experiment, with a slightly less computational time needed for QCISD(T). The more extensive basis set 20B(2f) appears to give smaller bond energies than those from 20A(2f) at every level of calculation.

Table II.4 lists the calculated and experimental bond energies of HgF_2 and $HgCl_2$. Only 20A(2f) and 20B(2f) basis sets were used for the calculation. A better evaluation of each method can be made since more experimental data are available for HgF_2 and $HgCl_2$. HF again shows its severe inadequacy in calculating energies. The error of HF atomization energy ($D_1 + D_2$) for HgF_2 can reach as large as 50 percent in the case of 20B(2f). MP2 generally overestimates the bond energies. Its accuracy gets better when using the larger 20B(2f) basis set, which almost always gives smaller bond energies than for 20A(2f). A comparison between the two different basis sets shows that, for the high-level QCISD(T) and CCSD(T) calculations using 20A(2f), the bond energy results agree excellently well with experiment (within $\sim$ 2 kcal/mol), while the 20B(2f) energies calculated at the same theoretical level are too small compared to 20A(2f) and experimental results. When using 20A(2f), B3LYP shows better results then MP2. In the case of $HgCl_2$, very accurate bond energies were obtained using B3LYP.

Table II.4. 20A(2f)- and 20B(2f)-Calculated[a] and Experimental Bond Energies (kcal/mol) for the HgF_2 and $HgCl_2$ Compounds

Method	D_1	D_2	$D = D_1 + D_2$
		(1) HgF_2	
HF	15.09 [8.15]	54.23 [50.54]	69.32 [58.69]
MP2	34.08 [28.60]	98.55 [95.42]	132.63 [124.02]
QCISD(T)	32.45 [27.38]	92.16 [89.07]	124.61[116.45]
CCSD(T)	32.30 [27.08]	91.96 [88.76]	124.26 [115.84]
B3LYP	35.14 [32.74]	92.85 [84.84]	127.99 [117.58]
exptl[16]	31.17	91.45	122.62
		(2) $HgCl_2$	
HF	23.01 [18.26]	63.74 [59.09]	86.75 [77.35]
MP2	22.74 [18.69]	89.82 [83.85]	112.56 [102.54]
QCISD(T)	23.85 [20.24]	84.00 [79.18]	107.85 [99.42]
CCSD(T)	23.90 [20.26]	83.98 [79.15]	107.88 [99.41]
B3LYP	26.48 [22.49]	81.32 [76.53]	107.79 [99.02]
exptl[17]	25.04	84.03	107.07

[a]Energies were calculated at MP2/20A geometries with both 20A(2f) and 20B(2f). The 20B(2f) values are in square brackets.

Based on the energy calculation results in Table II.3 and II.4, it can be concluded that in order to obtain accurate bond energies, the correlation from the outer-core electrons of Hg has to be included in the calculation (i.e., 20-electron core ECP needs to be used). The combination of QCISD(T) and 20A(2f) basis set seems to be the best among all methods investigated, and is able to provide estimation of bond energies with chemical accuracy. B3LYP performs overall better than MP2 and gives reasonable to good energy results (within 3 $\sim$ 4 kcal/mol).

II.3.3 Basis Set Superposition Error (BSSE) Correction

A well-known problem arising from using finite basis sets in quantum chemical calculations of molecular interactions is the appearance of basis set superposition error (BSSE), which normally leads to overestimated binding energies. BSSE is not a physical phenomenon. It is merely a spurious improvement (in energetic sense) in the description of the electronic structure of the individual monomers within the molecular complex, due to a partial use of the basis orbitals centered on other monomers. Theoretically, BSSE can be avoided by "saturating" the monomer with complete (infinite) basis functions to eliminate basis contributions from other monomers. However, this goal is not practicable in terms of computation, especially for methods accounting for electron correlation.

The most common approach to circumvent BSSE problem is *a posteriori* counterpoise scheme (or called BB scheme) introduced by Boys and Bernardi.[18] To use the BB scheme to correct BSSE in $Hg-X$ bond energies, the interaction energy between Hg and X is computed as the difference between the energy of the "supermolecule" HgX, E_{HgX}, and those of the monomer (E_{Hg} and E_X) calculated by using the whole supermolecule basis:

$$\Delta E^{BB} = E_{HgX}(HgX) - E_{Hg}(HgX) - E_X(HgX) \qquad (II.3)$$

Here the basis set used is indicated in parentheses. It is hoped that through this procedure the contamination energy from the monomer can be removed from the interaction energy. Table II.5 shows the BSSE corrected bond energies. These energies appear to be too small compared to experimental values. It is a well-documented fact that correlation energy calculations using the BB scheme sometimes tend to over-correct, especially with small or medium basis sets.[19] This is very likely due to the fact that in the supermolecule calculation, the monomers cannot take advantage of the full supermolecule basis as the Pauli principle prevents the monomer from using the occupied orbitals of the partner. From these results we can conclude that

Table II.5. BSSE Correction of Calculated Bond Energies (kcal/mol)

Molecule	D^a	$D_{BB}{}^b$	D_{exptl}
HgH	11.96	8.63	10.10
HgF	32.45	29.00	31.17
$HgCl$	23.85	18.14	25.04

[a] QCISD(T)/20A(2f) bond energy.

[b] BB scheme corrected bond energy.

the effort to remove BSSE is not actually worthwhile (at least in our HgX case) and will not be pursued further in the current work.

II.3.4 Pairing Energy Model

For divalent molecules such as Group IIB linear compounds, the bond dissociation energies usually can be estimated using a very simple model through the concept of ns^2 paring energy. This pairing energy is loosely defined to be the energy required to promote the Group IIB atom from the $(ns)^2$ ground state to the $(ns)^1(np)^1$ excited state configuration with two singly-occupied orbitals in order for the Group IIB atom to participate in molecular bonding. This model assumes that a ligand X bonds to a Group IIB metal with an intrinsic bond dissociation energy D_0, which has a characteristic value for the given X and the metal M. D_0 is not necessarily the observed bond energy because it by definition does not accommodate the paring energy term. Here let us consider an MX_2 compound. D_1 is the first dissociation bond energy as in (II.1). Since breaking the first bond involves relaxing M from the $(ns)^1(np)^1$ state to the $(ns)^2$ ground state (i.e., re-pairing the ns^2 electrons), $D_1 = D_0 - E_p$, where E_p is the pairing energy of M. D_2 is the bond energy observed when breaking the second bond as in (II.2). D_2 is equal to D_0 because no promotional energy is involved when making the second bond. Based

on the analysis above, E_p can therefore be estimated from the difference between the two observed bond energies: $E_p = D_2 - D_1$.

E_p can be a useful quantity for being a characteristic energy of the Group IIB metal regardless of the type of ligand X involved. Once E_p is known for a given M, the two bond dissociation energies of any MX_2 compound can be estimated as long as either one of the two is also known. This model, though simple but if proven accurate, can be very helpful in approximating the energetics for any MX_2 compound when experimental data are not readily available. Using the QCISD(T)/20A(2f) energy results in Table II.3 and II.4, the E_p calculated (from $D_2 - D_1$) for HgH_2 (66.48 kcal/mol) turned out to be different from the E_p for HgF_2 (59.71 kcal/mol) and the E_p for $HgCl_2$ (60.15 kcal/mol). To further test the model, other Group IIB (Zn and Cd) compounds were also investigated. Table II.6 lists the calculated E_p's and energetics of ZnX_2 and CdX_2 compounds. Again the E_p shows certain variation with the ligand X.

The noticeable discrepancy in the calculated E_p suggests that the paring energy model may be over-simplified. E_p is not a constant for a given M and appears to increase as the ionic character of the $M-X$ bond (or the electronegativity of X) decreases. The paring energies calculated from a given Group IIB fluoride and chloride are close in magnitude but are $7 \sim 13$ kcal/mol (depending on the metal) less than the E_p calculated from the corresponding hydride. The variation in E_p resulting from different ligands may be rationalized through the fact that each X has a different affinity toward the ns^2 electrons. From our calculations the result seems to suggest that it takes less energy to un-pair the ns^2 electrons if the ligand X has larger electron affinity (or larger electronegativity).

If we take into account the change in coulomb and exchange energies as a result of bonding of M to the ligand X, the above-mentioned simple pairing energy model can be improved in the following way:

Table II.6. Calculated[a] Bond Energies and $E_p^{'}$ (kcal/mol) of ZnX_2 and $CdX_2(X = H, F, Cl)$ Compounds

Molecule	D_1	D_2	$D_1 + D_2$	$E_p = D_2 - D_1$
ZnH_2	21.61 (21.92)[b]	80.12	101.73	58.51
ZnF_2	65.60	115.95	181.55	50.35
$ZnCl_2$	47.13 (48.98)[b]	97.96	145.09	50.83
CdH_2	18.33 (17.55)[b]	73.99	92.32	55.66
CdF_2	55.41	100.02	155.43	44.61
$CdCl_2$	42.90	90.28	133.18	47.38

[a]Bond Energy were calculated at the QCISD(T)/20B(2f) and QCISD(T)/20A(2f) levels for ZnX_2 and CdX_2, respectively. Please see Appendix A for reasoning.

[b]Values in parenthesis are experimental energies from reference 14.

For the Group IIB ns^2 ground state, we have only one coulomb energy term J_{ss} arising from the coulombic repulsion of the two ns^2 electrons.

$$M: \qquad \underset{s}{\uparrow\downarrow} \qquad \underset{p}{\text{—}}\ \underset{p}{\text{—}}\ \underset{p}{\text{—}} \qquad E_M = J_{ss} \qquad (II.4)$$

When a ligand X is bonded to the sp-hybridized M, the resulting coulomb and exchange energy terms are shown in (II.5).

$$MX: \qquad \underset{sp}{\uparrow\downarrow}\ \underset{sp}{\uparrow} \qquad \underset{p}{\text{—}}\ \underset{p}{\text{—}} \qquad E_{MX} = \frac{J_{ll}}{4} + J_{ll}^{'} - \frac{K_{ll}^{'}}{2} \qquad (II.5)$$

The $\frac{J_{ll}}{4}$ term comes from the two bonding electron pairs in the sp orbital. Since the probability of the two electrons simultaneously present in the metal sp orbital is $\frac{1}{4}$ (assuming $M-X$ is a covalent bond), the coulombic repulsion is only $\frac{1}{4}$ of

J_{ll}. We do not consider here the electronic energy terms for the ligand X because these terms will cancel out on each other in the pairing energy expression as will be demonstrated soon. The $J_{ll}^{'}$ and $\frac{K_{ll}^{'}}{2}$ terms respectively account for the coulomb and exchange energies between the two electron in the two separate *sp* orbitals. Here we denote prime($'$) for terms with interactions between one bonding and one non-bonding orbitals. The $\frac{1}{2}$ factor in the exchange term is due to the fact that the bonding electron only has the same spin of the non-bonding electron half of the time.

When a second X is bonded to M, this would result in a coulomb and exchange energy change of (II.6).

$$MX_2: \quad \underset{sp}{\uparrow\downarrow} \quad \underset{sp}{\uparrow\downarrow} \quad \underset{p}{\text{—}} \quad \underset{p}{\text{—}} \qquad E_{MX_2} = \frac{J_{ll}}{4} + \frac{J_{ll}}{4} + J_{ll}^{''} - \frac{K_{ll}^{''}}{2} \quad (II.6)$$

The two pairs of bonding electrons in the two *sp* orbitals contribute the first two coulomb terms $\frac{J_{ll}}{4}$ in (II.6). The $J_{ll}^{''}$ and $\frac{K_{ll}^{''}}{2}$ terms come from the two M electrons in the two separate *sp* orbitals interacting with each other. We denote double-prime($''$) for terms with interactions between two bonding orbitals.

Now If we express the bond energies of MX_2 in terms of E_p, D_0, coulomb and exchange energies, we get

$$M - X \xrightarrow{D_1} M + X \qquad D_1 = D_0 - E_p + E_M - E_{MX} \qquad (II.7)$$

$$XM - X \xrightarrow{D_2} XM + X \qquad D_2 = D_0 + E_{MX} - E_{MX_2} \qquad (II.8)$$

The observed pairing energy (denoted as $E_p^{'}$) therefore becomes

$$\begin{aligned} E_p^{'} &= D_2 - D_1 \\ &= E_p + 2E_{MX} - E_M - E_{MX_2} \\ &= (E_p - J_{ss}) + (2J_{ll}^{'} - J_{ll}^{''}) + (\frac{K_{ll}^{''}}{2} - K_{ll}^{'}) \qquad (II.9) \\ &\approx (E_p - J_{ss}) + J_{ll}^{'} - \frac{K_{ll}^{''}}{2} \\ &\approx (E_p - J_{ss}) + J_{ll}^{'} \end{aligned}$$

Here we make the assumption that $J'_{ll} = J''_{ll}, K'_{ll} = K''_{ll}$, and $J'_{ll} \gg K'_{ll}$, ending up with $E'_p \approx (E_p - J_{ss}) + J'_{ll}$. The $(E_p - J_{ss})$ term in E'_p is a characteristic of the metal M and is independent of the ligand X. J'_{ll}, on the other hand, is the coulombic repulsion between the electron in the $M-X$ bonding orbital and the electron in the M non-bonding orbital. This quantity should decrease in magnitude when the electron affinity of X increases, as the bonding electron is pulled farther away from M. This would explain the decreasing trend in the observed pairing energy $E'_p(MF_2) < E'_p(MCl_2) < E'_p(MH_2)$ as the electronegativity of X increases $(\chi_F > \chi_{Cl} > \chi_H)$.

Table II.7. Calculated[a] Bond Energies and E'_p (kcal/mol) of the BeX_2 and $MgX_2(X = H, F, Cl)$ Compounds

Molecule	D_1	D_2	$D_1 + D_2$	$E'_p = D_2 - D_1$
BeH_2	47.69	94.96	142.65	47.27
BeF_2	129.21	164.66	293.87	35.45
$BeCl_2$	87.46	128.44	215.9	40.98
MgH_2	31.72	72.16	103.88	40.44
MgF_2	100.75	135.83	236.58	35.08
$MgCl_2$	72.90	109.07	181.97	36.17

[a]Bond energies were calculated at the QCISD(T) level with MP2 geometries.

The above pairing energy analysis can be applied to any MX_2 compound provided that the ground state valence configuration of M is ns^2. Therefore a similar trend should also be observed for Group IIA divalent compounds. *Ab initio* bond energy calculations were carried out for BeX_2 and $MgX_2(X = H, F. Cl)$ compounds and the results are listed in Table II.7. The same pairing energy trend was indeed

found. In these calculations. TZDP quality all-electron basis sets 6-311(2dp)[20] and (10s7p3d/4s3p/2d)[21] were use for Be and Mg, respectively. Basis sets in 20A were used for all non-metals. Even though Ca also has ns^2 configuration, We did not calculate CaX_2 compounds because CaF_2 has been reported experimentally to have a bent structure,[22] which is likely due to the involvement of 3d orbitals in the molecular bonding.[23]

Table II.8. Calculated[a] $E_p^{'}$ of MX_2 $(M = Zn, Cd, Hg, Be, Mg)$ Compounds *vs.* Atomic Excitation Energy of M (in kcal/mol)

Molecule	$E_p^{'}(X = H)$	$E_p^{'}(X = F)$	$E_p^{'}(X = Cl)$	$E_{M(^1S \longrightarrow ^3P)}$
ZnX_2	58.51	50.35	50.83	89.01
CdX_2	55.66	44.61	47.38	82.32
HgX_2	66.48	59.71	60.15	119.91
BeX_2	47.27	35.45	40.98	62.89
MgX_2	40.44	35.08	36.17	59.26

[a] All energies were calculated at the QCISD(T) level.

Since the pairing energy is defined to be the energy needed to un-pair the ns^2 electrons and to enable the Group IIA or IIB element to form bonds in the linear sp configuration, it would therefore be interesting to see how $E_p^{'}$ compares with the atomic excitation energy of M. Table II.8 lists the calculated $E_p^{'}$ and $ns^2 \longrightarrow ns^1np^1$ excitation energy for M $(M = Zn, Cd, Hg, Be, Mg)$. Overall, $E_p^{'}$ amounts to only $50 \sim 60\%$ of the atomic excitation energy. This finding would indicate that the bonding orbital is not purely a sp. Instead, the molecular bonding state is a resonance between the s^2 and sp configurations.

Normally the energy level separation between the valence s and p orbitals for a given M decreases as M goes down along the column of the periodic table.

However, for a heavy element such as mercury, the average velocity for its $1s$ electrons is about 58% of the speed of light. According to Einstein's special relativity theory, the relativistic mass of any moving object $m_{rel} = m_{rest}/\sqrt{1-(v/c)^2}$, which means $m_{rel} = 1.23\ m_{rest}$ for Hg $1s$ electrons. This in turn means that the Bohr radius (based on m_{rest}) shrinks by 23% since the mass of the electron enters in the denominator. Thus the $1s$ orbital in Hg contracts significantly and lower its energy because of being closer to the nuclei. Since all orbitals must be orthogonal to one another, an almost equally large mas-velocity contraction occurs for $2s, 3s, 4s, 5s$, and $6s$ orbitals as well, causing the stabilization of valences s orbital. This is why Hg has a very different chemistry from other Group IIB elements.

The considerably greater $E_{M(^1S \longrightarrow ^3P)}$ (and thus $E_p^{'}$) of Hg than those of Cd and Zn is due to the relativistically stabilized Hg $6s$ orbital. This results in a much smaller D_1 than D_2 for Hg compounds. There is also some degree of relativistic stabilization of the Cd $5s$ orbital, though not to the same extent as of the Hg $6s$ orbital. Consequently the $E_p^{'}$ for Cd is only slightly smaller than Zn since Cd is one row down the periodic table from Zn.

II.4 Mercury–Carbon Bond Energies in Organomercury Compounds

The thermodynamic characterization of $Hg-C$ bonds is of great importance for the understanding the energetics involved in the organometallic growth of MCT. The $M-C$ $(M = Cd, Hg)$ bond energies from various organometallic groups were calculated and are listed in Table II.9. In the case of $M-CH_3$, Hg bonds very weakly to the methyl ligand with a bond energy (5.82 kcal/mol) which is less than half of the $Cd-CH_3$ bond energy (12.10 kcal/mol). This is consistent with the fact that gaseous radical $CdCH_3$ exists,[24] while $HgCH_3$ has never been observed in the gas phase. When the molecular hybridization of the bonding carbon goes for sp^3 to sp, the $M-C$ bond energy increases. This is likely due to the increasing electronegative nature of the carbon when the s contribution becomes larger (s

orbital is more electronegative than p orbital) and thus makes the $M-C$ bond more ionic. Coupled with the better overlap of C_{sp} orbital with the sp orbital of M, the $M-C{\equiv}CH$ and $M-C{\equiv}N$ thus become quite large. In fact, the calculated $Hg-C{\equiv}CH$ bond energy (39.92 kcal/mol) is larger than that of $Hg-F$ bond (32.45 kcal/mol). This calculation result is supported by the abnormally large $Hg-C$ bond energy of bis-phenylethynal mercury, $Hg(C{\equiv}CC_6H_5)_2$, compared to that of bis-benzyl mercury , $Hg(CH_2-C_6H_5)_2$, observed in a combustion study.[25] The strong $Hg-C_{sp}$ bond may provide a possible way to solve some of problems encountered in the MCT epitaxial growth. This will be discussed in detail in Chapter III.

Table II.9. Various Calculated[a] $M-C$ $(M = Cd, Hg)$ Bond Energies (kcal/mol)

$Cd-C$ Bond	D_1	$Hg-C$ Bond	D_1
$Cd-CH_3$	12.10	$Hg-CH_3$	5.82
$Cd-C_2H_5$	7.03	$Hg-C_2H_5$	unbound
$Cd-CH{=}CH_2$	18.16	$Hg-CH{=}CH_2$	11.59
$Cd-C{\equiv}CH$	47.67	$Hg-C{\equiv}CH$	39.92
$Cd-C{\equiv}N$	44.37	$Hg-C{\equiv}N$	38.66

[a]Energies were calculated at the QCISD(T)/20A(2f) level with MP2 geometries.

II.5 Group Additivity Values for Mercury Compounds

Since its introduction by S. W. Benson almost 40 years ago,[26] the group additivity scheme has remained to be one of the most useful tools for estimating heats of formation of organic compounds. The idea here is that by characterizing each atom in terms of the atoms it is bonded to (and which order of bond) and assigning it a group value, one can develop an additive scheme to accurately predict ΔH_f°. These group values, however, have so far been limited to being derived from

experimental heats of formation data. The existence of these data is not always abundant, especially for organometallic compounds. The availability of different ways to derive the group values would be of great importance in extending the usefulness of group additivity scheme. In this regard, precise quantum chemical calculations should be an attractive alternative method from which ΔH_f° can be obtained.

In choosing organomercury compounds as precursors for MCT growth, it would be very useful to have an additive scheme for these compounds so that the growth energetics can be worked out as a preliminary screening for suitable Hg compounds. Since high-level calculations have been carried out on various Hg compounds and the results are of satisfactory accuracy, groups values for Hg-containing molecules can also be developed based on these results.

In order for quantum chemical calculation results to be applied to the prediction of the enthalpy of a reaction $A+B \longrightarrow AB$, $\Delta H(AB)$, a few considerations need to be addressed first. The $-\Delta H(AB)$ in this case is the bond dissociation energy $D(A-B)$ needed for molecular AB to break into two fragments A and B. The "bond energy" $D_e(A-B)$ calculated theoretically, however, is just the electronic energy difference

$$D_e(A-B) = E_e(A) + E_e(B) - E_e(AB), \qquad (II.10)$$

while the bond dissociation energy

$$D(A-B) = -\Delta H(AB) = H(A) + H(B) - H(AB) \qquad (II.11)$$

E_e is the electronic energy of the species at $T = 0^\circ K$ calculated at its optimal geometry without considering nuclear motion. H is the enthalpy of the species. It not only includes the electronic energy, it also has to take into account the energy of translations, vibrations, and rotations. Since the reaction normally undergoes at

constant pressure and if the ideal-gas law is followed, an RT term is also needed in order to relate enthalpy with internal energy.

$$H = E_e + E_{trans}(T) + E_{vib}(T) + E_{rot}(T) + RT \qquad (II.12)$$

At $T = 0°K$ the molecule has no translational or rotational energies, but has a nonzero ground-state vibrational energy. This energy is called zero-point energy (ZPE) and is equal to $\frac{1}{2}\sum_i \nu_i$ under the harmonic-oscillator approximation, where ν_i is the harmonic vibrational frequency of the molecule. ZPE has to be corrected from the computational energy in order for the comparison with the experimentally observed energy. To make matters even more complicated, standard enthalpies are usually tabulated for the room temperature ($T = 298°K$) at which most experiments are conducted. Therefore temperature corrections must also be made. The relation between the enthalpy at $T = 0°K$ and the enthalpy at $298°K$ is

$$\Delta H_{298°K}(AB) - \Delta H_{0°K}(AB) = \int_0^{298} [C_p(A) + C_p(B) - C_p(AB)]dT \qquad (II.13)$$

C_p is the constant-pressure heat capacity and is made up of the E_{trans}, E_{vib}, and E_{rot} contributions plus the RT term in (II.12). At $T = 298°K$ the thermal energy ($RT \sim 210\ cm^{-1}$) is too small to cause any vibrational excitation. Only the translational and rotational contributions have to be considered here. Under ideal-gas approximation the translational contribution is $\frac{3}{2}RT$. The rotational contribution is zero for atoms, $1R$ for linear molecules, and $\frac{3}{2}RT$ for non-linear molecules. The overall C_p should be $\frac{5}{2}RT$ for atoms, $\frac{7}{2}RT$ for linear molecules, and $4R$ for non-linear molecules. These guidelines have been followed when deriving bond dissociation energies and heats of formation at $T = 298°K$ from quantum calculation results.

The computation of heats of formation for HgX compounds from bond energies has adopted the following scheme.

$$HgX \longrightarrow Hg + X \qquad \Delta H^{\circ}_{298°K} = D^{\circ}_{298°K}(HgX) \qquad (II.14)$$

The heat of formation for HgX then was obtained from

$$\Delta_f H^\circ_{298^\circ K}(HgX) = \Delta_f H^\circ_{298^\circ K}(Hg) + \Delta_f H^\circ_{298^\circ K}(X) - D^\circ_{298^\circ K}(HgX) \quad (II.15)$$

$D^\circ_{298^\circ K}(HgX)$ was calculated from theoretical bond energy $D_e(HgX)$ corrected with ZPE and the temperature effects in (II.13). For $\Delta_f H^\circ_{298^\circ K}(Hg)$ and $\Delta_f H^\circ_{298^\circ K}(X)$ experimental heats of formation were used. The heat of formation for HgX_2 can be calculated in a similar way.

$$HgX_2 \longrightarrow HgX + X \qquad \Delta H^\circ_{298^\circ K} = D^\circ_{298^\circ K}(XHg - X) \qquad (II.16)$$

$$\Delta_f H^\circ_{298^\circ K}(HgX_2) = \Delta_f H^\circ_{298^\circ K}(HgX) + \Delta_f H^\circ_{298^\circ K}(X) - D^\circ_{298^\circ K}(XHg - X) \quad (II.17)$$

Again, $D^\circ_{298^\circ K}(XHg-X)$ was corrected from $D_e(XHg-X)$. The $\Delta_f H^\circ_{298^\circ K}(HgX)$ used was obtained from (II.15).

Table II.10 summarizes the calculated and experimental heats of formation for selected HgX and HgX_2 compounds. ZPE was computed using HF vibrational frequencies scaled by 0.9. The agreement with available experimental data is overall very good. In order to derive group additivity parameters for a broad spectrum of Hg-containing organic compounds whose thermochemical data are needed in metal-organic MCT growth process, we need as many as heats of formation data as possible. Table II.11 lists the heats of formation used for deriving group values of organometallic mercury compounds. *Ab initio* heats of formation were used for $MeHgF$ and $Hg(C_2H)_2$ since they are not experimentally available. The resulting group additivity parameters are listed in Table II.12. A few selected hydrocarbon parameters from S. W. Benson are also listed, where C_d refers to a carbon with a double bond to another carbon and C_t refers to a carbon with a triple bond to another carbon.

Table II.10. Calculated[a] and Experimental[b] Heats of Formation (kcal/mol) for Selected Hg Compounds

Compound	$\Delta_f H^\circ_{298^\circ K}(calc)$	$\Delta_f H^\circ_{298^\circ K}(exptl)$
$HgH_{(g)}$	55.78	57.0 ± 4.0
$HgH_{2(g)}$	33.63	–
$HgF_{(g)}$	0.77	0.7
$HgF_{2(g)}$	-71.4	-70.2
$HgCl_{(g)}$	19.23	18.75 ± 2.29
$HgCl_{2(g)}$	-36.38	-34.96 ± 1.51
$HgCH_{3(g)}$	44.57	–
$Hg(CH_3)_{2(g)}$	26.11	22.56
$HgC_2H_{3(g)}$	70.60	–
$Hg(C_2H_3)_{2(g)}$	86.60	–
$HgC_2H_{(g)}$	102.27	–
$Hg(C_2H)_{2(g)}$	116.85	–
$H_3CHgF_{(g)}$	-37.40	–
$H_3CHgCl_{(g)}$	-15.42	-12.50

[a]Energies were calculated at the QCISD(T)/20A(2f) level with MP2 geometries.
[b]Experimental data are from reference 16.

Group additivity scheme makes the implicit assumption that only neighboring and next-neighboring interactions are important in determining heats of formation. This has been shown to be valid for simple hydrocarbons and their functionalized derivatives to be within ± 1 kcal/mol of experimental values. To test the accuracy of the Hg group parameters in Table II.12, and in general the workability of group additive scheme on organomercury compounds, $\Delta_f H^\circ_{298^\circ K}$ for various Hg compounds were calculated using group parameters to compare with experimental values (Table II.13). All the calculated $\Delta_f H^\circ_{298^\circ K}$ are within 1.5 kcal/mol of exper-

Table II.11. Heats of Formation (kcal/mol) Used for Deriving Group Values of Hg Compounds

Compound	$\Delta_f H^\circ_{298^\circ K}$	Compound	$\Delta_f H^\circ_{298^\circ K}$
$HgMe_{2(g)}$	22.56[b]	$MeHgF_{(g)}$	-37.40[a]
$HgEt_{2(g)}$	17.3[b]	$MeHgCl_{(g)}$	-12.50[b]
$Hg(i\text{-}Pr)_{2(g)}$	9.63[c]	$MeHgBr_{(g)}$	-4.37[b]
$Hg(C_2H_3)_{2(g)}$	80.60[a]	$MeHgI_{(g)}$	5.35[b]
$Hg(C_2H)_{2(g)}$	116.85[a]		

[a]Energies were calculated at the QCISD(T)/20A(2f) level with MP2 geometries.
[b]Data from Ref. 16(a).
[c]Data from Ref. 17(c).

imental data, which is about on the same order of experimental uncertainties. To demonstrate how the additive scheme works, let us consider a novel Hg compound ethynal-allyl mercury, $HC{\equiv}C{-}Hg{-}CH_2{-}CH_2{=}CH_2$. To calculate the $\Delta_f H^\circ_{298^\circ K}$ of this compound, we just have to add up all the C and Hg group values. Starting from the leftmost C group, $\Delta_f H^\circ_{298^\circ K}$ = C_t-(H) + C_t-(Hg) + Hg-$(C_t)(C)$ + C-$(Hg)(C)(H)_2$ + C_d-$(C)(H)$ + C_d-$(H)_2$ = 27.10 + 10.18 + 42.80 + (-2.60) + 8.59 + 6.26 = 92.33 kcal/mol. The parameters in Table II.12 can provide a quick and easy way to estimate heats of formation for a fairly large number of organomercury compounds for which these data may not be readily available experimentally.

II.6 Summary

In this chapter, we have investigated the energetics of Hg divalent compounds using various quantum chemical methods. We have found out that in order to obtain reasonable energy results from calculations, the outer-core electrons ($5s$ and $5p$) of Hg have to be included in the active valence space (20 electrons totally). At the

Table II.12. Group Values (kcal/mol) for $\Delta_f H^{\circ}_{298^{\circ}K}$ Organometallic Mercury Compounds

Group	Value	Group	Value[a]
Hg-$(C)_2$	42.80	C-$(C)(H)_3$	-10.12
Hg-$(C_d)_2$[a]	42.80	C-$(C)_2(H)_2$	-4.95
Hg-$(C_t)(C)$[a]	42.80	C-$(C)_3(H)$	-1.90
Hg-$(C_t)_2$[a]	42.80	C-$(C)_4$	0.50
Hg-$(C)(F)$	-27.28	C_d-$(H)_2$	6.26
Hg-$(C)(Cl)$	-2.38	C_d-$(C)(H)$	8.59
Hg-$(C)(Br)$	5.75	C_d-$(C)_2$	10.34
Hg-$(C)(I)$	15.47	C_t-(H)	27.10
C-$(Hg)(H)_3$[b]	-10.12	C_t-(C)	27.55
C-$(Hg)(C)(H)_2$	-2.60		
C-$(Hg)(C)_2(H)$	3.69		
C-$(Hg)(C_d)(H)_2$[c]	-0.90		
C_d-$(Hg)(H)$	12.64		
C_t-(Hg)	9.93		

[a] Hg-(C_t)(C) = Hg-$(C_t)_2$ = Hg-$(C_d)_2$ = Hg-$(C)_2$, assigned.

[b] C-(Hg)$(H)_3$ = C-$(C)(H)_3$, assigned.

[c] C-(Hg)$(C_d)(H)_2$ = C-(Hg)$(C)(H)_2$, assigned.

[d] Group values taken from S. W. Benson, "Thermonuclear Kinetics," J. Wiley, 1968.

QCISD(T) theory level coupled with TZDP basis, bond energies within chemical accuracy can be calculated. In addition, satisfactory energy results were found to be achievable through the B3LYP/DFT method. B3LYP/DFT is a relatively inexpensive computational method and can be applied to do calculations for larger systems. In the current case, we have done B3LYP studies on the growth energetics of $Hg_{1-x}Cd_xTe$ using large cluster models. This will be discussed in the next chapter.

Table II.13. Comparison of Group Additivity Calculated $\Delta_f H^\circ_{298^\circ K}$ (kcal/mol) With Experiment

Compound	$\Delta_f H^\circ_{298^\circ K}(calc)$	$\Delta_f H^\circ_{298^\circ K}(exptl)$
$EtHgCl$	-14.86	-15.80[a]
$EtHgBr$	2.75	3.08[a]
$EtHgI$	-7.83	-7.7[a]
$Hg(n\text{-}Pr)_2$	7.46	8.2 ± 1.4[b]
$Hg(n\text{-}Bu)_2$	-2.44	-1.00[c]

[a] Data from Ref. 16(a).
[b] Data from Ref. 17(c).
[c] Data from Ref. 17(d).

We have also analyzed the bond energies of Group IIB divalent compounds through the concept of pairing energy model. We found that the pairing energy for a given Group IIB metal is not a constant as previously thought. It actually depends on the ligand the metal is bonded to. The more electronegative the ligand is, the smaller the pairing energy becomes. We have explained this finding in terms of the change in coulomb and exchange energies of the metal as a result of bonding.

Finally, using high-level *ab initio* methods, we have calculated the heats of formation for various Hg compounds, and have developed group additivity parameters for Hg. These parameters can provide a fast and accurate way to estimate heats of formation for organomercury compounds.

Chapter II References

1. M. Kaupp and H. G. von Schnering *Inog. Chem.* **33**, 2555 (1994).
2. L. J. Norrby *J. Chem. Educ.* **68**, 110 (1991).
3. C. Famiglietti, E. Baerends *J. Chem. Phys.* **62**, 407 (1981).
4. C. Møller and M. S. Plesset, *Phys. Rev.* **46**, 618 (1934).
5. J. A. Pople, M. Head-Gordon, K. Raghavachari, *J. Chem. Phys.* **87**, 5968 (1987).
6. J. Paldus, J. Cizek, and B. Jeziorski, *J. Chem. Phys.* **90**, 4356 (1989).
7. K. Raghavachari, G. W. Trucks, J. A. Pople, and M. Head-Gordon, *Chem. Phys. Lett.* **157**, 479 (1989).
8. W. Kohn and L. J. Sham. *Phys. Rev.* **A 140** 1133 (1965).
9. P. J. Hay, W. R. Wadt, L. R. Kahn, F. W. Bobrowicz, *J. Chem. Phys.* **69**, 984 (1978).
10. M. J. Frisch, G. W. Trucks, M. Head-Gordon, P. M. W. Gill, M. W. Wong, J. B. Foresman, B. G. Johnson, H. B. Schlegel, M. A. Robb, E. S. Replogle, R. Gomperts, J. L. Andres, K. Raghavachari, J. S. Binkley, C. Gonzalez, R. L. Martin, D. I. Fox, D. J. DeFrees, J. Baker, J. P. Stewart, and J. A. Pople, *Gaussian 92, Revision A*. Gaussian, Inc., Pittsburgh, PA, 1992.
11. V. Barone, A. Bencini, F. Totti, and M. G. Uytterhoeven, *J. Phys. Chem.* **99**, 12743 (1995).
12. (a) For HgH , A. Berner, P. Millie, and M. Pelissier, *Chem. Phys.* **106**, 195 (1986); (b) for $HgCl$, J. Tellinghuisen, P. C. Tellinghuisen, S. A. Davies, P. Berwanger, and K. S. Viswanathan, *Appl. Phys. Lett.* **41**, 789 (1982).
13. (a) For HgF_2, D. R. Stull and H. Prophet, *Natl. stand. Ref. Data Ser.* (U. S., Natl., Bur. Stand., NSRDS-NBS, **37**, 1971; (b) for HgC_2, P. W. Allen and L. E. Sutton, *Acta Crystallogr.* **46**, 3 (1950).
14. K. P. Huber and G. Herzberg, *Molecular Spectra and Molecular Structure*,

IV. Constants of Diatomic Molecules, 1979.

15. (a) J. C. Marson and P. P. Wolynec, *Inorg. Chem.* **30**, 1681 (1991); (b) A. Neuhaus, G. Frenking, C. Huber, J. Gauss, *Inorg. Chem.* **31**, 5355 (1992); (c) V. Jonas, G. Frenking, J. Gauss, *Chem. Phys. Lett.* **194**, 109 (1992).

16. (a) For HgF , D. D. Wagman, W. H. Evans, V. B. Porker, R. H. Shumm, I. Halow, S. M. Bailey, K. L. Churney, and R. L. Nuttall, *J. Phys. and Chem. Ref. Data* **11**, 1982, with zero-point energy correction from H. G. Howell, *Proc. Roy. Soc. A* **182**, 95 (1943); (b) for HgF_2, M. W. Chase, Jr., C. A. Davies, J. R. Downey, Jr., D. J. Frurip, R. A. McDonald, and A. N. Syverud, *J. Phys. and Chem. Ref. Data* **14**, 1985, with zero-point correction from A. Givan and A. Loewenschuss, *J. Chem. Phys.* **72**, 3809 (1980).

17. (a) For $HgCl$, K. P. Huber and G. Herzberg, *Molecular Spectra and Molecular Structure*, IV. Constants of Diatomic Molecules, 1979; (b) for $HgCl_2$, K. B. Krasnov, V. S. Timoshin, T. G. Dailova, S. Khandozhko. *Handbook of Molecular Constants of Inorganic Compounds*, Jerusalem, 1970; (c) F. R. Hartley and S. Patai, *The Chemistry of the Metal-Carbon Bond*, I. The Structure, Preparation, Thermochemistry and Characterization of Organicmetallic Compounds, 1982; (d)S. W. Benson, J. T. Francis, and T. T. Tsotsis, *J. Phys. Chem.* **92**, 4515 (1988).

18. S. B. Boys and F. Bernardi, *Mol. Phys.* **19**, 553 (1970).

19. J. H. van Lenthe, T. van Dam, F. B. van Duijneveldt, L. M. Kroon-Batenburg, *J. Faraday Symp., Chem. Soc.* **19**, 125 (1984).

20. R. Krishnan, J. S. Brinkley, R. Seeger, J. A. Pople, *J. Chem. Phys.* **72**, 650 (1980).

21. A. K. Rappé and W. A. Goddard III, unpublished.

22. (a) L. Wharton, R. A. Berg, and W. K. Klemperer, *J. Chem. Phys.* **39**, 2023 (1963); (b) A. Buchler, J. L. Stauffer, and W. Klemperer, *J. Am. Chem. Soc.*

86, 4544 (1964).

23. M. Kaupp, P. v. R. Schleyer, H. Stoll, and H. Preuss, *J. Am. Chem. Soc.* **113**, 6012 (1991).
24. P. J. Young, R. K. Gosavi, J. Connor, O. P. Strausz, and H. E. Gunning, *J. Chem. Phys.* **58**, 5280 (1973).
25. A. S. Carson and J. A. Spencer, *J. Chem. Thermodynamics* **16**, 423 (1984).
26. S. W. Benson and J. H. Buss, *J. Chem. Phys.* **29**, 546 (1958).

Chapter III

Epitaxial Growth Study of $Hg_{1-x}Cd_xTe$ Using Clusters

Abstract

A novel metal-organic molecular beam epitaxial (MOMBE) growth strategy for growing $Hg_{1-x}Cd_xTe$ on the (001) surface orientation using $H_2C{=}CH{-}CH_2{-}Hg{-}C{\equiv}C{-}CH_3$ and TeH_2 as molecular precursors was examined by quantum molecular orbital calculations. The study showed that with the new growth strategy, Hg vacancy and p-doping problems in growing MCT may be avoided. The overall growth is energetically favorable by $\sim$ 2.45 eV indicated by cluster calculations. A very similar energy result can be obtained from simple $Hg{-}Te$ molecular complex calculations without using large cluster models.

III.1 Introduction

Epitaxial Growth on semiconductor surfaces is believed to take place under non-equilibrium conditions and is intrinsically controlled mainly by kinetics.[1,2] However, if the surface relaxation rate is much larger than the arrival rate of incoming atoms, the surface growth process can be described thermodynamically because surface atoms will have enough time to minimize their free energy before the arrival of next atom. It has indeed been shown that, by using separate pulses of reactants and properly chosen growth conditions in atomic layer epitaxy (ALE) growth, thermodynamics governed surface stoichiometry can be achieved.[3,4] The ALE process consists of a sequence of exchange reactions between reactant atoms or molecules in the gas-phase and a solid substrate. These conditions during the deposition allow the growth of the film to be controlled on the molecular level, which therefore can be examined through quantum chemical methods.

In this study, we have examined the basic process of both atomic and molecular epitaxial growth procedures of $Hg_{1-x}Cd_xTe$ (MCT) in order to gain a quantitative description of the chemical reactions occurred between the gas-phase species and the solid substrate by using a quantum chemical cluster approach. In this approach the cluster-adsorbate system is regarded essentially as a large molecule and is investigated by electronic structural studies. Preferential surface adsorption geometries and energies were obtained. From these results, a novel MOMBE growth strategy was designed for overcoming the Hg vacancy and p-doping problems often encountered in MCT thin film growth. In the following sections we will discuss epitaxial growth of MCT based on results from cluster calculations. The details of cluster calculations are described in Appendix B.

III.2 Atomic Growth of MCT on the (001) Surface Orientation

Since Te has six valence electrons and Hg only has two, the bonding in bulk $HgTe$ can be rationalized as Te making two covalent bonds and two donor-acceptor

(DA) bonds (using the two lone pair orbitals on Te) to the Hg while Hg atoms making two covalent bonds and two DA bonds (using the two empty orbitals on Hg) to the Te. Thus, each $Hg-Te$ bond in the bulk can be regarded as of half-covalent and half-DA nature.

As discussed in Appendix B, in the (001) surface the electronically stable structures always have two covalent bonds so that the broken bonds are all of DA type (i.e., empty dangling orbitals on Hg and doubly occupied dangling orbitals on Te). For the Hg rich (001) surface of $HgTe$ this leads to a structure in which each surface Hg forms a full covalent bond to each of two sub-surface Te. Since the sub-surface Te also forms two bulk-like bonds to two third layer Hg (each of which is 1/2 covalent and 1/2 DA), the Te can bond to only one surface atom. As a result, half the surface Hg sites are empty, leading to either a $p(2\times 1)$ or $c(2\times 2)$ structure. See Appendix B for more discussion on surface structures and reconstructions.

The surface Hg has a bond angle of 161.4° to the two sub-surface Te, reflecting the preference for 180° angles of covalent bonds to Hg. Removing the surface Hg costs about

$$E_{desorp}(Hg) = 0.99 \text{ eV} \qquad (III.1)$$

even though the calculated covalent $Hg-Te$ bond from $HHg-TeH$ is 2.59 eV (see Appendix C). This is because the free Hg atom has a very stable $6s^2$ configuration. Large stabilization energy is gained from returning to that state. For comparison, the Cd desorption energy was calculated to be 1.61 eV which is much larger than 0.99 eV of Hg. This is owing to the combining effects of the smaller $5s^2$ stabilization energy and the larger $Cd-Te$ bond energy.

We believe that the small bond energy of Hg to the surface in (III.1) is the origin for problems in $Hg_{1-x}Cd_xTe$ growth. We can estimate the desorption temperatures of surface Hg and Cd from the simple rate model for atomic desorption

given by Goddard and co-workers[5]

$$R = \frac{\Omega_o}{2\pi} exp(\frac{-E_d}{k_B T}), \qquad (III.2)$$

where R is the desorption rate constant, Ω_o is the vibrational frequency of the atom against the surface, and E_d is the activation energy for desorption. Taking the T derivative of total desorption rate function one can arrive at the relation between the activation energy E_d and temperature, T_{max}, for which the maximum of the desorption spectrum is obtained. If we use the typical value of 1.5×10^{14} for the preexponetial factor and the desorption energy for E_d to calculate the T_{max} for Hg and Cd desorption, we get the lower bound of desorption temperature

$$T_{max}(Hg) = 123\ ^\circ C$$
$$T_{max}(Cd) = 367\ ^\circ C \qquad (III.3)$$

The small surface bond energy and low desorption temperature may explain why at typical MBE film growth temperatures ($170 \sim 190\ ^\circ C$) the surface Hg tends to evaporate while incoming Hg from the source does not lead to favorable incorporation to the surface. No such problems exist for Cd. Thus, even with a Hg flux 1000 times that of Cd, Hg vacancies still are abundant in the $Hg_{1-x}Cd_xTe$ film. These vacancies lead to deterioration in electronic properties of the film.

Similar problems exist when one tries to grow p-type materials, e.g., by doping with As into Te positions in the lattice. The presence of Hg vacancies can lead to compensation in which some As atoms get incorporated into the Hg site rather than the intended Te site. Unfortunately these problems are intrinsic to MBE since it uses elemental source. The above considerations led us to consider using novel organometallic Hg precursor source for growth, as discussed in the next section.

II.3 Organometallic Growth Strategy of MCT

Since we have identified that the cause of problems with growing $Hg_{1-x}Cd_xTe$ is the weak bond of the surface Hg to the sub-surface Te, our concept here is to replace atomic Hg and Te precursors in the growth strategy with organometallic molecules, say $RHgR$ and $HTeH$, such that each Hg on the surface still has one R and such that each Te on the surface has one H. From the cluster calculations in Appendix B, the energy cost to remove HgH form the surface is

$$E_{desorp}(HgH) = 2.56 \text{ eV}, \qquad (III.4)$$

which is much higher than for (III.1). This energy corresponds to a $T_{max} = 740\ ^{\circ}C$, which is much higher than normal growth temperatures. The main difference between Hg and HgR is that unlike Hg, the promotion energy $E_p(6s)$ is not needed for HgR to bond to the surface. This favors HgR energetically to react with the surface and results in a higher sticking coefficient for HgR. Therefore we believe that replacing Hg with HgR in epitaxial $Hg_{1-x}Cd_xTe$ growth will increase the extent of Hg incorporation and avoid the Hg vacancies and p-doping problems. To demonstrate how we can include HgR into the growth strategy, let us consider the following idealized ALE growth sequence (as illustrated in Figure III.1 and III.2):

(i) Hg growth cycle

Let us start off with a (001) surface saturated with $Te{-}H$ bonds. (This surface can be obtained by, for example, impinging active H flux on the $\Theta = 1$ Te dimer surface.) Each surface Te will have one $Te{-}H$ bond and one lone pair. The incoming gas-phase $RHgR$ would react with one surface $Te{-}H$ to form a $TeHgR$ unit on the surface and a RH leaving the surface. This at first leads to a surface $Te{-}Hg$ bond with bond order of one, but additional surface $Te{-}Hg{-}R$ species would cause bridging between adjacent Te sites to form HgR bridge structures in which the two $Hg{-}Te$ bonds are of bond order $\frac{1}{2}$. When all the surface sites are occupied, we end up with a surface terminated with $Hg{-}R$ bonds.

Hg cycle

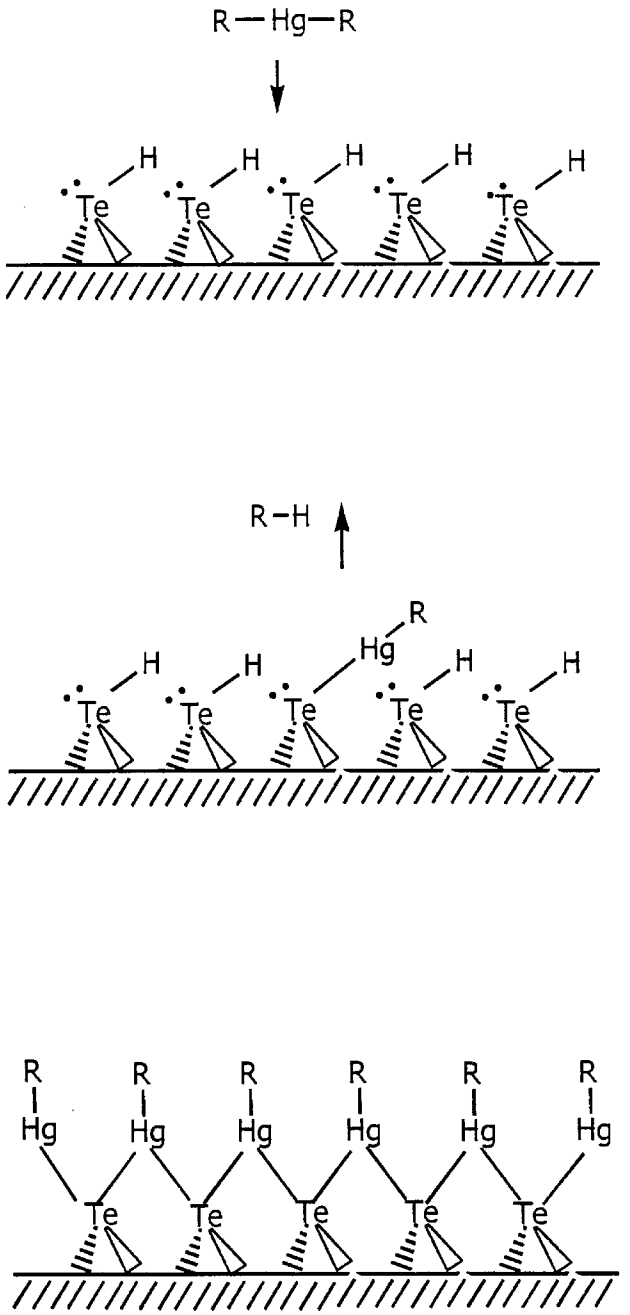

Figure III.1. Hg growth sequence for the MOMBE growth of MCT.

(*ii*) Te growth cycle

Next the incoming gas-phase $HTeH$ reacts with the surface HgR units to form surface TeH units and gas-phase RH units. An isolated unit leads to bond order of one for the surface $Te-Hg$ bond but additional surface $Hg-TeH$ species leads to bridging between Hg sites to form TeH bridge structures. After all the surface sites are saturated with $Te-H$, the resulting surface is exactly the same as the starting surface in (*i*). The only difference is that totally one monolayer of $HgTe$ has been added to the surface. This way the material can be grown in a layer-by-layer fashion, which is ideal for obtaining high-quality films.

Now we come to a point to decide what type of $RHgR$ compound will make the best candidate for our growth strategy. As discussed in Chapter II, due to the relativistic effects which increases the $6s-6p$ energy separation of Hg, the significantly large $E_p(6s)$ makes Hg species difficult to maintain in the $Hg-R$ (^{3}P) state. $Hg-R$ will tend to break the bond and become Hg (^{1}S) + R state, having the stabilization energy P_{6s} as the driving force. Indeed when R = methyl or ethyl, we have calculated the bond energy (in Chapter II)

$$D(Hg-CH_3) = 0.25 \text{ eV}, \qquad (III.5)$$

$$D(Hg-CH_2CH_3) = 0 \text{ eV} \qquad (III.6)$$

As we can see, $Hg-$alkyl compounds are not really stable. We are concerned that the short-lived HgR species will not work in our growth strategy which requires an active role of HgR. The bond energy of $Hg-F$ was calculated to be 1.42 eV, which should be a stable enough species to fit in the growth strategy. However, halogens are electronically active species and can act as n-type dopant in the II-VI semiconductor and therefore must be excluded to avoid unwanted incorporation into the thin film during growth. In addition, an organic ligand is preferred for vapor

Te cycle

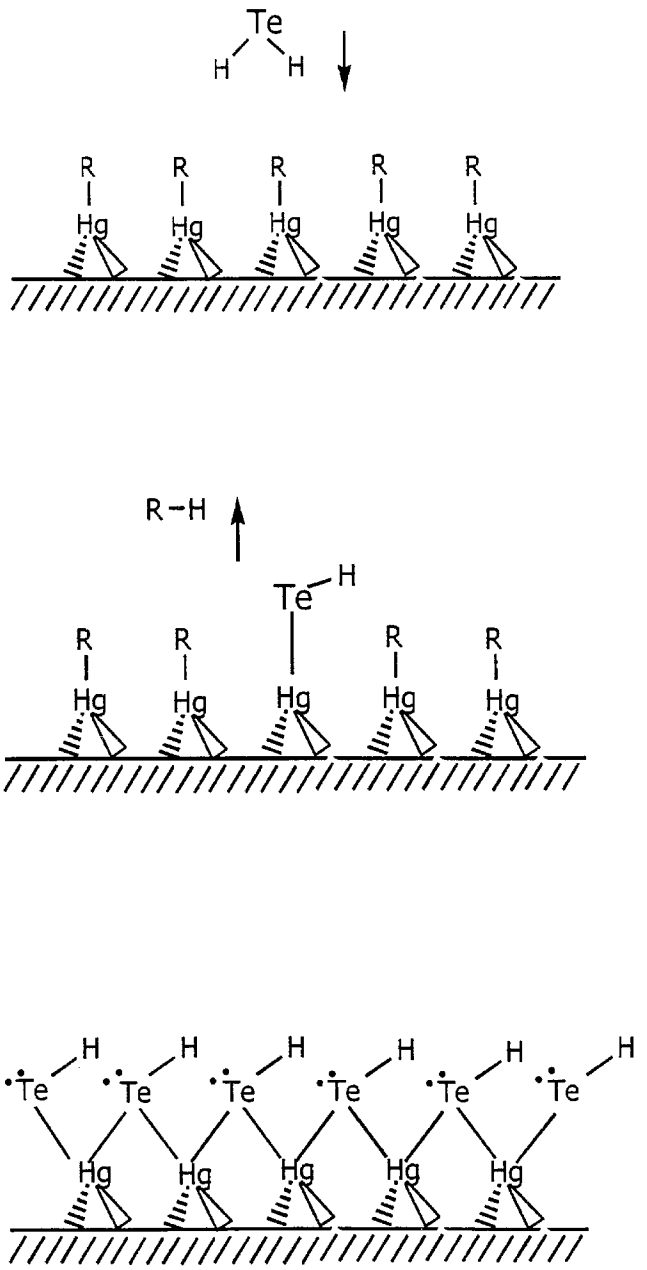

Figure III.2. Te growth sequence for the MOMBE growth of MCT.

pressure consideration. In the process of finding a suitable R, we have discovered that when R = ethynal, the $Hg-C$ bond energy

$$D(Hg - C \equiv CH) = 1.73 \text{ eV}, \qquad (III.7)$$

which is surprisingly strong for an organic ligand. In fact, the $Hg-C\equiv CH$ bond energy is even larger than that of $Hg-F$. This is probably because of the more electronegative nature of C_{sp} and the better overlap between C_{sp} and Hg_{sp} orbitals. We are convinced that with such a strong bond, the $-C\equiv CH$ ligand can remain bonding to Hg, forcing it to stay in the ^3P state until the next step of surface reaction occurs.

Organometallic Hg precursors (usually Hg alkyls) often need to be pre-cracked before entering the growth chamber because of their high pyrolysis temperatures. Unlike the first $Hg-R$ bond, the second $RHg-R$ bond is normally quite strong, making it difficult to activate $RHgR$ since the $RHg-R$ bond breaking on the surface is the first step toward growth reactions. It is well known that among simple organic ligands, the allyl group ($-CH_2=CH-CH2$) has a stable radical form and makes weaker bonds than most alkyls. Therefore instead of alkyls, if we bond to Hg with an allyl group as the second R, due to the delocalization of the free radical over the three carbon atoms,

$$CH_2 = CH - CH2 \longrightarrow CH_2 - CH = CH_2 \qquad (III.8)$$

the stabilization effect will make $Hg-$allyl bond easier to break and thus eliminating the pre-cracking process. Indeed, the calculated bond energy when R = allyl

$$D(RHg - allyl) = 1.95 \text{ eV} \qquad (III.9)$$

is much weaker than

$$D(RHg - methyl) = 2.60 \text{ eV} \qquad (III.10)$$

From examining the energetics of $RHgR$, we have demonstrated that it is possible to solve the $Hg_{1-x}Cd_xTe$ growth problems by adopting a novel Hg precursor $H_2C{=}CH{-}CH_2{-}Hg{-}C{\equiv}CH$ for growth. To verify the thermodynamic feasibility of the growth process using such a Hg precursor, coupled with TeH_2 as the Te precursor we have studied the overall growth energetics using cluster calculations. The growth reactions modeled by clusters are illustrated in Figure III.3. The Hg growth cycle was calculated to be exothermic by 1.36 eV and the Te growth cycle was calculated to be exothermic by 1.09 eV. The overall growth thus is exothermic by 2.45 eV, which is energetically quite favorable.

In Appendix B it has been shown that atoms in the surface layer behave very much "molecular-like." Their bond characteristics are very similar to those in free molecular bonding. Therefore instead of carrying out cluster calculations which are computational intensive and extremely time-consuming, we may be able to approximate the growth reactions using simple II-VI molecular complexes and calculate the energetics with much less computational efforts. If we approximate the $-TeH$ terminated surface with $H{-}TeH$ and the $-HgC{\equiv}CH$ terminated surface with $HTe{-}HgC{\equiv}CH$, the growth energetics are calculated to be

$$HTeH + H_2C = CHCH_2HgC \equiv CH \longrightarrow HTeHgC \equiv CH + H_3CCH = CH_2$$

$$\Delta E = -1.39 \text{ eV} \quad (Hg \text{ growth cycle}) \qquad (III.11)$$

$$HTeHgC \equiv CH + HTeH \longrightarrow HTeHgTeH + HC \equiv CH$$

$$\Delta E = -1.04 \text{ eV} \quad (Te \text{ growth cycle}) \qquad (III.12)$$

These energy agree very well with those from cluster calculations. The implication of this result is that, with a simple molecular approximation, we are able to calculate the growth energetics of any combination of Hg and Te precursors without resorting

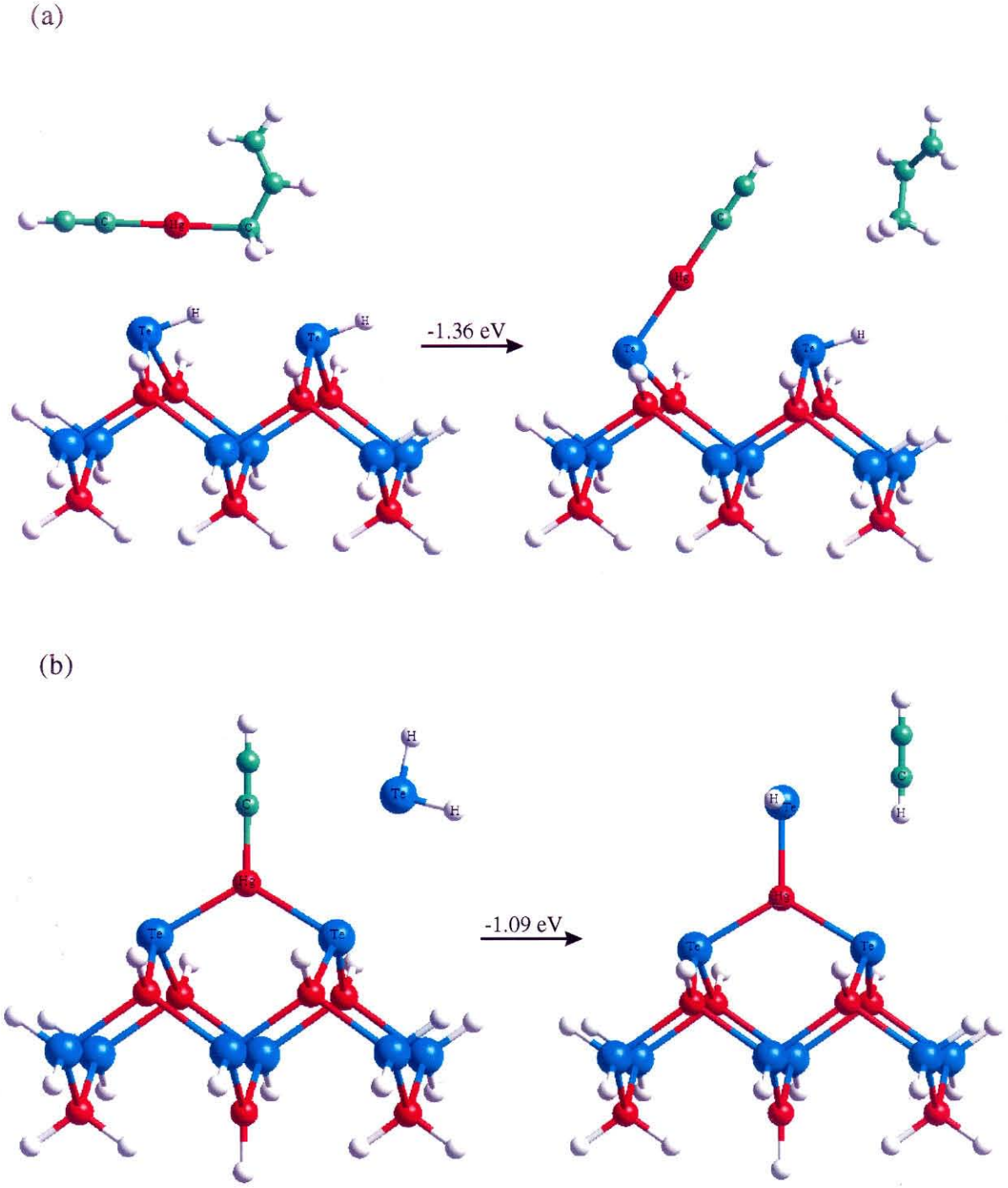

Figure III.3. Reaction energetics for (a) Hg growth cycle (b) Te growth cycle using cluster calculations (B3LYP/TZDP).

to cluster calculations. (III.11) and (III.12) therefore can serve as a screening test for potential precursors. For any organomercury asymmetric divalent compounds, there might be a concern of disproportionation reaction that can lead to the formation of undesired symmetric Hg species. One way to avoid this reaction is to have equal numbers of carbons on both ligands. Therefore in case where disproportionation indeed occurs. we can use $H_2C{=}CH{-}CH_2{-}Hg{-}C{\equiv}C{-}CH_3$ as the Hg precursor instead. This should not affect the energetics calculated earlier since the bond-breaking scheme remains the same. The overall growth of $HgTe$ layer of MCT using this MOMBE strategy is illustrated in Figure III.4. One should also be able to grow the $CdTe$ layer following the same strategy.

III.4 Conclusion

Using a novel Hg precursor compound having one strong $Hg{-}C$ bond ($Hg{-}C{\equiv}C{-}CH_3$) to increase the Hg sticking coefficient to the surface and one weak $Hg{-}C$ bond ($Hg{-}CH_2{-}CH{=}CH_2$) to reduce surface pyrolysis temperature, a MOMBE layer-by-layer growth strategy on the (001) surface orientation is demonstrated to have the potential to solve the Hg vacancy and p-doping problems troubling current MCT growth. This is the first time that an atomistic epitaxial growth mechanism has ever been proposed. We believe this strategy should also be applicable to all epitaxial techniques (such as MOCVD and MOVPE) that utilize organometallic molecules as precursors to grow MCT.

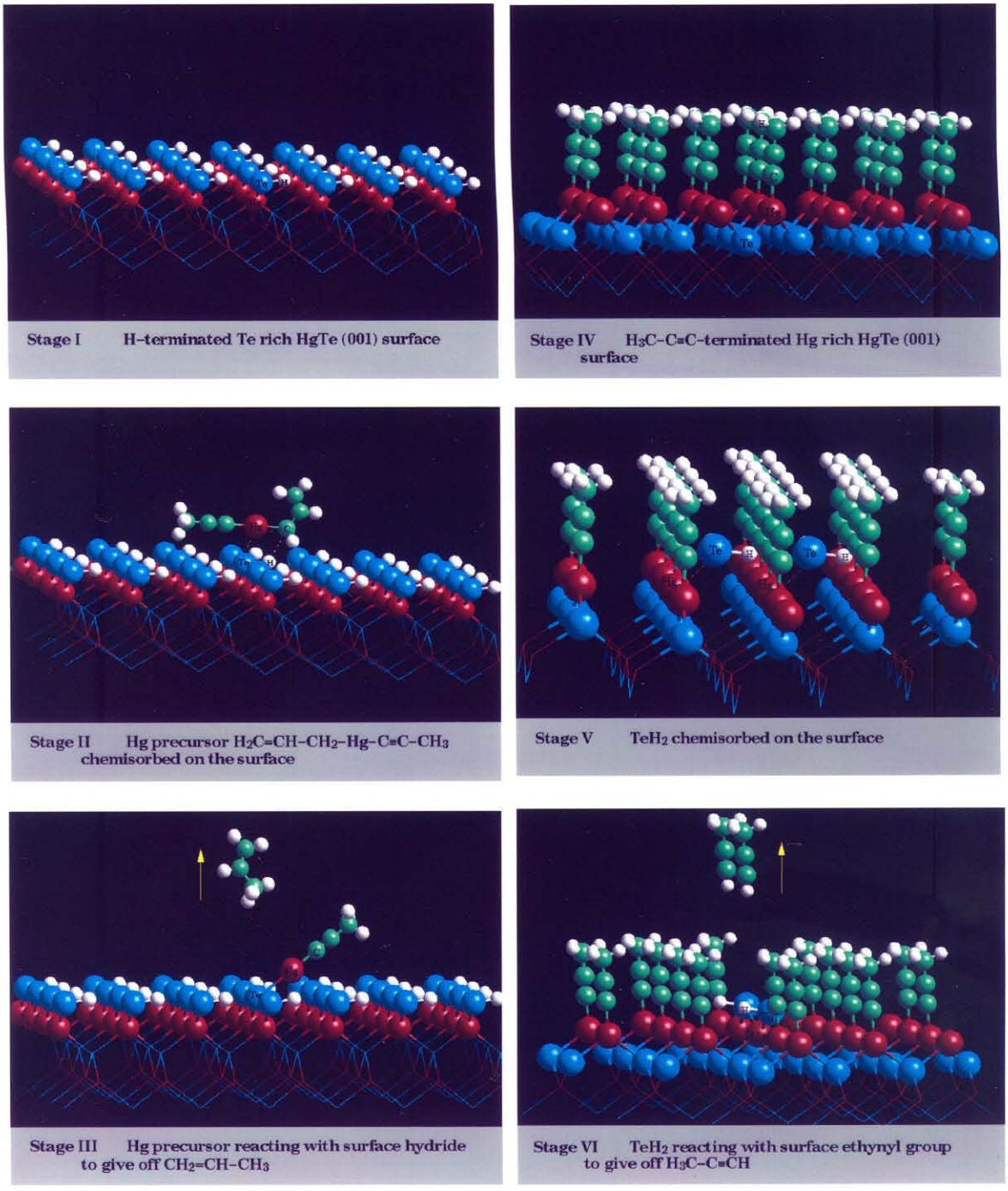

Figure III.4. The six stages of MOMBE growth strategy for HgTe.

Chapter III References

1. R. L. Harper. J. W. Han, S. Hwang, Y. Lansari. N. C. Giles. J. W. Cook, and J. F. Schetzina, *J. Vac. Sci. Technol.* **B7**. 244 (1989).
2. S. Sivanandan. X. Chu, J. Reno. and J. P. Faurie. *J. Appl. Phys.* **60**, 1359 (1986).
3. T. Yao, Z. Q. Zhu, K. Useugi, S. Kamiyama, and M. Fujimoto, *J. Vac. Sci. Technol.* **A8**, 997 (1990).
4. L. Lilja, J. Keskinen. M. Hovinen. and M. Pessa. *J. Vac. Sci. Technol.* **B7**, 593 (1989).
5. Y. Zeiri. A. Redondo, Y. Zeiri, and W. A. Goddard III. *Surf. Sci.* **131**, 221 (1983).

Appendix A: Computational Details

A.1 *Ab Initio* Methods

Single-reference Hartree-Fock and post Hartree-Fock *ab initio* methods used in this research work are summarized here.

A.1.1 Hartree-Fock (HF)

The Hartree-Fock self-consistent-field (SCF) method takes into account the interactions between electrons only in an average way. Even though the HF method is capable of providing good geometrical parameters for most stable molecules, the energy computed by the HF method usually errors by about 1% of the total energy, which often translates to several eV in error when calculating the bond energy of a chemical bond. Nevertheless, the HF wave function can still offer a reasonable overall description of the chemical system for use by other post HF configuration interaction (CI) methods, from which more accurate energy results can be obtained. The computer CPU time required for HF and post HF-based methodology, including electron correlation treatment, increases at between n^4 and n^7. n is the number of basis functions and is typically $2 \sim 5$ times the number of electrons.

A.1.2 Møller-Plesset Second-order (MP2)

Unlike HF's inability to describe electron correlation, the MP2 method is based on many-body perturbation theory, treating the correlation part of the Hamiltonian as a perturbation on the HF part and truncate the energy expansion at the second-order. Normally $75\% \sim 84\%$ of the correlation energy can be accounted for by using MP2 with complete basis of s, p, and d functions.[1] MP2 approximation is popular among theorists because of its favorable accuracy to computational cost ratio. The method is size-consistent, so that when applied to an ensemble of isolated molecules, calculated energies are additive. This is an important requirement

when one is interested in the relative energies of molecules of different sizes. MP2 however is not variational; it does not give an upper bound to the exact energy.

A.1.3 Quadratic Configuration Interaction Singles and Doubles With Triples Perturbation (QCISD(T))

The instantaneous electron correlation can be accounted for through configuration interaction (CI). Electron correlation treatments based on a single configuration state are much faster than multi-configuration approaches, and can therefore be used with extended one-particle basis sets. The mixing of excited configurations from the single-configuration HF wavefunction contributes the correlation energy for the system. The number of possible configurations increases very rapidly as the number of electrons m and the number of basis functions n increase ($\sim n^m$ configurations). Even with limited finite basis, a full CI calculation including all possible configurations is only possible for very small systems.[2] In practice, truncated CI with singly and doubly excited configurations (CISD) is often used and has been found to provide reasonable electron correlation of the ground state. Truncated CI provides only upper bounds to the exact energies and is thus variational. It however, does not offer size consistency. The QCISD(T) approximation introduces new terms which are quadratic in the configuration coefficient and can restore size consistency in the resulting total energy. A simplified triple-substitution correction is also added and is well-recognized to improve accuracy for many systems.[3] QCISD(T) is among the handful *ab initio* methods that have been used extensively to obtain quantitative and accurate chemical energetics information. However the method scales as n^7 which makes it rather expensive.

A.1.4 Coupled Cluster Singles Plus Doubles With Triples Perturbation (CCSD(T))

CCSD(T) is a size-consistent and variational method based on coupled clus-

ter (CC) theory.[4] This approach allows for interactions between pairs. It uses perturbation theory and calculates a correlated wave function directly from integrals over basis functions without constructing the Hamiltonian matrix. In most cases CCSD(T) offers compatible accuracy of QCISD(T), but costs about 20% more of computer time. Nevertheless, in cases where triple excitations are important QCISD(T) may show an exaggeration of T effects,[5] causing serious errors. In this work, the CCSD(T) method was used as a reference to the QCISD(T) calculation to make sure the result is reasonable.

A.2 Density Functional Theory (DFT)

During the past decade much interest has been given to methods based on density functional theory (DFT). DFT appears to be a versatile computational approach capable of successfully describing many problems previously could only be covered exclusively by *ab initio* HF and post-HF methods. Based on the Hohenberg-Kohn theorem,[6] the basic notion in DFT of many electron systems is that the exact energy of an electronic system can be expressed in terms of its electron density. There is a one-to-one correspondence between the external field $V_{ext}(r)$ and the single-particle density $\rho(r)$. As a consequence it is possible to write the total ground-state energy as a functional of $\rho(r)$,

$$E[\rho] = E_0[\rho] + \int dr V_{ext}(r)\rho(r). \qquad (A.1)$$

Here $E_0[\rho]$ is a functional that is independent of the external potential $V_{ext}(\rho)$. For any trial density $\overline{\rho}(r)$ that satisfies $\int \rho(r) =$ the total number of electrons,

$$E[\overline{\rho}] \geq E_g, \qquad (A.2)$$

where E_g is the true ground-state energy. The equality in (A.2) holds only when $\overline{\rho}(r)$ is the true ground-state density. The theorem provides a general method for calculating ground-state properties. If an approximation functional can be found

for $E_0[\rho]$, the E_g can be solved variationally for the $V_{ext}(r)$ of interest. Normally $E_0[\rho]$ is a combination of exchange and correlation functionals. There are a variety of implementations of DFT available, depending on what functionals are used.

The major advantage of DFT over wavefunction-based *ab initio* methods is that DFT is computationally much less demanding. The CPU time increases at n^4 as opposed to between n^5 and n^7 for post HF methods of similar accuracy. For large systems where high-level CI methods are impractical to use, the DFT approximation appears to be the only available quantum chemical method that can yield reliable enough results to be of chemical relevance. The B3LYP variant uses Becke gradient correction to exchange functional,[7] the Lee-Yang-Parr (LYP) correlation functional,[8] and the semi-empirical coefficients determined by Becke from a best fitting of the heats of formation of a standard set of molecules with a closely related approach.[7] B3LYP has been shown to reproduce the heats of formation of a wide range of molecules to an accuracy of $\pm$ 2 kcal/mol, and is currently the most popular DFT implementation for studying chemical reactions and energetics. It often can provide the accuracy similar to for MP2 or even MP4 with much less computational cost. For the calculations of Group IIB compounds in Chapter II, B3LYP was used along with conventional *ab initio* methods to access the accuracy issue of DFT approach. It then was used exclusively in later chapters for large cluster calculations.

A.3 Basis Sets and Effective Core Potentials (ECP)

The success of a quantum chemical calculation depends not only on the level of electron correlation treatment but also on the basis set used. Since the use of infinite basis sets in the calculation is out of the question, the molecular orbitals are usually approximated as linear combinations of a finite number of basis functions. With medium-sized basis functions and configuration interaction methods, one can obtain reasonably good electronic energies. Further improvements in these energies

(particularly dissociation energies) can be brought about by employing larger basis sets augmented with polarization functions. The choice of these truncated finite basis sets however is not unique, and larger basis sets do not always give better results. A lot of times the selection of an appropriate basis set is still more art than science. In Chapter II basis set effects at various theory levels were investigated.

For Group IIB atoms effect core potentials (ECP) were used to eliminate chemically inactive atomic core electrons from quantum mechanical calculations. These ECP's not only serve to reduce the computational effort, more importantly, they also offer the incorporation of relativistic effects into the calculation for heavy elements. Both factors are especially important for Hg. Hg has a total of 80 electrons which are too computational demanding to be considered explicitly in a CI calculation. The bonding in mercury compounds is believed to be mainly due to covalent overlap interactions of the Hg $6s$ orbitals where relativistic effects dominate. It is a well established fact that relativistic effects can modify bond lengths by about 0.2 Å and significantly affect energetic quantities.[9]

From the ECP point of view the definitions of core and valence orbitals often are arbitrary. One may wish to include as few electrons in the valence space as possible to reduce computational cost. However this strategy works well only when the defined core electrons do not have significant interaction with the valence electrons to affect the calculation result. Depending on the chemical properties of interest, a larger core (smaller valence) may suffice for some calculations while others may require a smaller core (larger valence). Earlier papers on mercury compounds calculations often accounted only for the $6s^2$ valence electrons within a pseudopotential approximation for the mercury atom, assuming the $5d$ shell to be frozen.[10~12] Now it is known that keeping the mercury $5d$ electrons frozen leads to errors mainly because of the incorrect description of core-core repulsion and of neglect of core polarization (core-valence correlation).[13,14] Therefore, this 2-valence-electron core

was not considered in this work. To study the core effect, two sets of relativistic ECP's were used for Group IIB elements. One is the (Z-12)-electron core potential from Hay and Wadt,[15] treating the $(n-1)d^{10}ns^2$ electrons explicitly. The other is the (Z-20)-electron core potential from Christiansen *et al.*,[16] which includes the outer core $(n-1)s^2(n-1)p^6$ electrons in the valence space. The valence basis sets and ECP's used in the calculations were constructed as described in the following.

Basis set and ECP scheme

Each basis/ECP combination is denoted as a number followed by a letter. The number represents the number of electrons treated explicitly in the valence space. The letter represents the particular basis set used.

12A – Group 12 elements use Hay and Wadt's ECP's and double-zeta basis sets,[15] leading to a $(3s2p5d/2s2p2d)$ basis for Zn, a $(3s3p4d/2s2p2d)$ basis for Cd, and a $(3s3p3d/2s2p2d)$ basis for Hg. Dunning's valence double-zeta basis sets,[17] (4s/2s) for H and (10s5p/3s2p) for F, are used. For Cl, Hay and Wadt's (Z-7)-electron ECP and (3s3p/2s2p) basis set are used.[18] The 12A scheme is exactly the same as the standard double-zeta quality basis/ECP in Gaussian 92 program with the keyword "LANL1DZ."

12B – Group IIB elements and Cl use the same scheme as in 12A except that all of the s functions are now un-contracted. In addition, the Cl basis set is augmented with one d polarization function with exponent of 0.63. This leads to $(3s2p2d)$ for the Group IIB and $(3s2p1d)$ for Cl. Both H and F use 6-31G** basis sets.[19]

12B(1f) – This scheme is the same as 12B except that each Group IIB basis set is augmented with one f polarization function with exponent of 3.90 for Zn, 1.80 for Cd and 0.56 for Hg, leading to an overall DZSP quality basis.

20A – The (Z-20) ECP's and triple-zeta basis sets from Christiansen *et al.*[16] are

used for Group IIB elements. This corresponds to a (7s6p6d/4s4p3d) basis for Zn. a (5s5p4d/4s4p3d) for Cd, and a (5s5p4d/4s4p3d) for Hg. Dunning's (6s/3s) basis[20] plus two sets of p polarization functions (exponents of 1.407 and 0.388) is used for H. For C and F Huzinaga's (11s7p/5s3p) basis[21] plus two sets of d polarization functions (exponents of 1.097 and 0.318 for C; 3.107 and 0.855 for F) is used. For Cl, Hay and Wadt's $(Z-7)$-electron ECP and un-contracted (3s3p) basis set is used,[18] augmented with two sets of d polarization functions (exponents of 0.80 and 0.22).[22]

20A(2f) – This scheme is the same as 20A except that each Group IIB element in 20A is augmented with two sets of f polarization functions with exponents of 6.15 and 1.65 for Zn,[23] 2.80 and 0.80 for Cd,[23] 0.99 and 0.28 for Hg, leading to an overall TZDP quality basis.

20B – A more extensive basis set (8s/7p/6d/6s5p3d)[24] is used for each Group IIB atom. The remaining ECP's and basis sets are kept the same as in 20A.

20B(2f) – Additional two sets of f polarization functions (from 20A(2f)) are added to each Group IIB atom. The remaining ECP's and basis sets are kept the same as in 20B.

To verify the quality and performance of the Group IIB ECP's and basis sets, atomic energies (first excitation energy and first through second ionization energies) were calculated at the QCISD(T) level and are listed in Table A.1. Among these quantities the first excitation energy, $M(^1S) \rightarrow M(^3P)$, is especially important because Group IIB elements have the ns^2 configuration. Almost all chemical reactions for atoms with this particular ground-state configuration involve one electron excited from the ns to the np orbital. Within the theoretic framework of QCISD(T), the calculated energies compare reasonably well with the experimental energies. One exception is the 20A(2f)-calculated first excitation energy for Zn,

Table A.1. QCISD(T)-calculated and Experimental[25] Atomic Energies (eV) of the Group IIB Elements

M/Method	$M(^1S) \rightarrow M(^3P)$	1st IP	2nd IP
Zn/12B(1f)	3.77	8.57	16.82
Zn/20A(2f)	7.95	9.11	17.54
Zn/20B(2f)	3.86	8.80	16.48
Zn/exptl	4.01	9.36	17.89
Cd/12B(1f)	3.70	8.59	16.16
Cd/20A(2f)	3.57	8.54	16.26
Cd/20B(2f)	3.67	8.70	16.53
Cd/exptl	3.73	8.96	16.84
Hg/12B(1f)	5.02	9.93	17.94
Hg/20A(2f)	5.20	9.89	18.01
Hg/20B(2f)	5.04	10.19	18.43
Hg/exptl	4.67	10.38	18.67

which is almost twice as large as the experimental value. The failure to describe ^3P state properly could result in significant errors when calculating molecular properties. Therefore for all the Zn calculations, we used 20B(2f). Also, the inclusion of outer core elections in the valence space does not necessarily improve the calculated energies. This may suggest that these elections play a minor role in the excitation process.

Appendix A References

1. J. S. Binkley and J. A. Pople, *Intern. J. Quantum Chem.* **9**, 229 (1975).
2. C. A. Bauschlicher, Jr., S. R. Langhoff, P. R. Tayer, and H. Partridge, *Chem Phys. Lett.* **126**, 436 (1986).
3. J. A. Pople, M. Head-Gordon, and K. Raghavachari, *Intern. J. Wuantum Chem. Quantum Chem. Symp.* **22**, 377 (1988).
4. J. Cizek, *J. Chem. Phys.* **45**, 4256 (1966).
5. Z. He and D. Cremer, *Theoret. Chim. Acta* **85**, 305 (1993).
6. P. Hohenberg and W. Kohn, *Phys. Rev.* **B 136**, 864 (1964).
7. A. D. Becke, *J. Chem. Phys.* **98**, 5648 (1993).
8. C. Lee, W. Yang, and R. G. Parr, *Phys. Rev.* **B 37**, 785 (1988).
9. P. Schwerdtfeger, P. D. W. Boyd, S. Brienne, J. S. McFeaters, M. Dolg, M. -S. Liao, and W. H. E. Schwarz, *Inorg. Chim. Acta* **231**, 233 (1993).
10. G. Das and A. C. Wahl, *J. Chem. Phys.* **64**, 4672 (1976).
11. P. Hafner and W. H. E. Schwarz, *Chem. Phys. Lett.* **65**, 537 (1979).
12. H. Basch, M. D. Newton, J. Jafri, J. W. Moskowitz, and S. Topiol, *J. Chem. Phys.* **68**, 4005 (1978).
13. W. Muller, J. Flesch, and W. Meyer, *J. Chem. Phys.* **80**, 3297 (1984).
14. H. Stoll, P. Fuentealba, M. Dolg, J. Flad, L. Vonszentpaly, and H. Preuss, *J. Chem. Phys.* **79**, 5532 (1983).
15. P. J. Hay and W. R. Wadt, *J. Chem. Phys.* **82**, 270 (1985).
16. (a) M. M. Hurley, L. F. Pacios, P. A. Christiansen, R. B. Ross, and W. C. Ermler, *J. Chem. Phys.* **84**, 6840 (1986); (b) L. A. LaJohn, P. A. Christiansen, R. B. Ross, T. Atashroo, and W. C. Ermler, *J. Chem. Phys.* **87**, 2812 (1987); (c) R. B. Ross, J. M. Powers, T. Atashroo, W. C. Ermler, L. A. LaJohn, and P. A. Christiansen, *J. Chem. Phys.* **93**, 6654 (1990).
17. T. H. Dunning, Jr and P. J. Hay *Modern Theoretical Chemistry*, Ed. H. F.

Schaefer, III, Plenum: New York,1976, 1-28.

18. P. J. Hay and W. R. Wadt, *J. Chem. Phys.* **82**, 284 (1985).
19. R. Ditchfield, W. J. Hehre, and J. A. Pople, *J. Chem. Phys.* **54**, 724 (1971).
20. T. H. Dunning, *J. Chem. Phys.* **55**, 716 (1971).
21. S. Huzinaga and Y. Sakai, *J. Chem. Phys.* **50**, 1371 (1969).
22. *Gaussian Basis Sets for Molecular Calculations*; S. Huzinaga, Ed.; Elsevier: New York, 1984.
23. M. Kaupp, M. Dolg, H. Stoll, and H. G. von Schnering, *Inorg. Chem.* **33**, 2122 (1994).
24. M. Dolg, U. Wedig, H.Stoll, and H. Preuss, *J. Chem. Phys.* **86**, 866 (1987).
25. R. F. Bacher and S. Goudsmit, *Atomic Energy states*, New York and London, 1932.

Appendix B: Theoretical Studies of II-VI Semiconductor Surfaces

B.1 Introduction

Quantum chemical calculations have long been recognized as a powerful tool to accurately predict structures, vibrational frequencies, electronic properties, and reaction energetics for molecules in the gas phase. This approach, however, becomes complicated when used for studying solid-state problems such as surface and bulk properties of crystals because of the infinite dimensions (relative to the scale of molecules) of the solid systems. To account for the periodic nature of these systems, first principles band methods with local density approximation (LDA)[1] are normally used for lattice constant, bulk modulus, and energy calculations. Local interactions can also be studied by using atomic-like functions (e.g., Gaussian basis functions) in the approximation. Nevertheless, these calculations are usually very demanding computationally, and the accuracy level cannot be improved beyond the approximation of LDA. Another problematic aspect of periodic approach is that when dealing with local phenomena such as impurities or defects, very large unit cells will have to be used in order to avoid interferences between neighboring local sites which are created artificially due to the periodic boundary conditions, and thus again increases computational difficulty.

The idea of using finite atomic clusters to simulate bulks and surfaces is popular among chemists mainly because sophisticated molecular orbital methods can be applied to these clusters the same way as to gas-phase molecules. The local geometrical and electronic structures of solids or surfaces can be investigated with the well-established techniques that have been used on molecules. Surface chemisorption reactions can be examined microscopically through the same concept as in intermolecular interactions. However, several factors have to be taken into account

before a surface model can be used successfully. When finite clusters are employed, the electronic structure of the site of interest should approach the characteristics in the infinite case as close as possible. Using cluster models to simulate infinite solids can cause problems in delocalized systems such as metals because of the artificially imposed termination of the models, which simply ignores long-range effects. It has been shown in an iron surface model study that with a 66-atom Fe cluster, the edge effects were still sensible.[2] On the other hand, covalent and ionic solid systems such as semiconductors and oxides are very suitable for cluster studies because electronic structures in these systems are fairly localized. The influences of edges and other local effects are limited to only a small region of space. This is why most cluster modeling studies have been focused on covalent and ionic solids.[3,4] Up until this date, there has not been any theoretical investigation done on $CdTe$ and $HgTe$ surfaces using cluster models. Most of the available structural information has been inferred from reflection high energy diffraction (RHEED) patterns, which do not give details about atomic positions. The very few STM studies[5] so far have not been able to produce high-resolution atomic images. In order to get a clear picture of these surfaces, quantum chemical calculations have been carried out on cluster models to study (001) surface reconstructions and energetics relevant to $Hg_{1-x}Cd_xTe$ (MCT) epitaxial growth.

B.2 Surface Cluster Model Construction

One thing that distinguishes the surface from the bulk is that a surface is coordinate-unsaturated relative to the bulk. There are always dangling bonds present on the surface as a result of bulk termination. A semiconductor surface will reconstruct itself in a way to minimize its surface net charge. It has been shown that simple electron counting models can successfully explain the principle reconstructions found on the surfaces of III-V and II-VI semiconductors.[6] A compound semiconductor surface satisfying the electron counting rule will have all its dan-

gling orbitals from the electropositive element empty and all its dangling orbitals from the electronegative element doubly occupied. This condition is equivalent to no electrons in the conduction band and no holes in the valence band, ending up with a stable semiconducting surface possessing no net surface charges. This electron counting model however does not result in a unique structure. It only gives a number of electronically reasonable reconstructions that a semiconductor surface could have. For a cluster model to represent a semiconductor surface accurately, the first requirement is that the model should also follow the electron counting rule so that it will have the proper electronic characteristics of the real surface. The importance of proper electron counting was demonstrated by Hiraoka and Mashita.[7] In their work, two cluster models, one satisfied the electron counting rule and the other did not, were used to calculate the dimerization of As-stabilized $AlAs(001)$ surface. The cluster with the correct electron count agreed significant better with experiment in both geometrical and electronic structures. The second consideration of constructing the model is to determine the proper cluster size. As the size of the cluster model increases, the edge effects on the electronic properties should become less prominent, and the more realistically it can model the real surface. However from computational point of view, a working cluster model should remain in a manageable size, while at the same time still having an adequate number of atoms to reproduce the surface and bulk characteristics of a real surface structure.

On the ideal (001) surface of a II-VI semiconductor with zinc-blende lattice, each surface atom makes two bonds with the subsurface atoms and has two dangling bond orbitals. In the bulk, each Group IIB atom is bonded to four neighboring Group VI atoms in a tetrahedral arrangement and vice versa. Since the number of valence electrons is 2 for Group IIB and 6 for Group VI, to each II–VI bond the Group IIB atom contributes $\frac{1}{2}$ electrons while the Group VI atom contributes $\frac{3}{2}$ electrons. Hydrogen atoms are normally used to saturated the dangling bonds

resulting from the arbitrary discontinuance of the bulk, with bond lengths kept at the same distances as those in the corresponding Group IIB and VI simple hydride molecules.

The approximation of using hydrogen atoms to tie up dangling orbitals is popular in cluster modeling not only because of the computational simplicity of hydrogen atom, but also because hydrogen is more or less in the middle of the electronegativity scale and can form covalent bonds with most atoms. It should be obvious that the hydride bonds introduced in the cluster will make the local electronic environment somewhat different from that in the bulk. In the semiconductor bulk, one Group IIB atom uses $\frac{1}{2}$ electrons to make bond to each of the four neighboring Group VI atom. However in the cluster, since each hydrogen atom has only one electron available for bonding, the Group IIB atom is forced to use one electron when making bond with the hydrogen and thus artificially creates $\frac{1}{2}$ electrons deficiency as compared to the bulk. For the similar reason, each Group VI hydride bond generates $\frac{1}{2}$ excess electrons as compared to the bulk. Varying the numbers of the two different types of hydride bonds provides a way to manipulate the electronic property of the cluster. If we only allow the surface atoms to relax while keeping everything else in the cluster fixed during a quantum-chemical molecular orbital optimization, the resulting net electronic effect will be reflected on the surface atoms. Therefore in order for the surface atoms in the cluster model to have identical electronic structures as those on the real surface, proper consideration has to be taken in the number of hydride bonds used when constructing the cluster.

In the study of the surface of a compound semiconductor, one also has to consider the possible variations of surface stoichiometry and termination. The difference in the amount of atomic species in the surface layer will almost always result in different electronic structures and reconstructions, so will the identity (cation or anion) of the species. The most commonly observed surface coverages (Θ) for (001)

II-VI semiconductor surfaces are $\Theta = \frac{1}{2}$ and $\Theta = 1$. The cluster models constructed in this study are designed to simulate surfaces under these two conditions.

B.2.1 One-half Monolayer Coverage (001) Surfaces

II-VI (001) surfaces terminated with half-monolayer coverage ($\Theta = \frac{1}{2}$) of Group IIB or VI atoms should exhibit $p(2 \times 1)$ or $c(2 \times 2)$ reconstruction. This has been experimentally confirmed for the cation terminated case[8,9] but not for the anion terminated case, which may not form a stable surface under the $\Theta = \frac{1}{2}$ condition. If we consider the cation terminated case, each surface Group IIB atom again bonds to two sub-surface Group VI atoms and ends up having 2 dangling orbitals and $2 \times \frac{1}{2} = 1$ available non-bonding electron. Each sub-surface Group VI atom now has one dangling orbital and $1 \times \frac{3}{2} = \frac{3}{2}$ non-bonding electrons. According to the electron counting model, it is not energetically favorable for atoms to have partially filled orbitals in the semiconductor surface layer. Since there are twice as many sub-surface Group VI atoms as surface Group IIB atoms, electron transfer can occur from each surface Group IIB atom to two sub-surface Group VI atoms, resulting in doubly occupied anion dangling orbitals and empty cation dangling orbitals. This is the criteria for being a stable surface according to the electron counting rule. By rearranging the available electrons in the surface layer, the surface thus can become stable. To avoid surface electronic structure modifications cause by hydrogen atoms introduced in the cluster, equal numbers of Group IIB and VI hydride bonds should be used when constructing the cluster so that the hydride bond effects will cancel out on each other. Figure B.1 is the schematic view of the $\Theta = \frac{1}{2}$ $c(2 \times 2)$ cation terminated (001) surfaces and its cluster model. There are 8 Group IIB , 8 Group VI, and 20 H atoms in the cluster, which was constructed to have C_{2v} symmetry for computational benefits. All the Group IIB and VI atoms within the cluster are fixed at the bulk positions, preserving bulk bond distances and angles. This cluster is denoted as $C1$. The anion terminated cluster can be

(a)

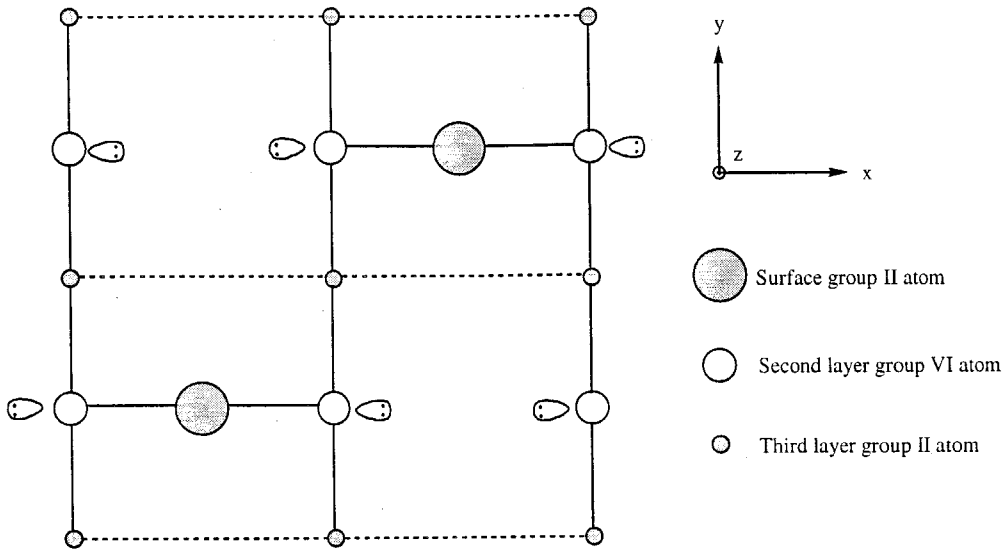

(b)

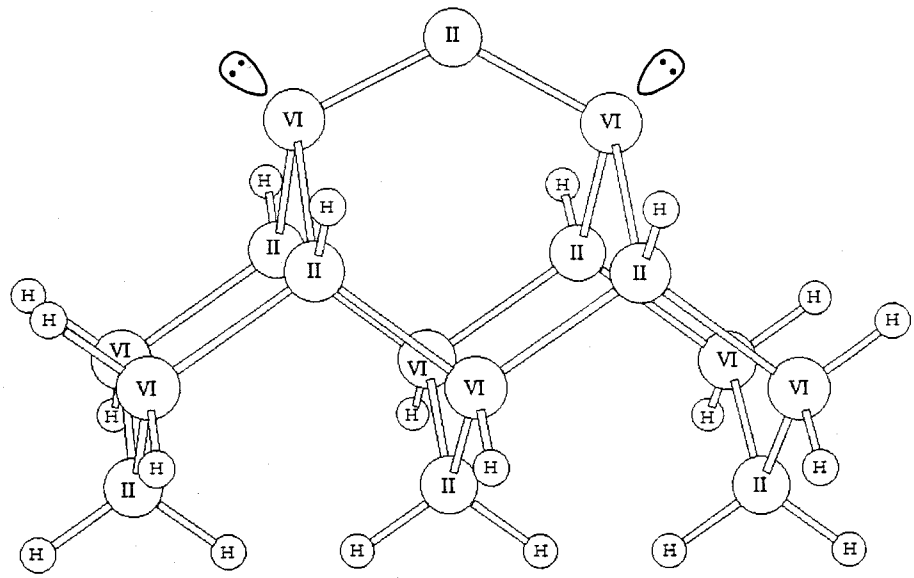

Figure B.1. (a) Cation terminated II-VI $c(2\times 2)$ surface . (b) $II_8VI_8H_{20}$ cluster $C1$ surface model.

obtained by simply exchanging the positions of all Group IIB and VI atoms from the cation terminated surface cluster. The surface Group IIB atom in this cluster has two empty orbitals, resulting from electron transfer to the sub-surface Group VI atoms. This cluster can be used to model either $p(2 \times 1)$ or $c(2 \times 2)$ surface.

B2.2 Full Monolayer Coverage (001) Surfaces

The electronic structure on the full monolayer coverage ($\Theta = 1$) (001) surface should also follow the electron counting rule, and is expected to be different from that on the $\Theta = \frac{1}{2}$ surface. When the surface is fully terminated with Group IIB atoms, each group II atom will use $2 \times \frac{1}{2} = 1$ electron for bonding to the second layer Group VI and will have $2 - 1 = 1$ electron left for the two dangling bond orbitals, which can be rationalized as one orbital singly occupied and one orbital empty. Since all the sub-surface Group VI atoms are coordinately saturated, electron transfer from the surface Group IIB thus cannot occur. Therefore, every two singly occupied dangling orbitals on the surface may have to pair up with each other and form a dimer bond so as to lower the doubly occupied bonding orbital out of the conduction band region. Through this type of reconstruction the surface is able to maintain semiconducting just like the bulk. In the case of Group VI terminated surface, the bonding configuration is the same for the group VI atom except that each surface atom now has only $6 - 2 \times \frac{3}{2} = 3$ electron remaining in the dangling bond state. This amounts to one singly occupied and one doubly occupied orbitals. For the same reason, every two surface Group VI atoms may also pair up the singly occupied dangling orbital to form a dimer bond and thus raises the energy level of the empty anti-bonding orbital out of the valence band region.

Theoretically the surface atoms can dimerize either asymmetrically to form $c(2 \times 2)$ unit cells or symmetrically to form $p(2 \times 1)$ unit cells. The $p(2 \times 1)$ dimerization is confirmed by the experimental reconstructions of $ZnSe$ and $CdTe$ (001) anion terminated surfaces,[10,11] while the $c(2 \times 2)$ reconstruction has not been

observed yet. Plane-wave calculations by Chadi et al. have indicated that $c(2 \times 2)$ is unstable with respect to $p(2 \times 1)$ on the $ZnSe$ (001) surface,[12] which is probably due to the strain induced on the second layer atoms.

Figure B.2 illustrates the $\Theta = 1$ $p(2 \times 1)$ (001) cation dimerized surface and its cluster model. For the cluster shown, each surface Group IIB atom itself has 2 dangling orbitals and 1 available electrons. just like the real (001) surface atom. As in the case of one-half monolayer coverage, there is no need to modify the cluster surface electronically through hydrides. Therefore. equal numbers of Group IIB and VI hydride bonds should also be used when constructing the cluster. resulting in no net electronic effect. There are 7 Group IIB atoms, 8 Group VI atoms, and 20 H atoms in the cluster, which again has C_{2v} symmetry. This cluster can be conveniently obtained from removing the top surface atom off the one-half monolayer anion terminated cluster ($C1$), and is denoted as $C2$. The anion terminated surface also can be modeled simply by just exchanging the positions of all Group IIB and VI atoms from the cation terminated cluster model. The only difference is that each surface Group VI now atom has a doubly occupied orbital instead of an empty orbital.

B.3 Computational Method

The current computational limitations do not allow for elaborate CI calculations on large molecules such as the clusters in Fig B.1 and B.2. Therefore compromise between accuracy and computability has to be made. Based on the results on Hg compounds calculations in Chapter II, it is found that reasonable geometries can be obtained at the HF/12B level while B3LYP/20A(2f) gives good energy results. In the current cluster calculation we used 12B plus Hay and Wadt's (3s3p/3s2p) basis set and $[Kr4d^{10}]$-core ECP[13] for Te to perform geometry optimization at the HF level. For comparison purpose, B3LYP geometries were also calculated. Energetics then were calculated at the B3LYP/20A(2f) level, with Te

(a)

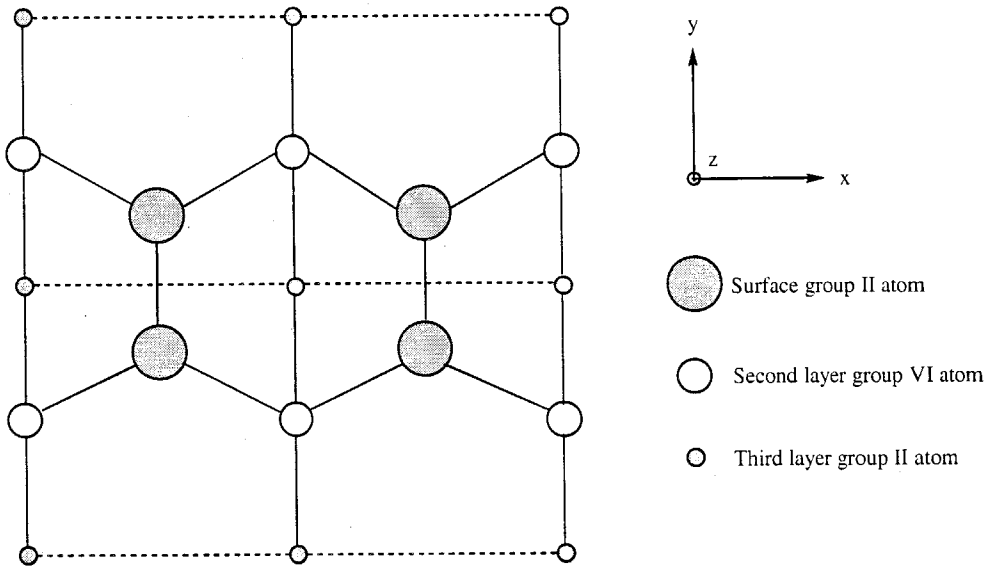

(b)

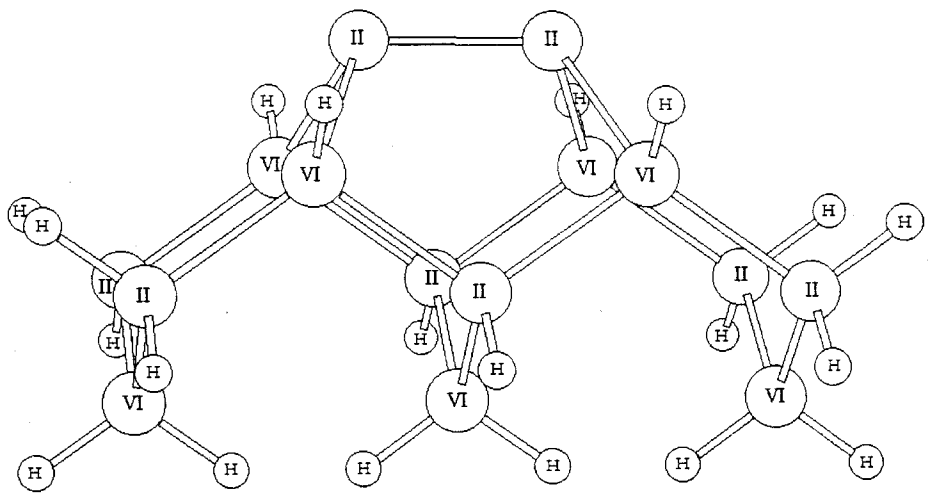

Figure B.2. (a) Cation terminated II-VI $p(2\times1)$ surface . (b) $II_8VI_7H_{20}$ cluster $C2$ surface model.

using the (3s3p4d/3s3p3d) basis set and $[Kr]$-core ECP from Christiansen et al.,[14] augmented with two sets of f polarization functions (exponents of 3.12 and 1.21). This amounts to overall TZDP basis for energy calculations.

B.4 Result and Discussion

B.4.1 Surface Reconstructions of the $\Theta = \frac{1}{2}$ Surfaces

B.4.1.1 The $c(2 \times 2)_{Cd}$ Reconstruction on $CdTe$ (001) Surface

We first carried out surface reconstruction calculations on one-half Cd monolayer $CdTe$ (001) surface using the cluster $C1$. Both $c(2 \times 2)$ and $p(2 \times 1)$ reconstruction patterns have been observed experimentally for this surface. They often co-exist to form a mixed $c(2 \times 2) - p(2 \times 1)$ phase.[15] Even though the two reconstructions should not be very different from each other due to their similar bonding considerations, in an exact sense $C1$ would represent $c(2 \times 2)$ better than $p(2 \times 1)$ because the surface atom in $C1$ does not have an adjacent neighbor, which is just like in the $c(2 \times 2)$ case. Only the surface and sub-surface atoms were allowed to relax during geometry optimization. The results are listed in Table B.1. The surface Cd atom relaxes towards the sub-surface Te atoms, increasing the $Te{-}Cd{-}Te$ bond angle. The calculated surface $Te{-}Cd{-}Te$ angle $\theta_{TeCdTe} = 156.4°$ (HF) or 160.2° (B3LYP), which is much larger than the ideal tetrahedral angle in the bulk. This bond angle reflects the tendency toward the 180° angle of free Cd compounds. The surface $Cd{-}Te$ bond $R_{CdTe} = 2.699$ Å (HF) or 2.763 Å (B3LYP), which is smaller than the bulk value 2.806 Å. This is expected since the surface $Cd{-}Te$ bond has bond order BO = 1 while the bulk BO = $\frac{1}{2}$ only. This decrease in surface bond length was also observed experimentally in the TEM study.[16] The calculated sub-surface $Te{-}Cd$ bond 2.856 Å (HF) or 2.924 Å (B3LYP) is longer than the bulk bond distance. This result agrees with the two-dimensional periodic boundary condition GDS/DFT study on the $CdTe$ slab,[1] and may be due to the electron transfer

Table B.1. Atomic Relaxations in the $c(2 \times 2)_{Cd}$ $CdTe(001)$ Surface

	HF	B3LYP	Bulk Value
		Surface bond	
R_{CdTe}	2.699 Å	2.763 Å	2.806 Å
$\Delta R_{CdTe}{}^a$	-0.107 Å	-0.043 Å	–
θ_{TeCdTe}	156.4°	160.2°	109.5°
		Sub-surface bond	
$R_{TeCd}{}^a$	2.865 Å	2.924 Å	2.806 Å
ΔR_{TeCd}	0.059 Å	0.118 Å	–

[a] Difference between calculated bond length and bulk value.

from the surface Cd to the sub-surface Te. The B3LYP bond lengths appear to be longer than the HF bond lengths in both surface and sub-surface bonds. This is consistent with the finding in Chapter II that B3LYP always overestimates bond distances. We believe that for the current calculation, HF geometries are more reliable than the B3LYP ones. The schematic representation and the displacements of surface atomic positions from HF results are illustrated in Figure B.3.

B.4.1.2 The $c(2 \times 2)_{Hg}$ Reconstruction on $HgTe$ (001) Surface

The recent RHEED study from Landwehr et al.[17] has shown that under Hg rich conditions, $HgTe$ (001) surface also adapts the $c(2 \times 2)_{Hg}$ ($\Theta = \frac{1}{2}$) reconstructed structure. Table B.2 summarizes the geometry optimization results for $HgTe(001)_{Hg}$ surface, which are very similar to those in the $CdTe$ case. The $Te{-}Hg{-}Te$ bond angle $\theta_{TeHgTe} = 161.4°$ (HF) or 163.8° (B3LYP), which is larger than the calculated θ_{TeCdTe}. This should be expected due to the larger separation of Hg $6s$ and $6p$ energy levels than for Cd, which results in more a difficult sp^2

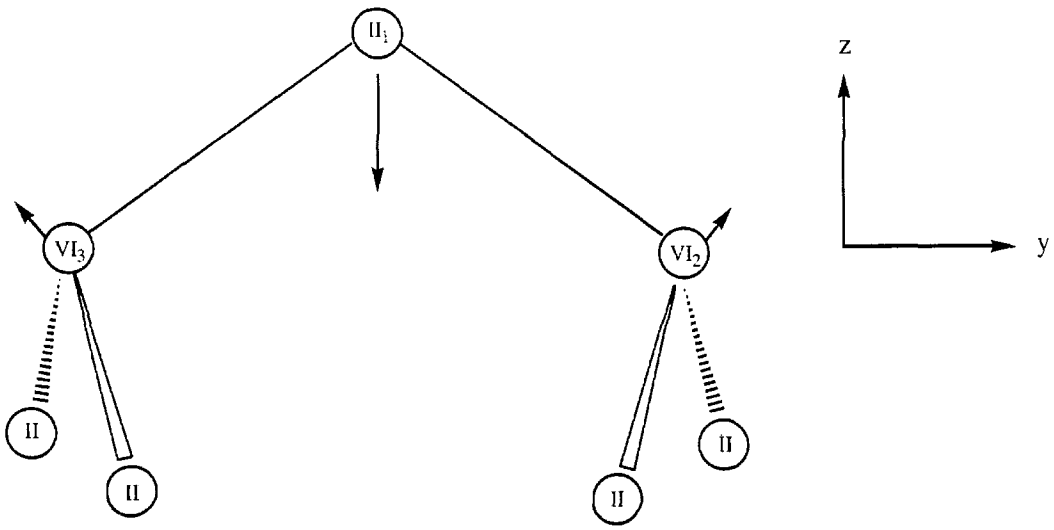

	Atom	Δy (Å)	Δz (Å)
CdTe $c(2\times2)_{Cd}$			
	II_1	0.000	-1.004
	VI_2	0.351	0.064
	VI_3	-0.351	0.064
HgTe $c(2\times2)_{Hg}$			
	II_1	0.000	-1.048
	VI_2	0.388	0.129
	VI_3	-0.388	0.129

Figure B.3. Displacements of surface atoms from their bulk positions in cation terminated II-VI $c(2\times2)$ surfaces .

hybridization for Hg. There is discrepancy between the HF calculated surface bond distance R_{HgTe} = 2.709 Å and B3LYP calculated R_{HgTe} = 2.807 Å. The latter is actually about 0.01 Å larger than the bulk value 2.798 Å, which is not consistent with the $CdTe$ case and the GDS/DFT study.[1] This again demonstrates the overestimation of bond length by B3LYP. The calculated sub-surface bond distance R_{TeHg} = 2.901 Å (HF) or 3.006 Å (B3LYP) is larger than the bulk bond distance as in the case of $CdTe$. The surface atomic displacement details from HF calculations can be found in Figure B.3.

Table B.2. Atomic Relaxations in the $c(2 \times 2)_{Hg}$ $HgTe(001)$ Surface

	HF	B3LYP	Bulk Value
		Surface bond	
R_{HgTe}	2.709 Å	2.807 Å	2.798 Å
$\Delta R_{HgTe}{}^{a}$	-0.089 Å	0.009 Å	–
θ_{TeHgTe}	161.4°	163.8°	109.5°
		Sub-surface bond	
$R_{TeHg}{}^{a}$	2.901 Å	3.006 Å	2.798 Å
ΔR_{TeHg}	0.103 Å	0.208 Å	–

[a] Difference between calculated bond length and bulk value.

B.4.1.3 The $c(2 \times 2)_{Te}$ Reconstruction on $CdTe$ (001) Surface

The surface bonding arrangement of $c(2 \times 2)_{Te}$ is the same as for $c(2 \times 2)_{Cd}$, with each Te bonding to two sub-surface Cd atoms except that each surface Te here has two doubly occupied dangling orbitals resulting from the electron transfer of the second layer Cd atoms. Geometry optimization results (in Table B.3) show that the Te relaxes away from the surface, reducing the $Cd{-}Te{-}Cd$ bond angle. The calculated surface $Cd{-}Te{-}Cd$ angle θ_{CdTeCd} = 85.1° (HF) or 82.2°

(B3LYP) deviates considerably from the tetrahedral bulk value and is also smaller than the molecular value of TeH_2 (90.2 °). The reason may be that, in addition to the tendency of the surface Te to resemble free molecular Te because of similar bonding configuration, the decrease in the surface $Cd{-}Te{-}Cd$ bond angle may be further caused by the second layer Cd's preference to become planar (sp^2) from the tetrahedral (sp^3) arrangement, as shown in Figure B.4. To compare with other theoretical studies, a similarly small $Zn{-}Se{-}Zn$ angle (82°) on the $ZnSe$ (001) surface was also found by using plane-wave calculations.[11] The calculated surface bond length 2.699 Å (HF) or 2.763 Å (B3LYP) is shorter than the bulk 2.806 Å, which is expected because of the larger BO of the surface bond. The sub-surface bond length from the calculation, as in the cation terminated case, is longer than the bulk value. This may be again due to the charge transfer that occurred in the surface layer.

Table B.3. Atomic Relaxations in the $c(2 \times 2)_{Te}$ $CdTe(001)$ Surface

	HF	B3LYP	Bulk Value
		Surface bond	
R_{TeCd}	2.721 Å	2.778 Å	2.806 Å
$\Delta R_{TeCd}{}^a$	-0.085 Å	-0.082 Å	–
θ_{CdTeCd}	85.1°	82.2°	109.47°
		Sub-surface bond	
$R_{CdTe}{}^a$	2.984 Å	3.047 Å	2.806 Å
ΔR_{CdTe}	0.178 Å	0.241 Å	–

[a] Difference between calculated bond length and bulk value.

One would argue that because of the lone pair repulsion between adjacent Te atoms (each has two lone pairs), the $\Theta = \frac{1}{2}$ Te-rich surface would prefer $c(2 \times 2)$

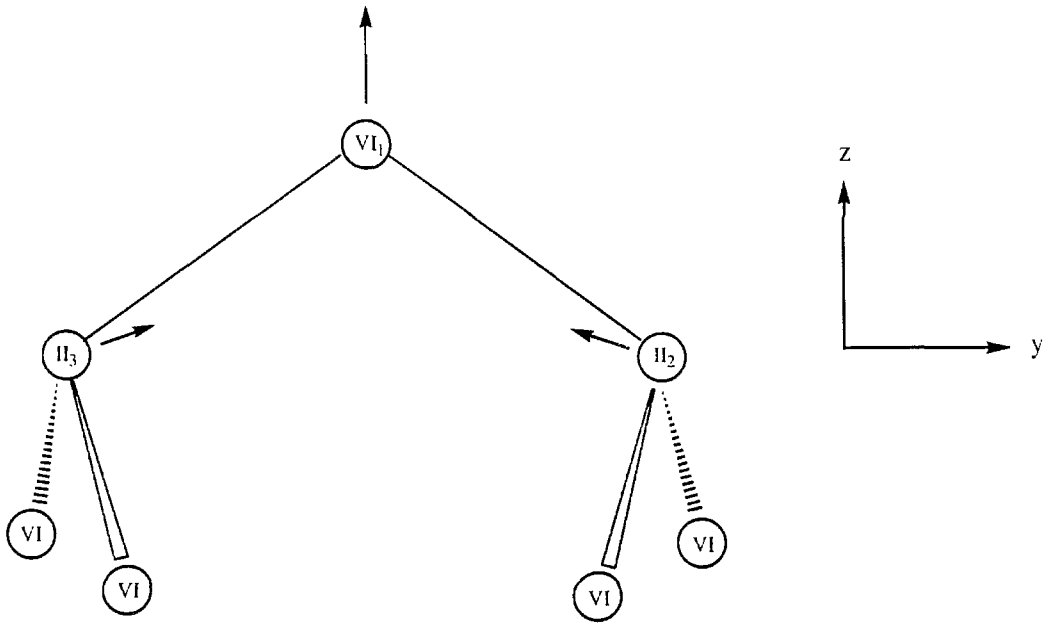

	Atom	Δy (Å)	Δz (Å)
CdTe $c(2\times2)_{Te}$			
	VI_1	0.000	0.623
	II_2	-0.450	0.239
	II_3	0.450	0.239
HgTe $c(2\times2)_{Te}$			
	VI_1	0.000	0.734
	II_2	-0.482	0.277
	II_3	0.482	0.277

Figure B.4. Displacements of surface atoms from their bulk positions in Te terminated II-VI $c(2\times2)$ surfaces .

over $p(2 \times 1)$. Our current cluster study cannot distinguish between the two. This will have to be resolved through total-energy band calculations. Nevertheless, the fact is that neither surface is stable against $\Theta = 1$ dimerized $p(2 \times 1)_{Te}$ surface, which is the surface observed experimentally under Te terminated conditions. We think that the instability of the $\Theta = \frac{1}{2}$ surfaces may be due the outward relaxation (0.623 Å) of surface Te away from these surfaces (Figure B.4). Because of the charge transfer from sub-surface Cd to Te, this outward movement would create larger surface dipole moment and thus increases the surface energy. For cation terminated surfaces we have an exact opposite situation. The surface cation relaxes toward the surface, reducing the surface dipole moment. The may explain why $\Theta = \frac{1}{2}$ $c(2 \times 2)$ or $p(2 \times 1)$ surfaces are commonly observed in $CdTe$ and $HgTe$ under cation-rich conditions but never under anion-rich conditions.

B.4.1.4 The $c(2 \times 2)_{Te}$ Reconstruction on $HgTe$ (001) Surface

The reconstruction found on $HgTe$ (001) surface is very similar to the $CdTe$ case. The geometry optimization results are summarized in Table B.4. The calculated surface $Hg{-}Te{-}Hg$ angle $\theta_{HgTeHg} = 82.0°$ (HF) or 80.0° (B3LYP) is somewhat smaller than the corresponding angle θ_{CdTeCd} found in $CdTe$. The may be due to the slightly stronger tendency of the second layer Hg (than Cd) to become co-planar with its three nearest Te neighbors. The overestimation of B3LYP bond length is again demonstrated by the longer calculated surface bond distance R_{TeHg} (2.839 Å) than the bulk value (2.798 Å). The larger outward relaxation (0.734 Å) of surface Te than for the $CdTe$ case may predict this surface to be even more unstable against the $\Theta = 1$ dimerized surface.

B.4.2 Surface Reconstructions of the $\Theta = 1$ Surfaces

The Optimized Geometries of the $\Theta = 1$ $p(2 \times 1)(001)$ Surfaces of $CdTe$ and $HgTe$ using cluster the $C2$ are summarized in Table B.5. Only the top two

Table B.4. Atomic Relaxations in the $c(2 \times 2)_{Te}$ $HgTe(001)$ Surface

	HF	B3LYP	Bulk Value
		Surface bond	
R_{TeHg}	2.746Å	2.839 Å	2.798Å
$\Delta R_{TeHg}{}^{a}$	-0.052 Å	0.041Å	–
θ_{HgTeHg}	82.0°	80.0°	109.47°
		Sub-surface bond	
$R_{HgTe}{}^{a}$	3.005 Å	3.116 Å	2.798 Å
ΔR_{HgTe}	0.207 Å	0.318 Å	–

[a]Difference between calculated bond length and bulk value.

surface atoms within the cluster were allowed to move during optimization. Dimer formation was found on each surface. The schematic description of surface atomic displacements can be found in Figure B.5.

B.4.2.1 The $p(2 \times 1)_{Cd}$ Reconstruction on $CdTe$ (001) Surface

The calculated $Cd{-}Cd$ bond length is 2.759 Å (HF) or 2.860 Å (B3LYP), which is significantly shorter than the corresponding bulk distance 4.582 Å of the two Cd atoms. This result indicates that the dimer formation indeed occurs. Comparing the dimer bond length to the calculated $Cd{-}Cd$ bond distance of the molecule $HCd{-}CdH$ 2.781 Å (HF) or 2.866 Å (B3LYP) indicates that the surface dimer bond should have a very similar character of the two-electron $Cd{-}Cd$ covalent bond (BO = 1). This $p(2 \times 1)_{Cd}$ dimerized surface, however, has never been observed experimentally. All experimental evidences have shown that $CdTe(001)$ surface under Cd-rich conditions prefers the $c(2 \times 2)$ or $p(2 \times 1)$ ($\Theta = \frac{1}{2}$) arrangement. This is probably due to the fact that on the $\Theta = \frac{1}{2}$ surface, Cd undergoes a near

Table B.5. Atomic Relaxations in the $CdTe$ and $HgTe$ $p(2\times1)(001)$ Surfaces

	HF	B3LYP	Bulk Value
		(1) $CdTe(001)_{Cd}$	
R_{CdCd}[a]	2.759 Å	2.860 Å	4.582 Å
ΔR_{CdCd}[b]	-1.823 Å	-1.722 Å	–
R_{CdTe}[c]	3.053 Å	3.129 Å	2.806 Å
ΔR_{CdTe}[b]	0.247 Å	0.323 Å	–
		(2) $HgTe(001)_{Hg}$	
R_{HgHg}[a]	2.747 Å	2.951 Å	4.569 Å
ΔR_{HgHg}[b]	-1.822 Å	-1.618 Å	–
R_{HgTe}[c]	3.059 Å	3.231 Å	2.798 Å
ΔR_{HgTe}[b]	0.261 Å	0.433 Å	–
		(3) $CdTe(001)_{Te}$	
R_{TeTe}[a]	2.915 Å	3.249 Å	4.582 Å
ΔR_{TeTe}[b]	-1.667 Å	-1.333 Å	–
R_{TeCd}[c]	2.915 Å	2.872 Å	2.806 Å
ΔR_{TeCd}[b]	0.109 Å	0.066 Å	–
		(4) $HgTe(001)_{Te}$	
R_{TeTe}[a]	2.913 Å	3.161 Å	4.569 Å
ΔR_{TeTe}[b]	-1.656 Å	-1.408 Å	–
R_{TeHg}[c]	2.932 Å	2.945 Å	2.798 Å
ΔR_{TeCd}[b]	0.134 Å	0.147 Å	–

[a] Surface dimer bond length.

[b] Difference between calculated bond length and bulk value.

[c] Sub-surface bond length.

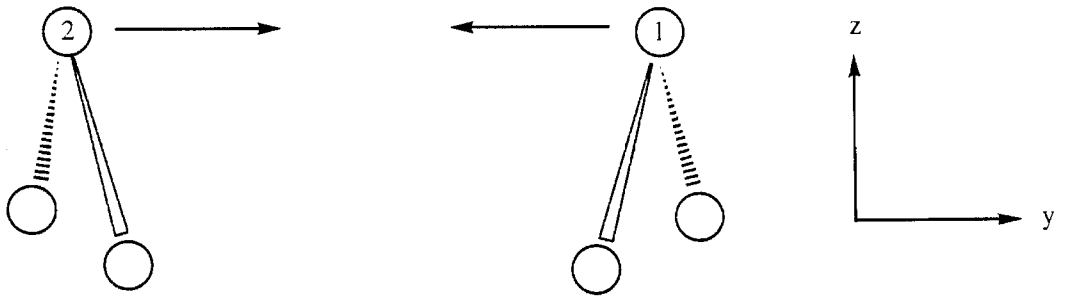

	Atom	Δy (Å)	Δz (Å)
CdTe $p(2\times1)_{Cd}$			
	1	-0.912	0.194
	2	0.912	0.194
HgTe $p(2\times1)_{Hg}$			
	1	-0.911	0.204
	2	0.911	0.204
CdTe $p(2\times1)_{Te}$			
	1	-0.833	-0.022
	2	0.833	-0.022
HgTe $p(2\times1)_{Te}$			
	1	-0.828	-0.026
	2	0.828	-0.026

Figure B.5. Displacements of surface atoms from their bulk positions in II-VI dimerized $p(2\times1)$ surfaces .

sp-hybridization as in its free molecule state, making two covalent bonds with the second layer Te atoms. While under the $\Theta = 1$ condition, each surface Cd atom has to make an additional $Cd{-}Cd$ dimer bond, ending up with an sp^2 hybridization. the sp^2 hybridization is not a preferable bonding configuration for Group IIB atoms. This would thus result in a higher surface energy for the $\Theta = 1$ surface with respect to $\Theta = \frac{1}{2}$ surfaces under Cd-rich conditions. For other geometrical features on this surface, the calculated sub-surface bond distance R_{CdTe} is again larger than the corresponding bulk value.

B.4.2.2 The $p(2 \times 1)_{Hg}$ Reconstruction on $HgTe$ (001) Surface

The dimerization reconstruction of $HgTe(001)_{Hg}$ surface is very similar to that of $CdTe(001)_{Cd}$ surface. The calculated $Hg{-}Hg$ dimer bond length 2.747 Å (HF) or 2.951 Å (B3LYP) is also compatible with the calculated covalent bond distance 2.752 Å (HF) or 2.878 Å (B3LYP) of the molecule $HHg{-}HgH$, indicating the BO = 1. One would expect that this should be even more unstable (than in the $CdTe$ case) with respect to the $\Theta = \frac{1}{2}$ surfaces since Hg would much prefer sp to sp^2 hybridization because of large $6s{-}6p$ energy separation. Indeed this surface has never been observed experimentally.

B.4.2.3 The $p(2 \times 1)_{Te}$ Reconstruction on $CdTe$ (001) Surface

The $p(2 \times 1)_{Te}$ ($\Theta = 1$) reconstruction is the most commonly observed $CdTe$ (001) surface under Te-rich conditions, and was found to have great surface's stability.[15] The surface $Te{-}Te$ dimer bond, unlike the $Cd{-}Cd$ bond in the cation-terminated case, is expected to have π character in addition to the σ bonding, which would make the dimer formation even more favorable. The calculated $Te{-}Te$ dimer bond length 2.915 Å (HF) or 3.249 Å (B3LYP) is very close to the covalent bond distance 2.825 Å (HF) or 3.027 Å (B3LYP) calculated from the molecule $HTe{-}TeH$.

B.4.2.4 The $p(2 \times 1)_{Te}$ Reconstruction on $HgTe$ (001) Surface

As in the case of $CdTe$, the $p(2 \times 1)$ Te dimerized reconstruction is also expected to be stable on the $HgTe(001)$ surface. This surface indeed has been observed experimentally.[17] The calculated surface structure is similar to the $CdTe(001)$ result, with Te dimer bond length 2.913 Å (HF) or 3.161 Å (B3LYP) also close to the molecular value.

B.4.3 Cation Surface Desorption Energies

Besides the surface structures, we have also investigated the desorption energies of surface atoms. We know that if the Te atoms desorb from the $p(2 \times 1)_{Te}$ surface, this process will be complicated by the subsequent desorption of one-half monolayer of cations atoms because $\Theta = 1$ cation terminated surface is not a stable surface. Furthermore, the desorbed Te can undergo reactions to form Te_2, Te_4, and other Te species, making the energetics difficult to study. On the other hand, the desorption of the surface cations from the $c(2 \times 2)$ ($\Theta = \frac{1}{2}$) surface will result in the anion dimer $p(2 \times 1)$ ($\Theta = 1$) surface. Since both surfaces and the free Group IIB atom are all thermodynamically stable, the cation surface desorption energy can be simply calculated the energy difference between these two surfaces. Using $C1$ and $C2$ cluster models we calculated this energy from E($C2$) + E(cation) − E($C1$). The computed desorption energies for Cd and Hg are 1.61 and 0.99 eV, respectively. The Hg desorption energy only accounts for about 60% of Cd desorption energy, which is the combined results of the smaller $Hg{-}Te$ bond energy and larger Hg $6s$ pairing energy gained in desorption. For comparison, the calculated Te desorption energy is 2.87 eV under the same $\Theta = \frac{1}{2}$ condition, although this energy does not have much physical meaning.

The inert nature of Hg atom and the low surface desorption energy may explain why the low Hg sticking coefficient and high Hg vacancy concentrations are encountered in growing MCT materials while no such problems exist for Cd. If

we can somehow modify the energetics of surface Hg species by bonding a ligand R to the Hg so that this $Hg-R$ unit remains bonded throughout surface growth reactions, the Hg reaction probability (sticking coefficient) to the surface will greatly increase because Hg is forced to stay in the reactive ^3P state.

Cluster calculations were carried out to study how strongly $Hg-R$ would react with surface. Since the BO of $Hg-R$ bond is 1, the Hg will only makes another BO = 1 bond to the surface. There are two possible cases for the surface bonding. $Hg-R$ can either make a single BO = 1 bond to the surface Te or bridge over two Te atoms to make two BO = $\frac{1}{2}$ bonds. The result from a separate cluster study[18] indicates that the latter bonding configuration is preferred. In order to account for the somewhat different electronic structure of the surface Te, a new $Hg_8Te_8H_{20}$ cluster modified from cluster $C1$ (denoted as $C3$) was introduced to model the surface bonding. This $C3$ cluster includes one $Hg_{sp^2}-H$ unit in the bulk to replace one regular $Hg_{sp^3}-H_2$ unit in $C1$. What this does electronically to the surface is to provide overall one extra electron to the two surface Te atoms, enabling them to use three electrons make two bonds with HgR, which only contributes one electron. For computational simplicity, we used H to represent the R. Geometry optimization was done at HF level as usual and the optimized cluster structure is depicted in Figure B.6. The calculated $Hg-H$ desorption energy is 2.56 eV, which is much larger than that of the atomic Hg. Based on this result, a novel MOMBE growth strategy for MCT was proposed and is described in detail in Chapter III.

B.5 Conclusion

Surface reconstructions on the $CdTe$ and $HgTe(001)$ surfaces have been investigated using quantum chemical cluster models for the first time. A total of eight different surfaces owing to the variations of surface conditions (surface coverage, cation/anion termination) were elucidated. It is found that the increasing surface dipole energy may be the reason why half-monolayer $c(2 \times 2)_{Te}$ or $p(2 \times$

$1)_{Te}$ is not a stable surface, unlike its cation terminated counterparts. The surface desorption energetics information pertinent to epitaxial growth of $Hg_{1-x}Cd_xTe$ has also been resolved in this study. Due to the limitations of finite clusters, other surface energy issues (e.g., which of $p(2 \times 1)_{Cd}$ and $c(2 \times 2)_{Cd}$ is a more stable surface) will have to be addressed by periodic band calculations. However, the current cluster work can provide useful surface structural information to be used in such calculations.

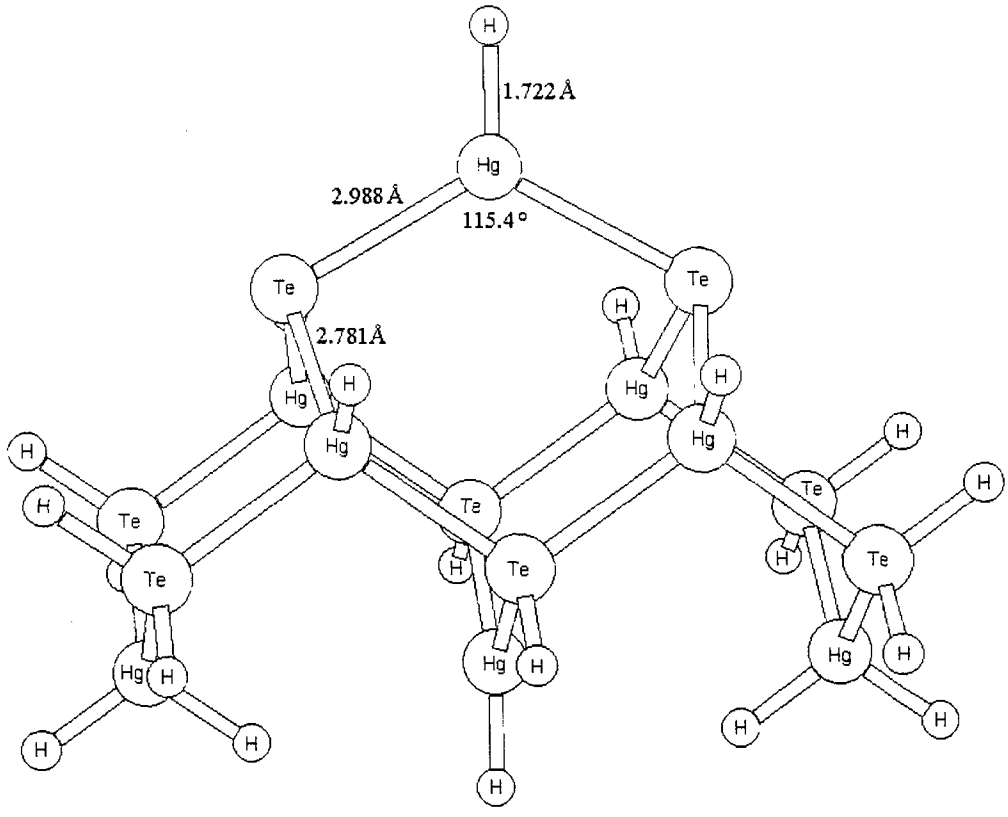

Figure B.6. Optimized geometry of cluster *C3* obtained from modified *C*2 cluster.

Appendix B References

1. X. Chen, A. Mintz, J. Hu, X. Hua, J. Zinck, and W. A. Goddard III, *J. Vac. Sci. Technol.* **B 13**, 1715 (1995).
2. S. P. Walch, *Surf. Sci.* **143**, 188 (1984).
3. M. W. Radny, P. V. Smith, and P. L. Cao, *Surf. Sci.* **351**, 75 (1996).
4. S. Ramachandran, B. L. Tsai, M. Blanco, H. Chen, Y. Tang, and W. A. Goddard III, *J. Phys. Chem. A* **101**, 83 (1997).
5. *Appl. Phys. Lett.* **67**, 1680 (1995).
6. W. A. Harrison *J. Vac. Sci. Technol.* **16**, 1492 (1979).
7. Y. S. Hiraoka and M. Mashita, *J. Crystal Growth* **150**, 163 (1995).
8. K. Menda, I. Takayasu, T. Minato, and M. Kawashima, *Jpn. J. Appl. Phys.* **26**, L1326 (1987).
9. H. H. Farrel, M. C. Tamargo, S. M. Shibli, and Y. Chang, *J. Vac. Sci. Technol.* **B8**, 884 (1990).
10. S. Tatarenko, F. Bassani, J. C. Klein, K. Saminadayer, J. Cibert, and V. H. Etgen, *J. Vac. Sci. Technol.* **A12**, 140 (1994).
11. D. Li and D. Pashley *J. Vac. Sci. Technol.* **B12**, 2547 (1994).
12. C. H. Park and D. J. Chadi, *Phys. Rev.* **B49**. 16467 (1994).
13. P. J. Hay and W. R. Wadt, *J. Chem. Phys.* **82**, 299 (1985).
14. L. A. LaJohn and P. A. Christiansen, *J. Chem. Phys.* **87**, 2812 (1987).
15. M. B. Veron, V. H. Etgens, M. Sauvage-Simkin, S. Tatarenko, B. Daudin, and D. Brun-Le Cunff, *J. Crystal Growth* **159**, 694 (1996).
16. P. Lu and D. J. Smith, *Surf. Sci.* **254**, 119 (1991).
17. S. Oehling, M. Ehinger, W. Spahn, A. Waag, C. R. Becker, and G. Landwehr, *J. Appl. Phys.* **79**, 748 (1996).
18. B. L. Tsai and W. A. Goddard III, unpublished work.

Appendix C: Molecular Bonding in Group II-VI Complexes

C.1 Introduction

In Appendix B we used finite cluster models to study the reconstructions and desorption energetics of II-VI semiconductor surfaces. These calculation results demonstrate "molecular-like" features on the surfaces, i.e., the geometrical and electronic structures of these surfaces are shown to be heavily determined by molecular bonding. This observation is not too surprising since bondings in II-VI semiconductors are considered mostly covalent. The purpose of this appendix is to find out how far this molecular bonding concept can be extended to understand solid-state phenomenon such as surface vacancy and bulk cohesive energies by studying the bonding of Group IIB-VI simple molecular complexes. In the following sections we will first discuss the bonding in Group IIB (Zn, Cd, Hg) and VI (Te) hydrides. Then the bonding in simple molecular complexes containing II-VI covalent bonds will be examined and compared with cluster results. We used the same level of theory (TZDP basis sets plus B3LYP/DFT theory, as described in Appendix B.) to do all the calculations on molecules in order to ensure a meaningful comparison with the cluster study.

C.2 The Bonding in Group IIB Hydrides and TeH_2

C.2.1 Group IIB Hydrides

The bonding characteristics of Group IIB divalent compounds have been studied in detail in Chapter II. Here we only recap a few relevant points from that study for the sake of completeness of the current ongoing discussion. Since the two valence electrons of the ground state Group IIB atom are already spin paired, we cannot form an ordinary covalent bond to it. Instead we have to first promote the Group IIB atom to the $(ns)^1(np)^1$ excited state configuration with two singly-

occupied orbitals. These orbitals can then be hybridized into $sp = ns + np$ and $\bar{sp} = ns - np$ orbitals in, say the z direction, to form two covalent bonds. When bonding to two H atoms this leads to a linear $H-M-H$ compound. Dissociating one H from $H-M-H$ leads to the fundamental bond energy, $D_2 = D_{MH}$. Breaking the second bond leads to a much weaker bond energy $D_1 = D_{MH} - P_M$, where P_M is the pairing energy of the ns^2 electrons. The reason is that upon breaking this $M-H$ bond the free M atom can relax from the $(ns)^1(np)^1$ configuration to the ground state $(ns)^2$ configuration, leading to a stabilization by P_M. One may try to estimate the value of P_M from the atomic excitation energy as $P_M^{at} = E(^3P) - E(^1S)$. This however, as shown in Chapter II, is not entirely true. Even though P_M and P_M^{at} are related quantities, the molecular value is always weaker than this atomic estimate because of the resonance between the s^2 and sp configurations in the molecular state. Table C.1 lists the pairing energies alone with atomic excitation energies for the Group IIB elements. The promotion energy P for Hg is particularly large because the relativistic effects are important for Hg, stabilizing the $6s$ orbitals with respect to $6p$ orbitals.

Table C.1. Calculated P_M From Hydrides and Atomic P_M^{at} (in eV)

	Zn	Cd	Hg
P_M	2.54	2.39	2.88
P_M^{at} [a]	4.01	3.73	4.67

[a] Data from reference 2.

C.2.2 TeH_2

The ground state of the Te atom has a $(5s)^2(5p)^4$ valence configuration, leading to a ^3P ground state with two singly-occupied orbitals readily available for making two covalent bonds. Each singly-occupied p orbital can bond to the

unpaired p orbital of another atom (in the current case, H) to form a covalent bond. Since the two unpaired p orbitals are pointing at 90° with respect to each other, the bond angle is expected to be $\sim 90°$. Indeed for TeH_2 the bond angle was calculated to be 90.3° (90.2° from experiment[2]). Dissociating one H from TeH_2 leads to the bond energy

$$D\left(HTe - H\right) = 3.18 \text{ eV} = D_{TeH} \tag{C.1}$$

where we denote D_{TeH} as the fundamental bond energy of TeH_2. Breaking the second bond is easier with a smaller bond energy

$$D\left(H - Te\right) = 2.85 \text{ eV} = D_{TeH} - \kappa_{Te}, \tag{C.2}$$

where $\kappa_{Te} = 0.33$ eV. The reason for this weaker bond is that Te atom has two unpaired p orbitals, leading to the exchange stabilization of the triplet state (^3P). In the triplet state the two unpaired p electrons (say p_x and p_y) always have the same spin (say α). However, for TeH the orbital of Te (say p_x) bonded to the H has β spin half the time so there is no longer a correlation between the spins associated with p_x and p_y. The same is true for TeH_2. The resulting effect is that Te atom is stabilized by an extra unit of atomic exchange energy κ over TeH and TeH_2. This leads to a TeH bond ($C.2$) weaker by κ than the first bond ($C.1$) in TeH_2. This atomic exchange stabilization can be estimated from the atomic spectra as[2]

$$\kappa_{Te} = \frac{1}{4}\left[E\left(^1D\right) - E\left(^3P\right)\right] = 0.33 \text{ eV}, \tag{C.3}$$

which is exactly the same as the computed value. The results for Se and S are similar: $\kappa_{Se} = 0.30$ eV and $\kappa_S = 0.29$ eV.[2]

C.3 The Bonding II-VI Molecular Complexes

C.3.1 II-VI Covalent Bonds

With the understanding of bonding characteristics of Group IIB and VI, we can start looking into II-VI molecular complexes. Replacing both H in TeH_2 with HgH leads to the $Te(HgH)_2$ compound. The calculated Te bond angle $\theta_{HgTeHg} = 96.7°$ and the Hg bond angle $\theta_{TeHgH} = 177.6°$. with

$$D_{TeHg} = 2.55 \text{ eV}$$
$$\kappa_{Te} = 0.12 \text{ eV} \qquad (C.4)$$

The difference in κ_{Te} from the κ_{Te} of TeH_2 is due to a different amount of charge transfer in the valence bonds. Removing Te from $Te(HgH)_2$ but without bonding of the two HgH fragments, leads to the snap vacancy energy for Te

$$2D_{TeHg} - \kappa_{Te} = 4.98 \text{ eV} \qquad (C.5)$$

Now let us consider a different II-VI complex. Replacing the H in HgH_2 with TeH leads to $Hg(TeH)_2$ with Hg bond angles $\theta_{TeHgTe} = 180.0°$ and Te bond angle $\theta_{HgTeH} = 89.3°$. Bond energy calculations lead to

$$D_{HgTe} = 2.17 \text{ eV}$$
$$P_{Hg} = 2.01 \text{ eV} \qquad (C.6)$$

The same bond analysis was done for $Zn{-}Te$ and $Cd{-}Te$ covalent bonds. All these results are summarized in Table C.2 and C.3.

C.3.2 II-VI Donor Acceptor Bonds

The TeH_2 and HgH_2 molecules cannot form additional covalent bonds because they are already covalently fully satisfied. However, Hg has two empty orbitals (say $6p_x$ and $6p_z$) while TeH_2 has two lone pair orbitals (say $5s$ and $5p_z$). Thus it is possible for these two molecules to form Lewis acid-base or donor-acceptor (DA) bonds. We have calculated that the optimal structure for the $(H_2Te)\cdots(HgH_2)$

Table C.2. Calculated Energy Terms (eV) for $Te(MH)_2$ (M = Hg, Cd, Zn)

	$Te{-}HgH$	$Te{-}CdH$	$Te{-}ZnH$
$D_2 = D(HMTe{-}MH)$	2.55	2.58	2.61
$D_1 = D(HM{-}Te)$	2.43	2.44	2.46
$\kappa = D_2 - D_1$	0.12	0.14	0.15
$D_2 + D_1 - \kappa$	4.86	4.88	4.92

Table C.3. Calculated Energy Terms (eV) for $M(TeH)_2$ (M = Hg, Cd, Zn)

	$Hg{-}TeH$	$Cd{-}TeH$	$Zn{-}TeH$
$D_2 = D(HTeM{-}TeH)$	2.17	2.36	2.54
$D_1 = D(HTe{-}M)$	0.16	0.55	0.56
$P = D_2 - D_1$	2.01	1.81	1.98
$D_2 + D_1 - P$	0.32	1.18	1.10

complex under C_{2v} symmetry where the Hg is in the TeH_2 plane (along the z axis) and the $H{-}Hg{-}H$ axis perpendicular to this plane. This leads to a DA bond energy

$$DA\,(H_2Te \rightarrow HgH_2) = 0.06 \text{ eV}, \tag{C.7}$$

which is almost negligible. The reason for this small DA bond energy is due to the fact that by making such an bond, the linear $H{-}Hg{-}H$ bonding will have to bend to a certain extent (bond angle calculated to be 178°), increasing the p character in the bonding orbitals in order to accommodate the additional DA bond. Energetically this is very unfavorable for Hg because of the large $s{-}p$ energy separation. The DA bonds energies calculated for Zn and Cd are somewhat larger

because relativistic effects are less pronounced for these two, but the energies still are not very significant compared to covalent bond energies.

$$DA(H_2Te \rightarrow CdH_2) = 0.10 \text{ eV}$$
$$DA(H_2Te \rightarrow ZnH_2) = 0.13 \text{ eV} \qquad (C.8)$$

C.4 Surface Structures and Vacancy Energies of II-VI Semiconductors

The valence bond (VB) description suggests that on the II-VI (001) surface under one-half monolayer Te-rich conditions, the surface Te makes two covalent bonds to the second layer Hg and has dangling bonds with two lone pairs pointing away from the surface. This arrangement makes the bonds between the top two layers more covalent. From the cluster calculation in Appendix B, we find the Te surface angle $\theta_{Hg-Te-Hg} = 82.0°$ and the desorption (vacancy) energy of surface Te is

$$E_{vac}[Te_{surf}] = 2.87 \text{ eV}, \qquad (C.9)$$

where the surface Hg are allowed to bond to each other to form a dimer as the Te is removed. In comparison, the value obtained for the $HHg-Te-HgH$ molecular complex is

$$E_{vac}[Te(HgH)_2] = E(HHgTeHgH) - [E(HHgHgH) + E(Te)] = 2.76 \text{ eV} \quad (C.10)$$

This result suggests that the $Hg-Hg$ bond at the surface formed after Te desorption is strained by $2.87 - 2.76 = 0.11$ eV.

Similarly under half-monolayer Hg-rich conditions, the surface Hg will make two covalent bonds to the second layer Te with two empty orbitals pointing out into the vacuum. The surface Hg bond angle will tend to relax toward the free molecular value of 180°. Using cluster model calculation on this surface we obtain

$\theta_{TeHgTe} = 161.4°$. We also calculated that the energy needed to break both surface $Hg-Te$ bonds is

$$E_{vac}[Hg_{surf}] = 0.99 \text{ eV}, \qquad (C.11)$$

where the surface Te are allowed to bond to each other as the Hg is removed. Compared to the value calculated from the $HTe-Hg-TeH$ complex

$$E_{vac}[Hg(TeH)_2] = E(HTeHgTeH) - [E(HTeTeH) + E(Hg)] = 0.13 \text{ eV}, \quad (C.12)$$

this suggests a surface strain of $0.99 - 0.13 = 0.86$ eV for the $Te-Te$ bond.

In contrast, for Cd the corresponding bond energy are much larger than Hg. We estimated the $Te-Cd-Te$ angle to be 156.4° from cluster calculations. We find that the energy to break both surface bonds is

$$E_{vac}[Cd_{surf}] = 1.61 \text{ eV}, \qquad (C.13)$$

while allowing the surface Te to bond as the Cd is removed. Again if we compare this bond energy with the value obtained from the complex $HTe-Cd-TeH$

$$E_{vac}[Cd(TeH)_2] = E(HTeCdTeH) - [E(HTeTeH) + E(Cd)] = 0.86 \text{ eV}, \quad (C.14)$$

this would suggest a surface strain for $Te-Te$ bond of $1.61 - 0.86 = 0.75$ eV, which is compatible with the $HgTe$ case.

C.5 Bulk Cohesive Energies of II-VI Semiconductors

Since each Te can form two covalent bonds and two DA bonds and each Hg can form two covalent bonds and two DA bonds, we can envision the bonding in bulk $HgTe$ as either

(i) having four equivalent $HgTe$ bonds each with $\frac{1}{2}$ covalent and $\frac{1}{2}$ DA characters.

or

(*ii*) a resonance of a large number of wavefunctions each of which has two covalent and two DA bonds to each Hg and each Te.

This suggests an estimate for the bulk cohesive energy of $HgTe$ as

$$E_{HgTe}^{coh,est} = 2C_{HgTe} + 2DA_{HgTe}, \tag{C.15}$$

where C denotes the average covalent bond (as in an infinite $HgTe$ chain). This leads to

$$E_{HgTe}^{coh,est} = 2E_{HgTe} - \kappa_{Te} - P_{Hg} + 2DA_{HgTe} = 2.71 \text{ eV}, \tag{C.16}$$

where we take E_{HgTe} to be the average value of D_{HgTe} and D_{TeHg}. Similarly, for $CdTe$ this simple VB theory leads to

$$\begin{aligned} E_{CdTe}^{coh,est} &= 3.19 \text{ eV} \\ E_{ZnTe}^{coh,est} &= 3.25 \text{ eV} \end{aligned} \tag{C.17}$$

These estimates from molecular energetics ignore strain and electron delocalization. Compared to the experimental cohesive energies,[3]

$$\begin{aligned} E_{HgTe}^{coh,exp} &= 3.11 \text{ eV} \\ E_{CdTe}^{coh,exp} &= 4.16 \text{ eV} \\ E_{ZnTe}^{coh,exp} &= 4.61 \text{ eV} \end{aligned} \tag{C.18}$$

the molecular values provide an inadequate estimate of the bulk values. They are too small compared to the experiment even though strain energy was not a consideration in the calculation. This result indicates that electron delocalization makes up a significant portion of cohesive energy in the II-VI solid. The resonance effect mentioned in (*ii*) should play an important role. The simple VB theory cannot describe these effects in the semiconductor bulk.

C.6 Conclusion

In this appendix we have attempted to use molecular calculations of simple II-VI complexes to relate to the solid-state properties of II-VI semiconductors. For surface structures and energetics, the VB theory offers a reasonable description mainly due to the fact that the surface has more degrees of freedom to relax itself toward the molecular covalent state. For bulk properties such as cohesive energy where electron delocalization is important, the mere VB consideration is not adequate. Total energy band calculations will have to be used to predict these quantities.

Appendix C References

1. D. L. Laing and L. D. Pettit, *J. Chem. Soc., Dalton Trans.*, 2297 (1975).
2. The exchange energy κ_X defined here is half the value of the standard exchange integral κ. This is to eliminate a plethora of 1/2 factors. The atomic spectra data were obtained from C. E. Moore. *Atomic Energy Levels.* NSRDS-NBS 35, 1971.
3. Cohesive energies were calculated using heats of formation data obtained from D. R. Stull and H. Prophet, *Natl. stand. Ref. Data Ser.* (U. S., Natl., Bur. Stand., NSRDS-NBS, **37**, 1971.

Part II

First Principles Studies of Cubic GaN Epitaxial Growth

Chapter IV

Surface Reconstructions and Energetics Relevant for MBE Growth of Cubic GaN

Abstract

Using quantum chemical cluster model approach, we have investigated issues relevant for molecular beam epitaxial (MBE) growth of cubic GaN using atomic N and molecular N_2 sources on the (001) surface orientation. We consider the interactions of gas-phase atomic and molecular nitrogens with the N terminated surface and conclude that ground state atomic N (^4S) is favorable for growth but excited states (^2D and ^2P) of atomic N are likely to etch off chemisorbed surface N atoms to form desorbed N_2. These results also indicate that ground state N_2 ($^1\Sigma_g^+$) is energetically unfavorable for growth of GaN by 1.42 eV, but that the excited state active nitrogen N_2 ($^3\Sigma_u^+$) would likely undergo dissociative chemisorption (adding one N to the surface), leading to favorable growth (exothermic by 0.92 eV). These results also suggest that growth is preferred under Ga-rich conditions.

IV.1 Introduction

GaN is a direct wide bandgap semiconductor which is of great current technological interest for developing blue light emitting diodes (LED) and potential blue laser applications.[1] Consequently there have been numerous efforts to grow GaN material. However, the present crystal growth techniques are still not well-developed to grow device-quality materials. Currently for large-scale production chemical vapor deposition (CVD) is the technique of choice. The drawback of CVD is that the material grown often is not in the single crystal form. Also the organic compounds ($Ga(CH_3)_3 + NH_3$) that are employed in CVD for growth contain H, which would lead to p-type compensation of the material.[1] Molecular beam epitaxy (MBE) technique on the other hand offers H-free growth environment and single crystal growth, which is the preferred method for growing high-quality thin films. Nevertheless, MBE growth of GaN has been plagued with problems such as poor surface morphology and high background electron concentration,[2,3] which are mostly N source related. MBE experiments with molecular N_2 source indicate that to achieve growth of GaN, it is necessary to plasma convert the N_2 to N_2^+ and to accelerate the ion to a large impact energy[4] ($\geq$ 35 eV) so as to overcome the large barrier arising from the strong nitrogen-nitrogen bond (bond energy of 9.76 eV). Such large impact energies will likely cause surface damage, limiting the ultimate quality of the film. The frequently occurred N vacancies in the thin film grown also bring about the background electron concentration problem which interferes with the controlled p-type doping. Even though the actual N species favorable for growth is not known (N ion sources are known to cause surface roughening), it appears that MBE growth using atomic N or excited state N_2 sources would be attractive since it should not require high impact energies. The development of viable N sources is currently underway using an arcjet design[5].

The stable form of GaN has the hexagonal wurtzite structure, h-GaN. How-

ever, under certain growth conditions[6] it is also possible to grow thin films of the thermodynamically metastable cubic form (sphalerite), c-GaN, which has several advantages over the more commonly occurred h-GaN. Theoretically it is believed that c-GaN has higher carrier mobility than for h-GaN due to the higher symmetry and thus lower electron-phonon scattering in the cubic phase. It therefore possess superior electronic properties for some device applications.[7] c-GaN is also easier for dopant incorporation than h-GaN,[8] and has cleavage surfaces more suitable for laser fabrication. One more reason for the interest in growing c-GaN is the better lattice mismatch on available substrates. [With the 3C-SiC substrate, the lattice mismatch for growing c-GaN is 3.2%, somewhat smaller than that for growing h-GaN on 6H-SiC (3.5%).]

It has been shown that using excited molecular nitrogen or atomic nitrogen source can result in high-quality GaN film growth.[9] Excited N_2 in the $^3\Sigma_u^+$ metastable state has a lifetime of $2 \times 10^6 \mu s$,[10] which can survive long enough for growth to occur. As for the atomic nitrogen atom, the mean free path is greater than 1000 cm[11] under a typical MBE system pressure of 4×10^{-5} Torr. Under this condition the collision process of covering them back to N_2 is negligible. In this chapter we use surface cluster models and first principle calculations to examine the surface structures and energetics of c-GaN (001). The growth process and energetics using the various ground and excited states of N and N_2 are then investigated. To outline this chapter in the following: Section 2 provides details of the calculations. Section 3 discusses the surface reconstructions. Section 4 reviews the energetics of gas phase N and N_2 sources. Section 5 reports the energetics relevant for growth. The conclusion is in Section 6.

VI.2 Computational Method

Finite cluster models (described in VI.3) were used to simulate GaN (001) surfaces. In geometry optimization calculations we used the 3-electron effective core

potential from Hay and Wadt[12] coupled with their $(3s3p/3s2p)$ contracted Gaussian basis set for Ga. For N we used the 6-31G* basis set (including core electrons). Dunning/Huzinaga's (4s/2s) basis set was used for H. All geometries were optimized at the HF level. Some of the geometry optimizations were also performed at the B3LYP/DFT (described in Appendix A) and LDA/DFT[13] levels. It has been found that the shallow $3d$-core electrons of Ga overlap considerably with the valence charge density, leading to a significant effect on energetic properties.[14] The omission of this core-valence correlation may introduce errors in energy. Therefore for energetics calculations the all-electron basis sets[15] (denoted as MSV*) for Ga and N were used (while H basis set was kept the same). MSV* basis sets are tabulated in Table V.1. These basis sets involve contracted basis functions for the core orbitals plus two sets of valence basis functions for each valence orbital plus one set of d polarization functions. All energy calculations were carried out at the B3LYP/DFT level.

IV.3 Surface Reconstruction

IV.3.1 *Ga* Terminated (001) Surface

It has been observed from RHEED experiments that $GaN(001)$ surface often forms the $c(2 \times 2)$ reconstruction under Ga-rich conditions.[16,17] Ploog *et al.*[16] proposed a full Ga monolayer ($\Theta_{Ga} = 1$) surface structure model (shown in Figure IV.1a) to account for this $c(2\times2)$ reconstruction, where there is one alternate dimer bond between every pair of surface Ga atoms. We think this surface model is problematic because in this model each surface Ga uses $2 \times \frac{3}{4} = \frac{3}{2}$ electrons (for each $Ga-N$ bond electron pair in GaN, Ga only contributes $\frac{3}{4}$ electrons while N contributes $\frac{5}{4}$ electrons) to make two bonds with the second layer N and one electron to make the dimer bond. This results in every Ga on the surface having $3 - \frac{3}{2} - 1 = \frac{1}{2}$ electrons left in the dangling orbital, which is highly unstable and does not follow the electron counting rule. To explain the observed $c(2 \times 2)$ reconstruction we have

Table IV.1. MSV* Basis Sets for *Ga* and *N*

	Ga (43321/4321/311)		N (421/311)	
	exponent	coefficient	exponent	coefficient
s	12280.00000	.0200799	587.50000	.0208091
	1852.00000	.1392998	88.61000	.1423225
	418.20000	.4830319	19.79000	.4795299
	114.00000	.4958735	5.26300	.5002286
	163.50000	-.1269048	7.14700	-.1964301
	27.57000	.4458493	.76720	1.0740028
	10.76000	.6452182	.23170	1.0000000
	16.95000	-.2418781		
	3.30400	.5173021		
	1.23100	.6288712		
	1.77500	-.4157210		
	.18980	1.1176758		
	.06699	1.0000000		
p	559.40000	.0297783	13.56000	.0589272
	130.80000	.1909530	2.92400	.3203068
	40.29000	.5210790	.79940	.7531123
	13.75000	.4303017	.21920	1.0000000
	9.40500	.0655480		
	4.35300	.5212200		
	1.40600	.5202436		
	3.64800	-.0079170		
	.255000	1.0013291		
	.06785	1.0000000		
d	40.47000	.0852251	0.79940	1.0000000
	10.99000	.3874325		
	3.41900	.6989743		
	.97750	1.0000000		
	.28600	1.0000000		

(a) Θ = 1

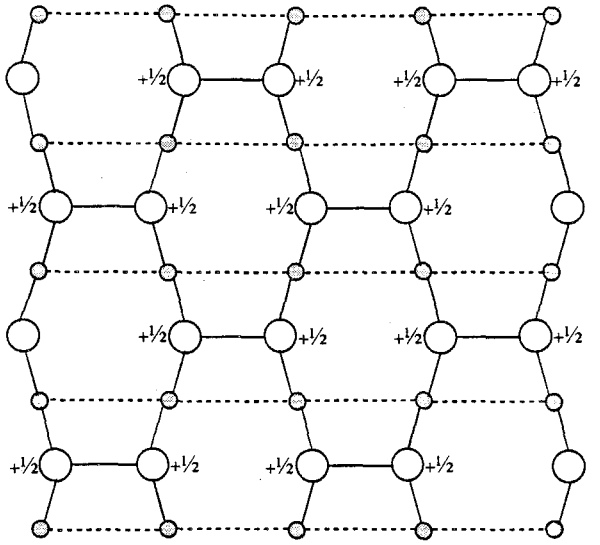

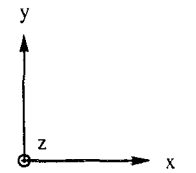

(b) Θ = 1 ½

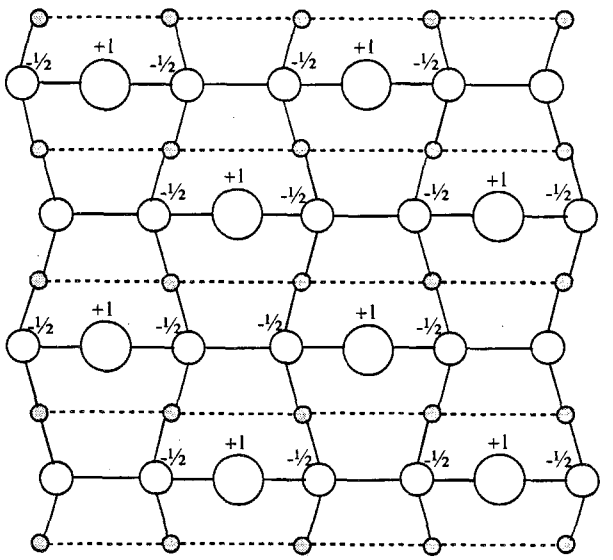

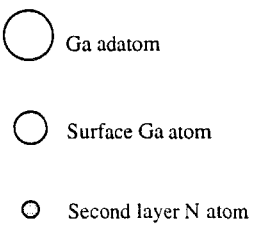

Figure IV.1. (a) Ploog's Ga-rich $c(2\times2)$ surface model. (b) Our Ga-rich $c(2\times2)$ surface model.

proposed a one-and-half monolayer ($\Theta_{Ga} = \frac{3}{2}$) model (shown in Figure IV.1b), where there are alternate Ga dimers and Ga adatoms along both the $2\times$ and $\times 2$ directions. Compared to Ploog's model, each surface Ga now has to use one electron to make an additional $Ga-Ga$ bond to the adatom, resulting in $1-\frac{1}{2}=\frac{1}{2}$ electrons deficiency in the surface Ga. Since on this surface for every two surface Ga atoms there is one Ga adatom, and each adatom Ga only uses two electrons to makes two $Ga-Ga$ bonds and therefore has one electron left. This excess electron can then be transferred to the two underlying Ga atoms, making up for the $2\times\frac{1}{2}=1$ electron deficiency. The final surface electronic structure will thus only have Ga adatom dangling orbitals which are empty, satisfying the electron counting rule.

We used a $Ga_{12}N_8H_{26}$ cluster (Figure IV.2) to model the proposed $c(2\times 2)$ surface. Proper electron counting was taken into consideration in constructing this cluster so that each Ga adatom in the cluster has empty dangling orbitals just like for the real surface. In this cluster, we denote the two Ga adatoms as Ga_1, the two surface dimer Ga atoms as Ga_2, and the second layer N that Ga_2 bonds to as N_3. Geometry optimization was performed at the HF level with C_s symmetry. Only the top two layers of atoms were allowed to move during relaxation. The optimization results are shown in Figure IV.2. The dimer bond length $R_{Ga_2Ga_2}=2.369$ Å, which is very close to the $Ga-Ga$ bond length (2.340 Å) in the molecule $H_2Ga-GaH_2$ calculated at the same level, indicating that the dimer bond has a bond order (BO) equal to 1. $R_{Ga_1Ga_2}=2.494$ Å which is longer than the dimer bond. This may be because of the electron transfer. We expect $R_{Ga_2N_3}$ to be larger than the bulk value (1.949 Å) due to the deviation of Ga_1 from its bulk position to form the dimer bond. $R_{Ga_2N_3}$ is calculated to be =2.000 Å. The bond angle of Ga_1 with the two underlying Ga is calculated to be 108.0°, which is less than the 120.0° we expected it to be. This is probably due to the smaller spacing between two Ga lattice points in GaN as compared to the spacing in the corresponding all-Ga zinc-blend structure.

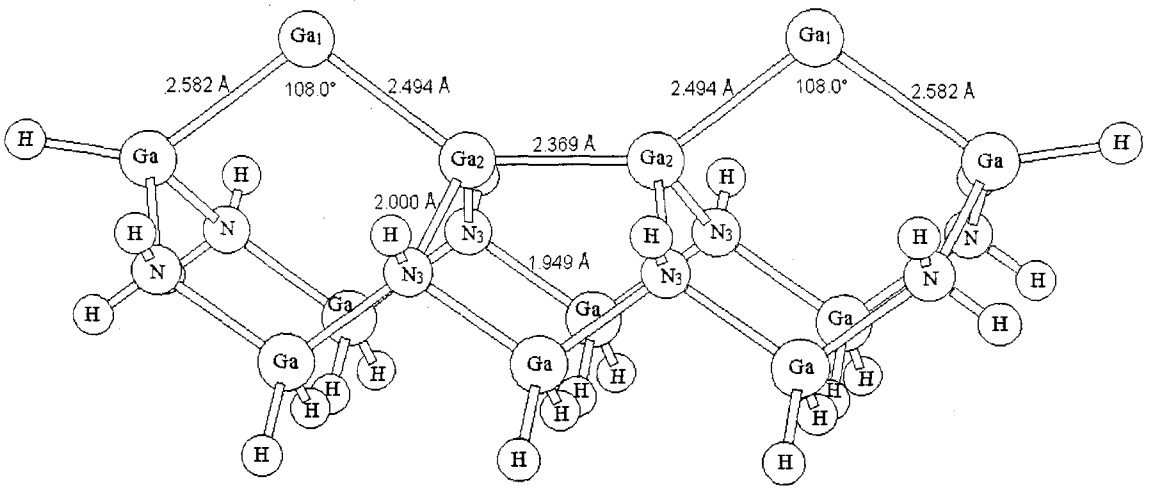

Figure IV.2. Optimized geometry of the $Ga_{12}N_8H_{28}$ cluster for the Ga-rich $c(2\times2)$ surface.

For the Ga_1 to form an bond angle of 120.0° (assuming $R_{Ga_1Ga_2}$ does not change), it would require a Ga_2 displacement of 0.568 Å (instead of 0.407 Å), resulting in $R_{Ga_2Ga_2}$ = 2.046 Å, which is too short for a Ga–Ga bond and thus unlikely to happen.

IV.3.2 N Terminated (001) Surface

There has not been any structural information regarding the N terminated $GaN(001)$ surface available so far. In the analogous case of $GaAs(001)$, the most frequently observed As terminated surface has the (2×4) reconstruction with $\Theta_{As} = \frac{3}{4}$ coverage, with one missing As dimer for every four As dimers (the so-called missing dimer model).[18] However we believe that this reconstruction is not likely for GaN because of the N–N dimer bond on the surface will very likely lead to the desorption of N_2. In fact, as illustrated in Figure IV.3, we believe that the surface N coverage Θ_N (in the absence of other Ga adatoms) should not exceed $\frac{1}{2}$, otherwise this would unavoidably force N atoms to be located on adjacent sites, eventually resulting in N_2 desorption due to the large $N{\equiv}N$ bond energy. The electronic structure of $\Theta_N = \frac{1}{2}$ surface has each surface N with two doubly occupied dangling orbitals, which according to the electron counting rule should be a stable surface. The two possible reconstructions for the $\Theta_N = \frac{1}{2}$ surface are $c(2 \times 2)$ and $p(2 \times 1)$. The $p(2 \times 1)$ surface is higher in energy than the $c(2 \times 2)$ surface by 0.65 eV from the result of band calculations,[11] which may mainly be due to repulsion between the adjacent N lone pairs.

The cluster models used for the $\Theta_N = \frac{1}{2}$ (001) surfaces are illustrated in Figure IV.4. We used a $N_8Ga_8H_{20}$ cluster (denoted as $C1$) to model the $c(2 \times 2)$ surface. $C1$ has one surface atom N (denoted as N_1), two second layer Ga atoms (denoted as Ga_2), four third layer N atoms (denoted as N_3), six fourth layer Ga atoms, three fifth layer N atoms, plus 20 hydrogen atoms to saturate the dangling orbitals within the cluster. Again, proper electron counting was considered in

(a) $\Theta = 1/2$

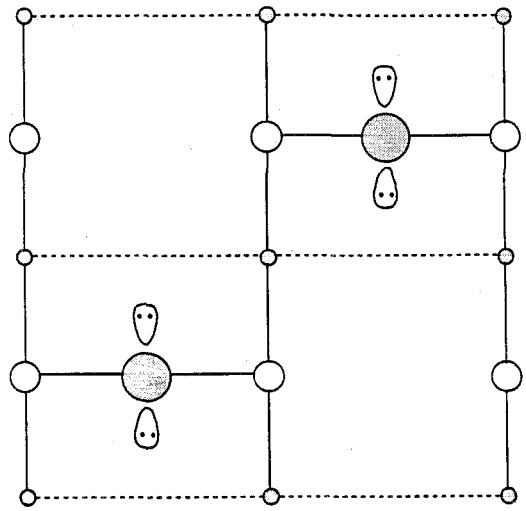

(b) $\Theta > 1/2$

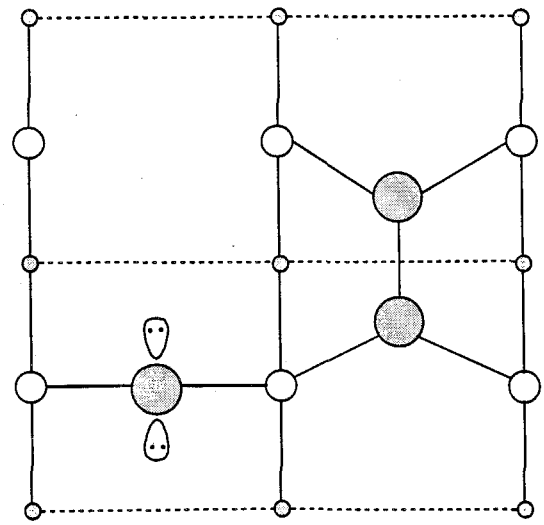

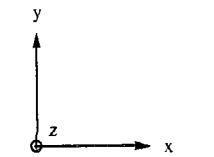

Surface N atom

Second Ga atom

Third layer N atom

N_2 desorption

Figure IV.3. N terminated GaN(001) surface (a) $\Theta_N = 1/2$. (b) $\Theta_N > 1/2$.

(a)

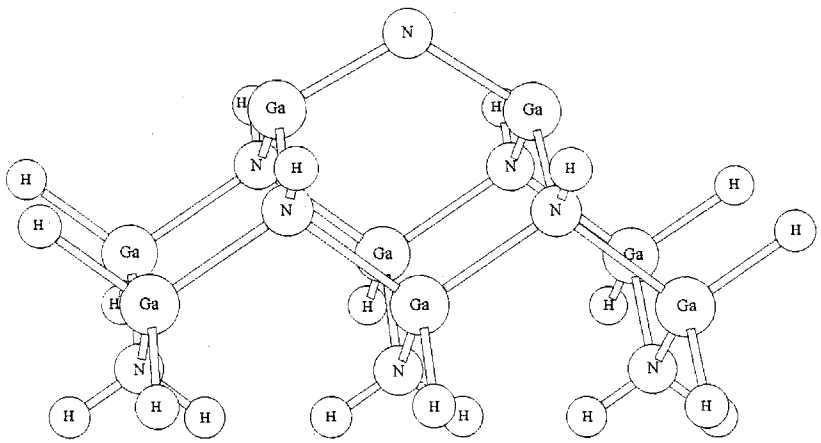

(b)

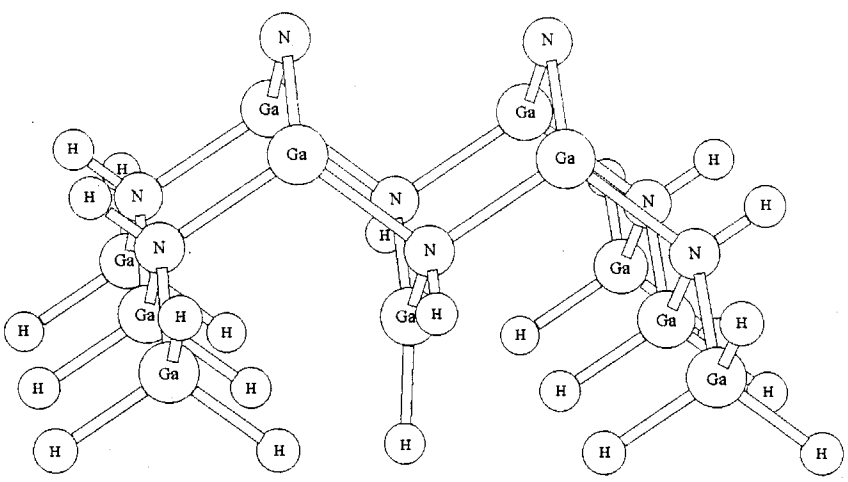

Figure IV.4. (a) $N_8Ga_8H_{20}$ cluster *C*1 for the $c(2\times2)_N$ surface.(b) $N_8Ga_{11}H_{23}$ cluster *C*2 for the $p(2\times1)_N$ surface.

constructing this cluster so as to mimic the electronic structure of the infinite GaN $(100)_N$ surface having one-half monolayer coverage of N. On this surface each N atom has two electron lone pairs, which can be regarded as having a N^- configuration. Another $N_8Ga_{11}H_{23}$ cluster (denoted as $C2$) was designed to model the $p(2\times 1)$ surface. In this cluster the two surface N atoms both have the N^- configuration and are adjacent to each other. $C2$ has two surface atom N (denoted as N_1), four second layer Ga atoms (denoted as Ga_2), six third layer N atoms (denoted as N_3), and seven fourth layer Ga atoms plus 23 hydrogen atoms for saturate dangling orbitals. Geometry optimizations were carried out at the HF, B3LYP/DFT, and LDA/DFT levels with C_{2v} summitry. Only the top three layers of atoms were allowed to relax. These results are summarized in Table IV.2.

Our $c(2\times 2)$ relaxation calculation using cluster $C1$ indicate that the N_1 atom on the top layer forms strong covalent bonds (BO = 1) to the two subsurface Ga_2 while an electron is transferred to the N_1 from the bulk of the cluster. The calculated surface N_1 to subsurface Ga_2 bond distance $R_{N_1Ga_2}$ = 1.754 Å (HF) or 1.778 Å (B3LYP/DFT) or 1.780 Å (LDA/DFT), which is significantly contracted from the bulk GaN value of 1.949Å. Such a contraction is expected since the average bulk $Ga-N$ bond has BO = $\frac{3}{4}$ while the surface bond order BO = 1. The back-bond (second layer Ga to third-layer N) distance is calculated to be $R_{Ga_2N_3}$ = 1.981Å (HF) or 1.991Å (B3lYP/DFT), or 1.982Å (LDA/DFT), which is larger than the bulk value (as in the case of $HgTe$). This is probably because of the charge transfer from the Ga_2 to the surface N_1.

Similar to the molecular calculations in Chapter II and the cluster calculations in Appendix B, the bond distance results from B3LYP/DFT are always larger than those obtained form HF calculations. LDA/DFT bond distances were calculated here for the purpose of being able to compare with future band calculations which normally are done at this level. This comparison enables us to study the

Table IV.2. Atomic Relaxations in the $\Theta = \frac{1}{2}$ $GaN(001)_N$ Surfaces

	HF	B3LYP	LDA
	(1) $c(2 \times 2)^a$		
$R_{N_1Ga_2}$	1.754Å	1.778Å	1.780Å
$\Delta R_{N_1Ga_2}{}^b$	-0.195Å	-0.171Å	-0.169Å
$R_{Ga_2N_3}$	1.981Å	1.991Å	1.982Å
$\Delta R_{Ga_2N_3}{}^b$	0.032Å	0.042Å	0.033Å
$\theta_{Ga_2N_1Ga_2}$	99.7°	97.5°	96.6°
	(2) $p(2 \times 1)^a$		
$R_{N_1Ga_2}$	1.741Å	1.767Å	1.768Å
$\Delta R_{N_1Ga_2}{}^b$	-0.206Å	-0.182Å	-0.181Å
$R_{Ga_2N_3}$	1.950Å	1.959Å	1.959Å
$\Delta R_{Ga_2N_3}{}^b$	0.001Å	0.010Å	0.010Å
$\theta_{Ga_2N_1Ga_2}$	98.9°	96.9°	96.9°

[a] Cluster C1 and C2 were used for c(2×2) and p(2×1), respectively.
[b] Difference between calculated bond length and the bulk value.

cluster *vs.* periodic modeling approach on GaN, where these two approaches can be complimentary to each other. The calculated surface N bond angle $\theta_{Ga_2N_1Ga_2}$ is 99.7° (HF level) or 97.5 (B3LYP/DFT) or 96.6 (LDA/DFT), decreasing from the bulk tetrahedral angle. This result is consistent with the fact that N makes two BO = 1 bonds (with mostly, say, N_{2px} and N_{2yx} orbitals) and has the N^- electronic structure.

The $p(2 \times 1)$ optimization result using cluster $C2$ shows a similar trend in bond distances and angles as in the case of $c(2 \times 2)$. The slight differences in the values of bond distance and angle may be due to the interaction between the two adjacent surface N atoms, which is absent in the $c(2 \times 2)$ surface. Based on our

previous experience, we believe that B3LYP/DFT generally overestimates bond distances. But for energy calculations, as discussed in Appendix A and demonstrated in Chapter II, B3LYP is a much superior method than HF, and is able to give good energy results. Therefore for the GaN growth energetics calculations (discussed in Section 5), B3LYP method coupled with the HF geometries obtained from the current calculation were used.

IV.4 Energetics of the Nitrogen Source

Figure V.5 summarizes the energetics of various potential sources of nitrogen (both atomic and molecular)[19] for growth in GaN. Relevant features of these species to note are

1. Ground state N_2 has a very large bond energy calculated to be 9.65 eV using B3LYP/MSV*, which is very close to the experimental value of 9.76 eV.
2. The lowest excited state of $N_2(^3\Sigma_u^+)$, sometimes called active nitrogen, has a bond energy of only 3.54 eV.
3. N atoms may be in the ground state (^4S) or excited state (^2D and ^2P) at 2.38 eV and 3.58 eV, respectively.

Our objective here is to consider the GaN growth using these possible nitrogen sources in light of the stable surface structures.

IV.5 Energy Phase Diagram for the GaN Growth

To construct an energy phase diagram for growth on $GaN(001)$ surface using various N sources, we first used cluster $C1$ to calculate the energy needed to remove the surface N in the $c(2 \times 2)$ unit cell. We used the HF-optimized geometries of the surface clusters for both "before" and "after" the N desorption to calculate the energy using MSV* basis at the B3LYP level. This energy was calculated to be 3.87 eV. Even though the energy needed to remove another N in the same $c(2 \times 2)$ unit cell may not be too different from 3.87 eV since the bonding configuration of

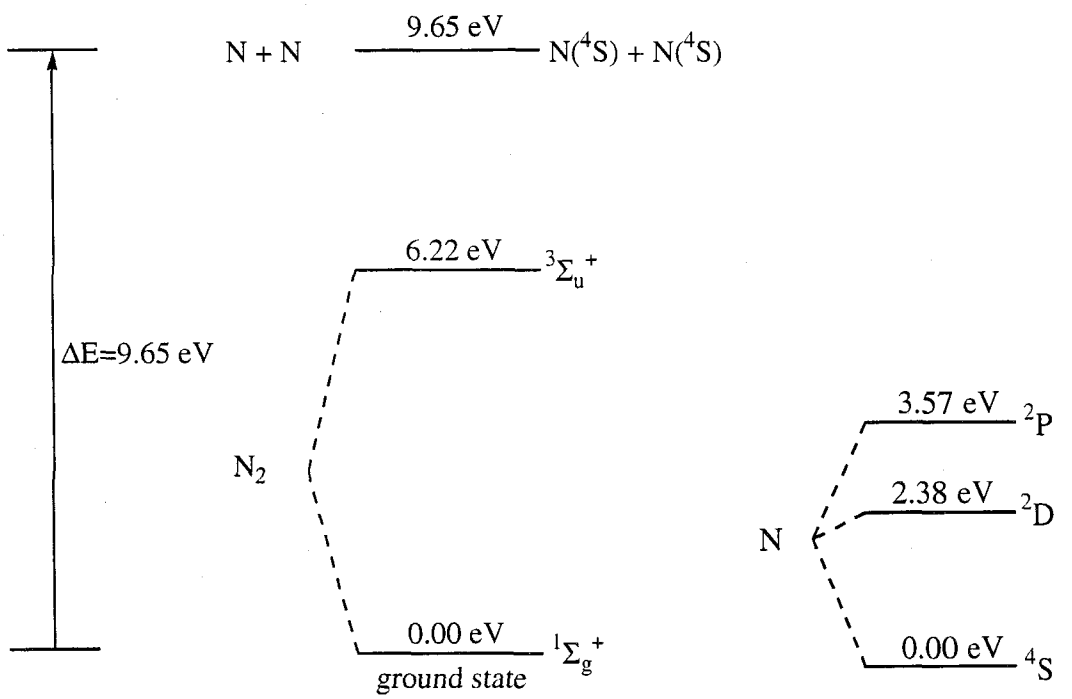

Figure IV.5. Basic energetics of various N sources.

N is the same, the absence of the first N might somewhat affect the energetics of the second N in the same unit cell, making it easier to desorb. To make sure that all the possible effects are taken into consideration, we opted to use cluster $C2$ to calculate the total energy needed to remove the two surface N atom in one unit cell. Using the same approach as in the $C1$ case, the energy was calculated to be 7.58 eV, which is indeed 0.16 eV smaller than the 3.87×2 eV needed if we were to remove two surface N atoms from two separate $C1$ clusters. From the growth point of view, since the bond energy of ground state N_2 is 9.65 eV, this amounts to energy uphill of $9.65 - 7.58 = 2.07$ eV if growing from ground state N_2 to form the $p(2 \times 1)$ surface. Since the $p(2 \times 1)$ is unstable with respect to the $c(2 \times 2)$ by 0.65 eV, the actual growth is endothermic by $2.07 - 0.65 = 1.42$ eV. Using these cluster calculation results coupled with the energetics of the nitrogen sources, we have constructed an MBE growth energy phase diagram elucidating the relevant growth energetics and is shown in Figure IV.6.

Unlike the ground state N_2, a ground state atomic N source atom binds to the surface by 3.87 eV. Thus its growth energetics are quite favorable. Of course such a process would involve conversion of the large chemical energy into phonons (heat). Thus an issue in growth is whether the incoming N ends up chemisorbed on the surface or it reacts with a N already on the surface to desorb as N_2 (etching the N off the growth surface). Since the ground state for a surface N atom will usually have all electrons spin paired up with only occasional singly-occupied dangling bond orbitals while the new N (^4S) has three unpaired spins, the initial complex formed with the surface would be a triplet state. Thus the one-step process for $N(^4S)$ to etch off a surface bonded N to form ground state N_2 ($^1\Sigma_g^+$) is expected to be forbidden (illustrated in Figure IV.7). Instead the initial state formed will create phonons as it binds more strongly leading to growth. Simultaneous spin exchange could eventually lead to the desorption of ground state N_2. However, it is plausible

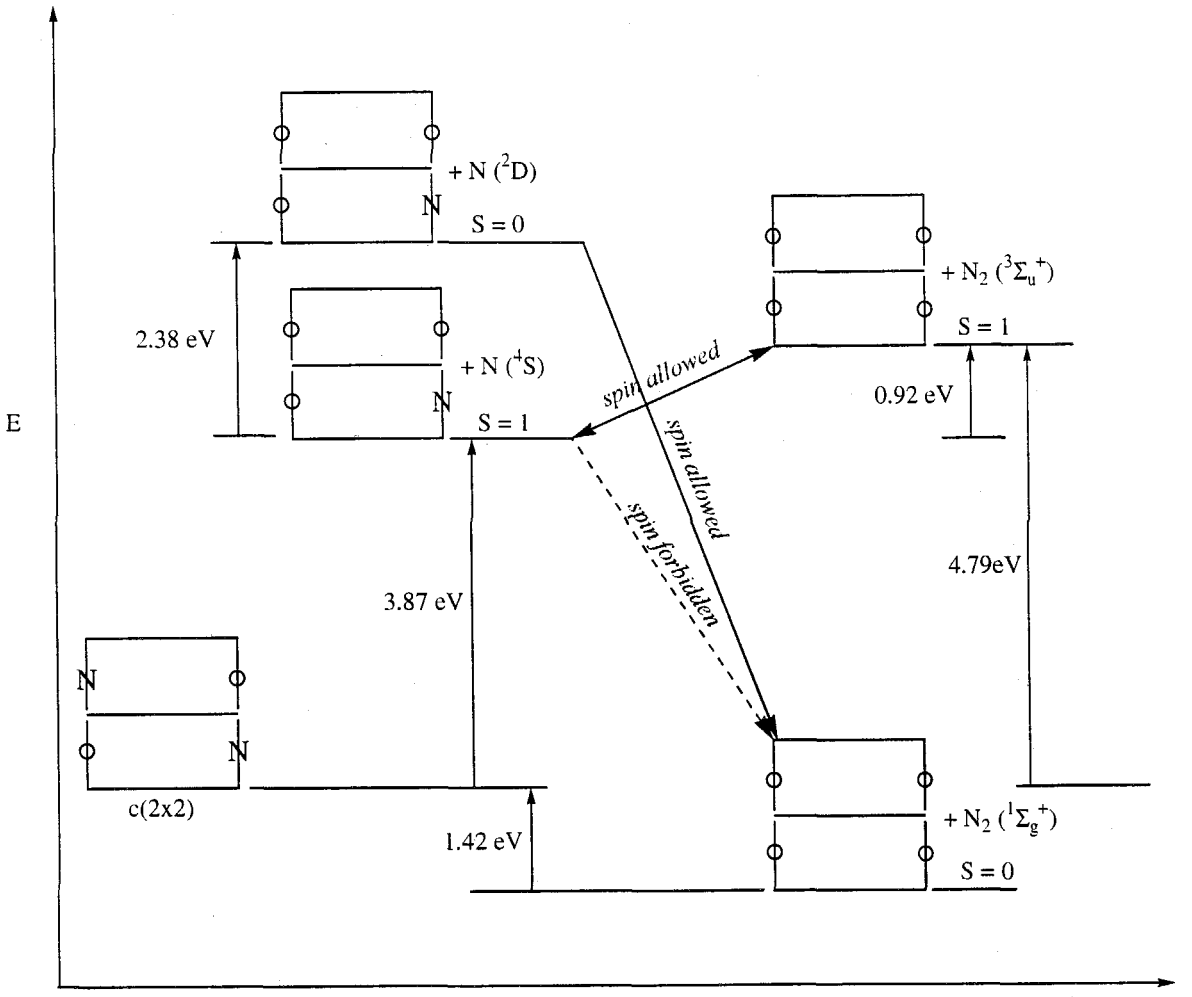

Figure IV.6. MBE growth energetics on GaN(001) surface using various N sources.

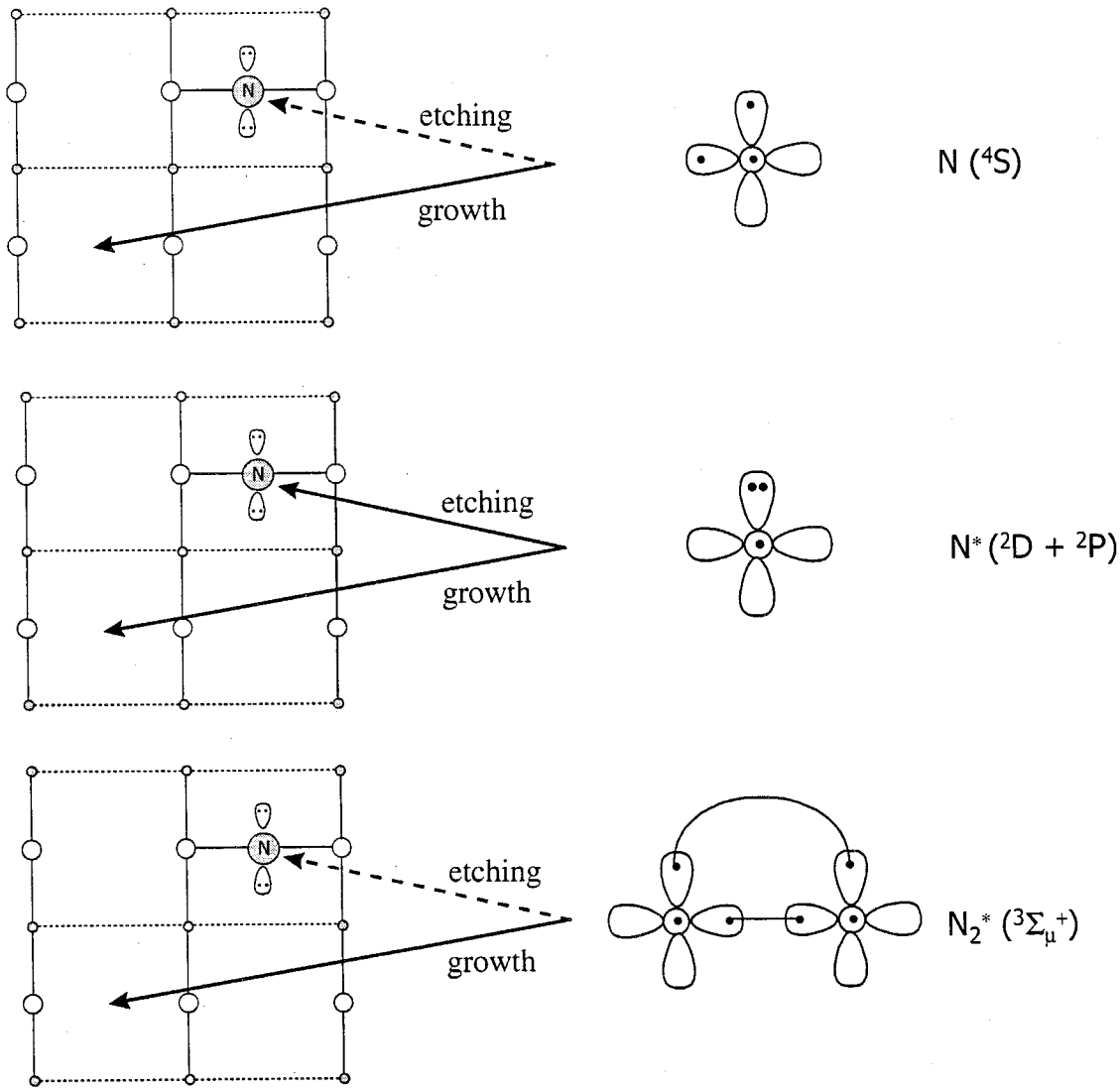

Figure IV.7. Illustration of the possible reaction pathways for the various N sources reacting with $GaN(001)_N$ surface.

that despite the 3.87 eV exothermicity most atoms may lead to growth. A second channel for the reaction is to desorb N_2 in the $(^3\Sigma_u^+)$ excited state; this is spin allowed, but is energetically unfavorable by 0.92 eV.

Since the procedure by which an atomic N beam is generated may at the same time lead to atomic excited states ^2D and ^2P (e.g., arcjet-generated N sources), we have also considered surface reactions likely to occur during growth by using these excited states of N. Since their growth energetics should be even more favorable than for the ground state N, we thus looked at reaction pathways where the incoming atom might lead to an etching process (dissociative recombination) rather than growth (chemisorption). The salient difference between ground state and excited state N is that the doublet states allow for a GVB description in which one of the N_{2p} orbitals is doubly occupied while another is empty, whereas $N(^4S)$ has one electron in each orbital. Therefore reactions are expected to be quite different for the excited states $N(^2D)$ or $N(^2P)$. In particular, the empty orbital of the doublet N atom can overlap with a doubly occupied lone pair orbital of the surface N^- to form a bond that might lead directly to dissociative recombination to form ground state N_2 (see Figure IV.7). Since this process is very exothermic (by 7.67 eV for $N(^2D)$), we expect a very high reaction probability. From this reasoning we think such etching processes are much more likely when the N atom is in the excited state than in the ground state $N(^4S)$. This analysis suggests that if one is to grow high quality GaN from atomic N source, it will be necessary to exclude the excited (doublet) states from the N beam.

Some other growth strategies are also suggested by Figure IV.6. With appropriate plasma or arcjet conditions, it is possible to obtain a significant population of the lowest triplet state, active nitrogen $N_2(^3\Sigma_u^+)$. Unlike the ground state N_2, the bond energy for $N_2(^3\Sigma_u^+)$ is only 3.54 eV, making the dissociative chemisorption energetically favorable (it was calculated to be exothermic by 0.92 eV). The

dissociative chemisorption leads to one N bonding to the surface while the other N atom leaves the surface in the ^4S state. Through such an process the leaving N can conserve kinetic energy and momentum of the incoming species without creating phonons which may cause dissociative recombination. Consequently we expect that growth from $N_2(^3\Sigma_u^+)$ might lead to high quality films.

Since the desorption of N_2 is favorable when N atoms are on adjacent sites, the (001) surface is expected to be stable only for up to one-half coverage of N. This raises the question of how growth is able to be sustained. To add additional N to the growth surface seems to be possible only under the condition that extra Ga atoms are present when the N arrives to simultaneously form at least a third $Ga-N$ bond to each N in order to trap the N on the surface and prevent rapid desorption of N_2.

The above analysis suggests that Ga-rich conditions with enhanced Ga mobility are preferred for growth. Such growth conditions will both increase $Ga-N$ formation and at the same time avoiding formation of $N-N$ dimers that would lead to desorption of N_2. Indirect experimental support of this conclusion comes from the studies of Newman *et al.*[20] who found that the quality of the GaN film improves with the increase of Ga flux up to the point that Ga droplets are starting to formed.

IV.6 Conclusion

Using quantum chemical cluster approach we have studied the surface reconstructions of Ga and N terminated $GaN(001)$ surfaces. A $c(2\times2)$ surface structural model with $\Theta_{Ga} = \frac{3}{2}$ that conforms to both electron counting rule and experiment is proposed for the Ga terminated (001) surface. We have also calculated the energetics for the $GaN(100)_N$ surface interacting with various atomic and molecular nitrogen sources. Using these results we have constructed an energy phase diagram for the growth of GaN using these nitrogen sources. These calculations suggest

that excited state molecular N_2 ($^3\Sigma_u^+$) is the most favorable of all N species for growth of high quality GaN because it can undergo a dissociative chemisorption process. Ground state atomic N (^4S) is also good for growth without etching off surface N significantly. The doublet excited states N (^2D and ^2P) might lead to a high probability of surface N abstraction, leading to N vacancies. Therefore if an experimental design is to produce active N sources for growth from the ground state N_2, one should maximize the output of active nitrogen $N_2(^3\Sigma_u^+)$ while avoiding the doublet atomic N.

Chapter IV References

1. H. Morkoc, S. Strite, G. B. Gao, M. E. Lin, B. Sverdlov, and M. Burns, *J. Appl. Phys.* **76**, 1363 (1994).
2. K. G. Fertitta, A. L. Holmes, J. G. Neff, F. J. Ciuba, and R. D. Dupuis, *Appl. Phys. Lett.* **65**, 1823 (1994).
3. H. Liu, A. C. Frankel, J. G. Kim, and R. M. Park, *J. Appl. Phys.* **74**, 6124 (1993).
4. R. C. Powell, N.-E. Lee, Y. -W. Kim, and J. E. Greene, *J. Appl. Phys.* **73**, 189 (1993).
5. F. Grunthaner and P. Grunthaner, JPL, private communication.
6. S. Strite and H. Morkoc, *J. Vac. Sci. Technol.* **B 10**, 1237 (1992).
7. K. Das and D. K. Ferry, *Solid-State Electron* **19**, 851 (1976).
8. T. Lei, T. D. Moustakas, R. J. Graham, Y. He, and S. J. Berkowitz, *J. Appl. Phys.* **71**, 1 (1992).
9. W. C. Hughes, W. H. Rowland, Jr., M. A. L. Johnson, S. Fujita, J. W. Cook, Jr., J. F. Schetzina, J. Ren, and J. A. Edmond, *J. Vac. Sci. Technol.* **B 13**, 1571 (1995).
10. K. Ohkawa, T. Karasawa, and T. Mitsuyu, *J. Cryst. Growth* **117**, 375 (1992).
11. Band calculations from X. J. Chen and W. A. Goddard III, unpublished work.
12. W. R. Wadt and P. J. Hay, *J. Chem. Phys.* **82**, 284 (1985).
13. (a) D. M. Ceperley and B. I. Alder, *Phys. Rev. Lett.* **45**, 566 (1980); (b) J. P. Perdew and A. Zunger, *Phys. Rev.* **B23**, 5048 (1981).
14. A. García and M. L. Cohen, *Phys. Rev.* **B47**, 6751 (1993).
15. A. K. Rappé and W. A. Goddard III, unpublished.
16. O. Brandt, H. Yang, B. Jenichen, Y. Suzuki, L. Daweritz, and K. H. Ploog,

Phys. Rev. **B52**, R2253 (1995).

17. D. Schikora, M. Hankeln, D. J. As, and K. Lischka. *Phys. Rev.* **B54**, R8381 (1996).
18. M. D. Pashley, K. W. Haberern, W. Friday, J. M. Woodall, and P. D. Kirchner, *Phys. Rev. Lett.* **60**, 2176 (1988).
19. (a) For atomic N, R. F. Bacher and S. Goudsmit. *Atomic Energy States* 1st Ed., McGraw-Hill, New York and London 1932; (b) For N_2, K. P. Huber and G. Herzberg, *Molecular Spectra and Molecular Structure* **IV**, 1979.
20. N. Newman, J. Ross, and M. Rubin *Appl. Phys. Lett.* **62**, 1242 (1993).

Part III

Ab Initio Study of Corrosion Inhibition on Iron Oxide

Chapter V

Ab Initio Calculations of Oleic Imidazolines Bound to Ferric Clusters

Abstract

The oleic imidazoline (OI) class of molecules are used extensively for corrosion inhibitor in oil field pipeline applications. However, up until now there has not been any model for understanding how these inhibitors work. As a first step in elucidating this complex mechanism, we have carried out quantum mechanical calculations on clusters involving Fe^{3+}, H_2O, OH, and OI. These calculations are used to determine how OI bonds to the surface and the strength of the surface bond. These results can then be applied to the development of force field for molecular dynamics simulations.

V.1 Introduction

Corrosion is a phenomenon associated with most metals and is particularly severe in the case of iron. Corrosion problems in steel pipes used for the production and transportation of oil and gas cause enormous industrial waste and expense and thus require the use of corrosion inhibitors. Development of such corrosion inhibitors has been slow because the mechanism by which these inhibitors (usually N-containing organic compounds) prevent corrosion is not understood.[1] Experimental evidence in support of specific mechanisms is not available because these inhibitors are normally used in low concentrations (a few parts per million) and the operating environments are quite complex. Therefore it is very difficult to experimentally observe the atomistic nature of the fluid/metal interface.

Some of the most effective corrosion inhibitors for oil field pipeline applications are the oleic imidazoline (OI) class of molecules. However, the bonding information of OI with the pipe surface still remains unknown. Since under normal operating conditions the pipe surface is covered with iron oxides, in order to understand why type of surface interaction is involved in corrosion inhibition, we have used iron oxide clusters to model the oxide surface and carried out quantum mechanical calculations of iron oxide clusters interacting with oleic imidazoline and various N-containing molecules. Section 2 describes the computational details. Section 3 describes the general valence bond (GVB) cluster model of Fe_2O_3. Section 4 discusses the electronic characteristics of OI molecules and how they bond to the iron oxide surface. In Section 5 we discuss the theoretical binding energy results of various N-containing molecules (including OI) and the iron oxide cluster.

V.2 Computational Method

Ab initio Hartree-Fock calculations were used throughout this study. To avoid errors caused by basis set and pseudopotential effects, three different basis/ECP schemes were used in the calculations:

(i) LANL1DZ - Hay and Wadt's (3s2p5d/2s2p2d) basis and 18-electron effective core potential for Fe,[2] D95V (DZ)[3] basis for the non-metals.

(ii) LAV3P* - Hay and Wadt's (3s2p5d/3s2p2d) basis and 18-electron effective core potential for Fe, 6-31G* basis for the non-metals.

(iii) LACVP* - Hay and Wadt's (9s5p5d/3s3p2d) basis and 10-electron effective core potential for Fe,[2] 6-31G* basis for the non-metals.

All calculations with LANL1DZ and LACVP* were done at UHF level using Gaussian 92 program, while with LAV3P* the calculations were done at RHF level using PSGVB program.[4]

V.3 Iron Oxide (Fe_2O_3)

V.3.1 The GVB Cluster Model of Fe_2O_3

Ferric oxide commonly exists as nonmagnetic $\alpha-Fe_2O_3$ (hematite) or as magnetic $\gamma-Fe_2O_3$ (maghemite). At pH in the range of $4 \sim 6$ (for oil field applications the pH ~ 4.5) the stable oxide form of iron is hematite.[5,6] Thus we expect that the oil pipe surface will be covered by this native oxide. Consequently we studied the interactions of OI molecules with the $\alpha-Fe_2O_3$ surface. In $\alpha-Fe_2O_3$ crystal the Fe is in a distorted octahedral site with three $O-H$ bonds at 1.946Å (with $O-Fe-O$ bond angles of 111.8°) and the other three bond at 2.116Å.[7] Our $Fe(OH)_3(H_2O)_3$ GVB cluster model of Fe_2O_3 postulates that the bonding in Fe_2O_3 can be described as follows:

(i) There are three covalent partially ionic (CPI) $Fe-O$ bonds with bond distances of 1.946Å. These correspond to the formal charge of +3 on the Fe. Each CPI bond involves some $4s$ and $4p$ atomic character on the Fe as the electron in each orbital is partially transferred to the oxygen atom.

(ii) The Fe also has five electrons in d orbitals (a d^5 configuration) coupled to high spin ($s = \frac{5}{2}$).

(iii) The remaining three $Fe-O$ bonds (2.116Å) are of donor-acceptor (DA) or Lewis acid-base type. This type of bond involves a lone pair on the O (the Lewis base) coordinating into the empty orbital on Fe (the Lewis acid).

V.3.2 Cluster Calculations for Fe_2O_3

To verify the GVB model of Fe_2O_3 we first performed quantum chemical calculations on the $Fe(OH)_3(H_2O)_3$ cluster. Full geometry optimization was carried out at the ROHF/LAV3P* level. We find that the optimized structure has three CPI bonds of 1.916Å (with $O-Fe-O$ bond angles of 109.3°) and three DA bonds of 2.259Å. In the GVB model the CPI bond should be approximately trans to a DA bond, and indeed the cluster leads to an average angle of 160.3° while the crystal leads to 162.2° between CPI and DA bonds. Also the $Fe-O-Fe$ bond angle in hematite along CPI bonds is 119.7° while the same $Fe-O-H$ bond angle in the cluster is 121.8°. The close correspondence of the geometries for the $Fe(OH)_3(H_2O)_3$ cluster and the Fe_2O_3 crystal (shown in in Figure V.1) confirms the validity of GVB model of Fe_2O_3.

To examine the character of bonding orbitals, we carried out GVB Perfect Pairing (GVB-PP)[8] calculations with LAV3P*. Here we correlated the three $Fe-O$ CPI bonds, the three $Fe-OH_2$ DA bonds, and all nine OH bonds. This amounts to a GVB(15/24) calculation. The GVB orbital contour diagram of the CPI bond is shown in Figure V.2a. One orbital corresponds closely to an sp^3 hybrid orbital on the O while the other has some Fe *sp* character in addition to the O character. The GVB overlap is 0.87, indicating a fairly ionic bond. The covalent nature of the bond is shown in the build up of electron density between the atoms. The ionic nature is clear by the greater participation of the oxygen orbitals in the both GVB orbitals. Figure V.2b shows two GVB orbitals of the $Fe-OH_2$ donor-acceptor bond from a GVB(24/24) calculation correlating all 24 valence pairs (to make the lone pairs unique). Here the orbitals correspond to the lone pair of the oxygen in the

(a)

(b)

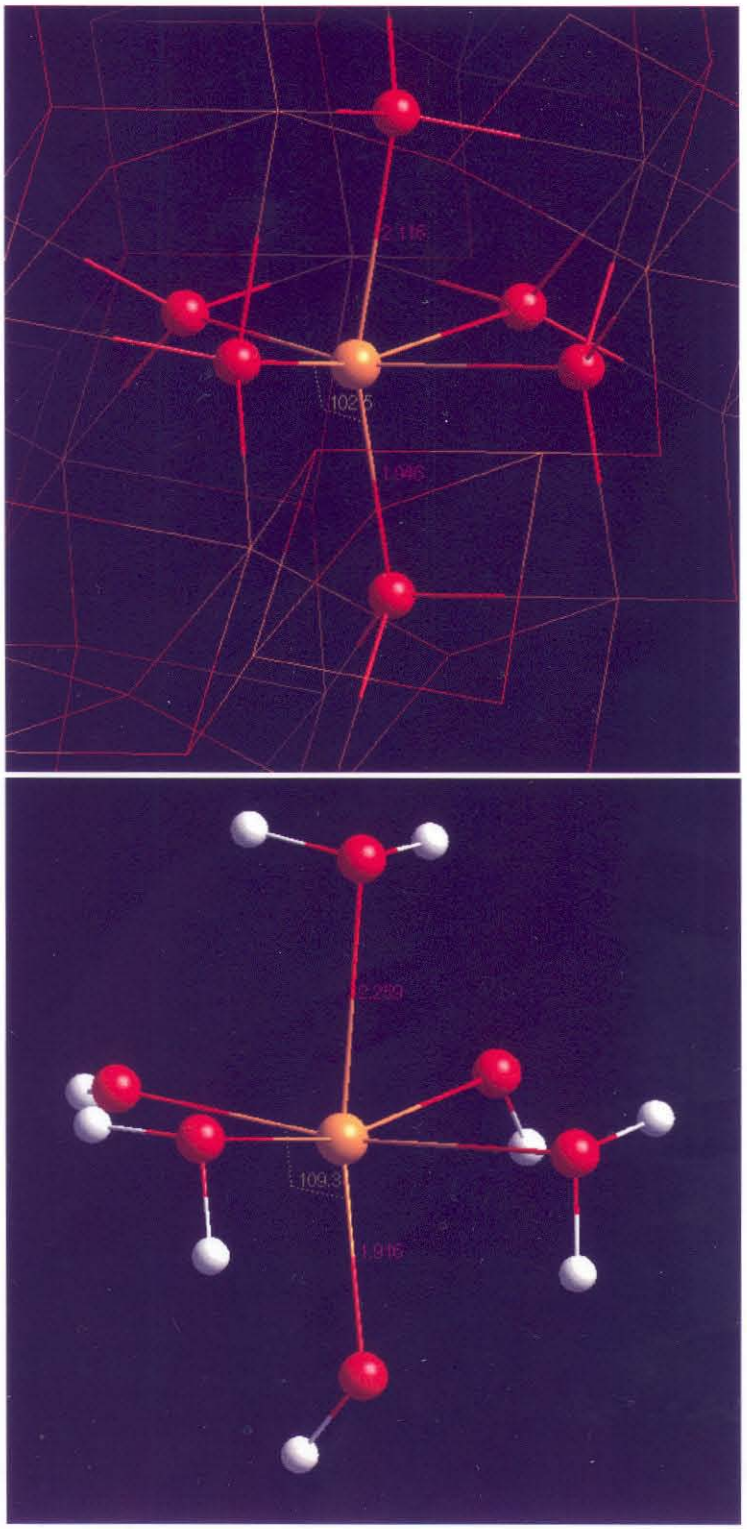

Figure V.1. (a) Geometry from the α–Fe_2O_3 crystal. (b) HF/LAV3P* optimized geometry of $Fe(OH)_3(H_2O)_3$ cluster.

(a)

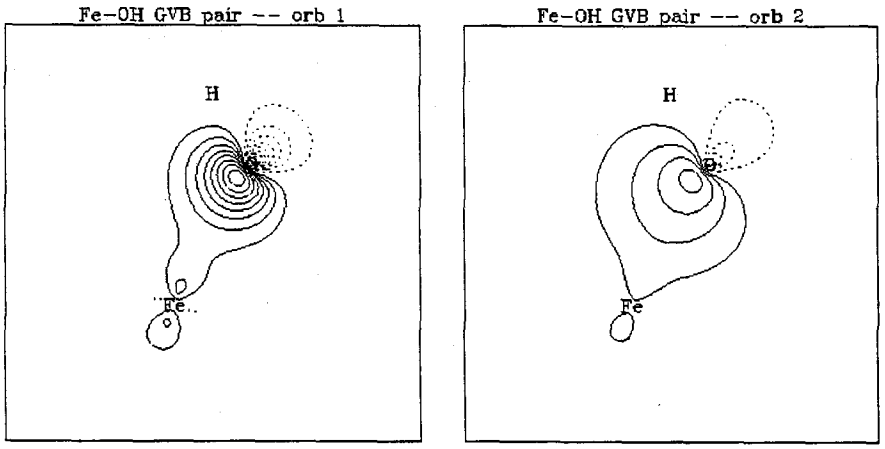

(b)

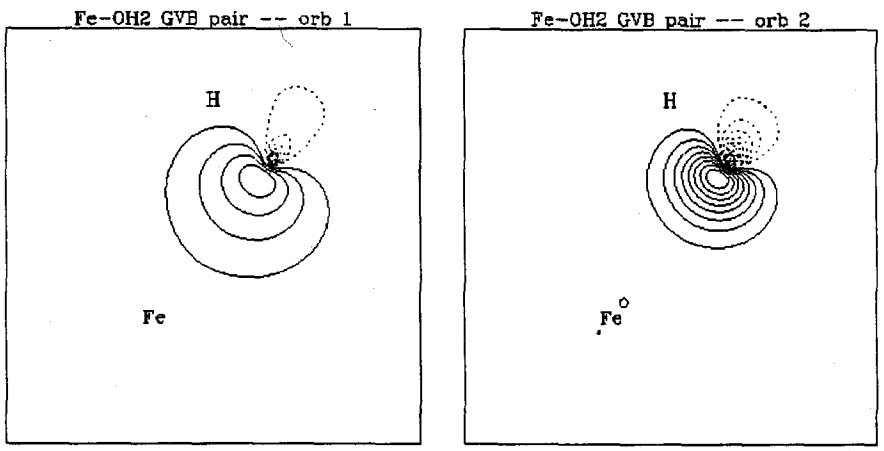

Figure V.2. GVB contour diagram of the electron pairs of (a) Fe–OH CPI bond. (b) Fe–OH_2 donor-acceptor bond.

H_2O, with in-out or radial correlation. This pair forms a Lewis base to Lewis acid bond to the Fe.

V.4 Oleic Imidazolines (OI)

The chemical structure of oleic imidazoline compound is illustrated in Figure V.3a. The molecule consists of an imidazoline head group, a short pendant amino-ethyl side group, and a long hydrocarbon tail group [1-(2-aminoethyl)-2(heptadec-8-enyl)-2-imidazoline]. In contrast to inorganic inhibitors which work by forming a relatively thick layer over the surface, OI is thought to form only a monolayer on the surface.[9] It is believed that the imidazoline ring is primarily responsible for binding the OI to the surface through the two ring nitrogens, while the hydrocarbon tail in OI acts as a hydrophobic barrier between the metal and the electrolyte. Once the monolayer has been formed, the hydrophobic group can thus inhibit corrosion reactions. The pendant side chain once was thought to be anchoring the molecule to the metal surface through the lone electron pair on the nitrogen in the amino group and was therefore regarded to be integral to the mechanism of adsorption of the molecule. However, corrosion studies[1] suggest that the nature of the group on the end of side chain does not appear to be critical to the efficiency of corrosion inhibition. We therefore put our focus only on the imidazoline head group in studying the surface reaction.

To understand how the imidazoline head group interacts with the Fe surface, electronic structure calculations were carried out on OI. Since we were only interested in the nature of the head group, we used a methyl group to replace the hydrocarbon tail to avoid unnecessary computation. The geometry was fully optimized at the HF/LAV3P* level. There are two N atoms in the imidazoline ring. One is sp^3-hybridized (N_{sp^3}) and the other is sp^2-hybridized (N_{sp^2}), each having one electron lone pair. It is believed the reason that N-containing molecules are often used as corrosion inhibitors is because the lone pair on N can bind to the Fe

(a)

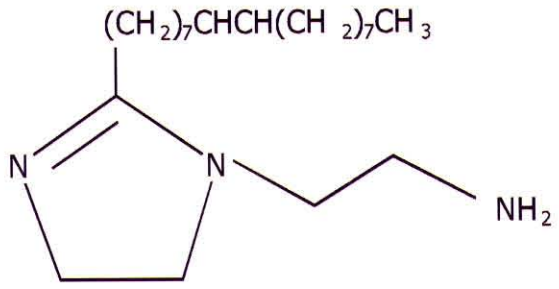

(b)

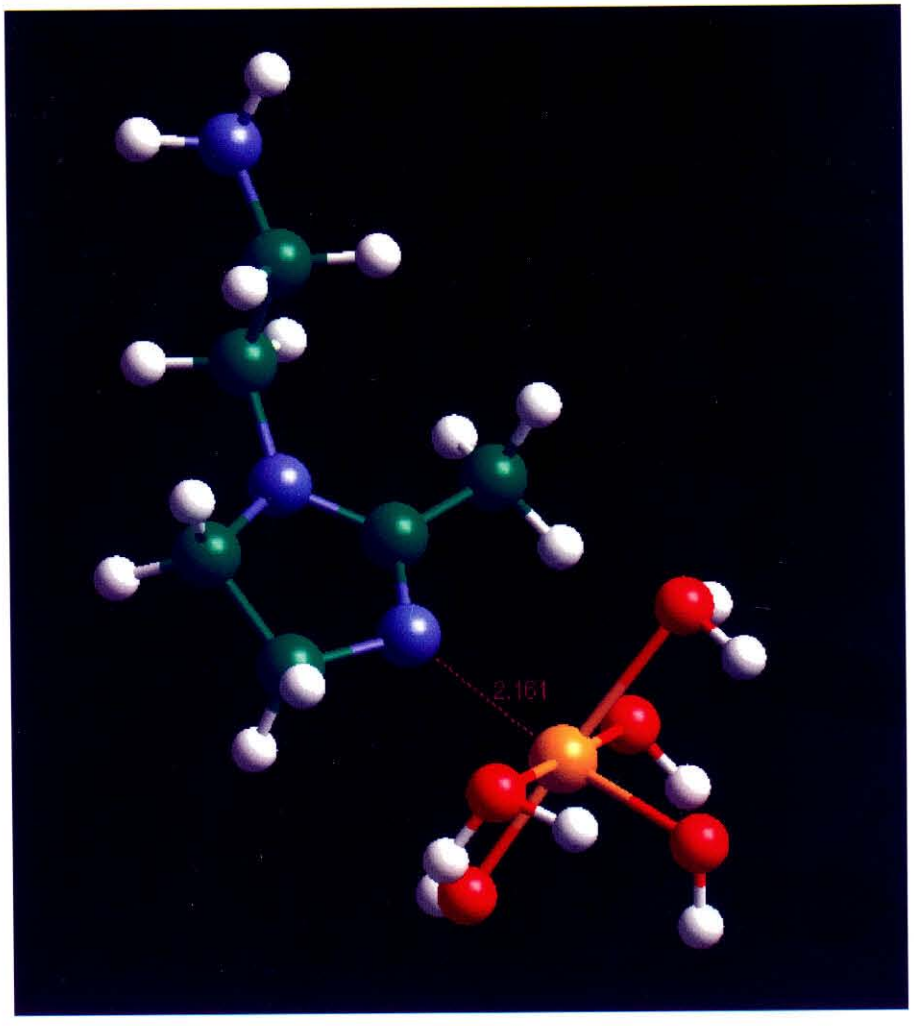

Figure V.3. (a) Chemical structure of OI. (b) HF/LAV3P* optimized geometry of OI over iron oxide cluster.

oxide surface via donor-acceptor (Lewis acid-base) type of reaction.[10] The higher orbital energy the donor electron pair has, the stronger adduct bond it can make due to the greater stability energy gained as a result of bonding. Since p orbital is higher in energy than s orbital, of the two N reaction centers in the imidazoline ring, the N_{sp^3} should be the one that binds to the Fe oxide surface. This was the assumption made by Edwards *et al.*[1] in their mechanistic study of OI corrosion inhibition. However, when we carried out geometry optimization calculation with OI on top of the iron oxide cluster (replacing one H_2O) to obtain an optimal bonding configuration, we found that the bonding between the N_{sp^3} and Fe did not lead to a minimum on the overall potential energy surface. Instead, the optimized structure indicates Fe binding to the N_{sp^2} atom as shown in Figure V.3b.

This seemingly puzzling result prompted us to look more into the electronic structure of the OI molecule. The lone pair electron density surface diagrams of N_{sp^3} and N_{sp^2} in the imidazoline ring are plotted out and shown in Figure V.4. The energy for the N_{sp^3} lone pair orbital, which happens to be the HOMO of the molecule, is higher in energy (by 2.12 eV) than for N_{sp^2} lone pair orbital. However, as shown in the density surface diagram, the N_{sp^3} lone pair electrons are practically delocalized over the imidazoline ring, mostly concentrated on the two ring N atoms. This electron delocalization is consistent with the fact that the imidazoline ring is found to be close to a planar structure. The density diagram for the N_{sp^2} lone pair, on the other hand, shows a large electron density lobe localized on the N_{sp^2}, along the direction where $N-Fe$ bond is found to form.

The preference of the oxide Fe to bond with N_{sp^2} over N_{sp^3} in OI can be explained through the concept of Lewis acid-base interaction,[11] where both orbital energies and characteristics of acid and base are the important factors in determining the strength of adduct bond. The donor orbital of N_{sp^3} though higher in energy, is delocalized in nature and can be considered as a "soft base," while the localized

(a)

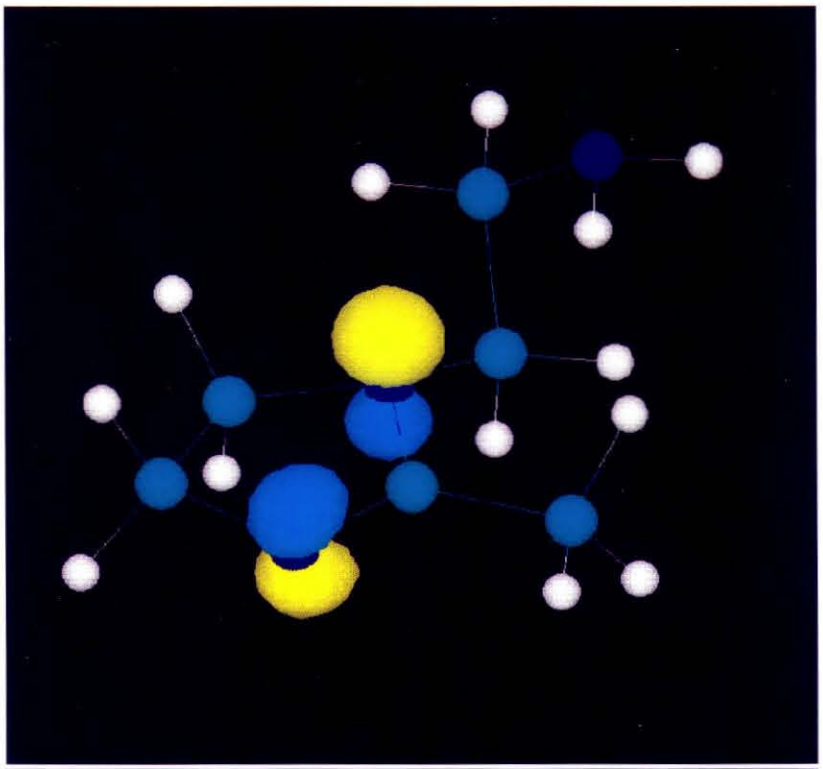

(b)

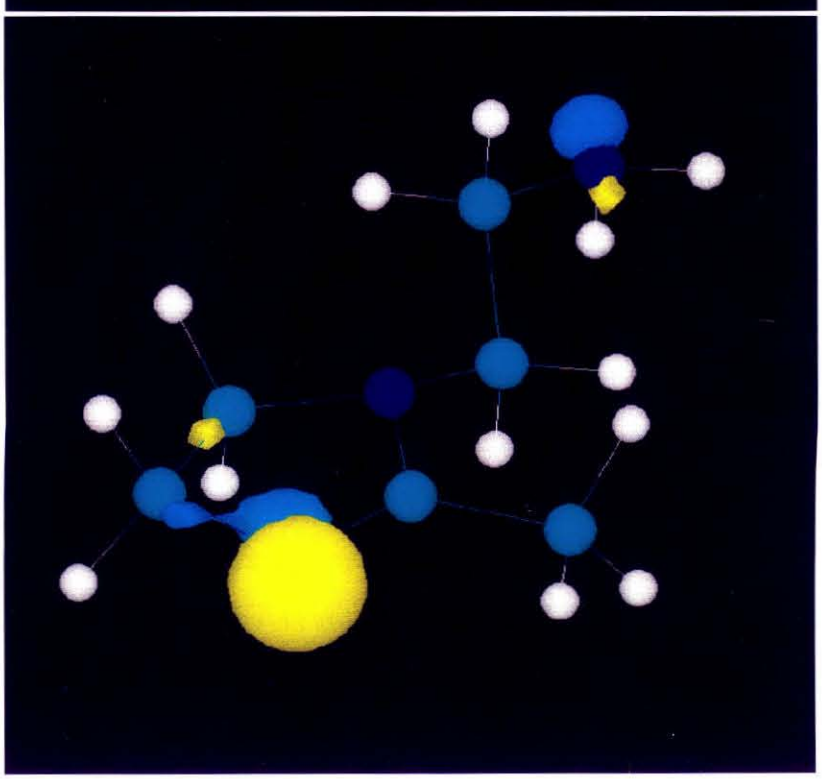

Figure V.4. Orbital density diagram of (a) N_{sp^3} lone pair of OI. (b) N_{sp^2} lone pair of OI.

donor in N_{sp^2} is considered as a "hard base." The Fe in $Fe(OH)_3(H_2O)_3$, due to its highly positive charge (+3), is in the "hard acid" category. According to the Hard-Soft Acid-Base (HSAB) rule from Pearson[12] that are widely used among chemists, hard acids prefer to associate with hard bases while soft acids with soft bases. This "rule of thumb" would expect Fe to make bond with N_{sp^2} instead of N_{sp^3}, as our calculation indicates. Based on this finding, we now have the knowledge of the orientation of OI over iron oxide surface. With that a self-assembled monolayer (SAM) mechanism for corrosion inhibition has been developed.[13]

V.5 Binding Energy Results

V.5.1 Binding Energies of N-containing Molecules

Now we have come to a point to determine the energetics involved when the iron oxide surface binds to corrosion inhibitor molecules where $Fe-N$ interaction is believed to be the dominant factor. We have first calculated the bond energies between various simple N-containing molecules ($Nmol$) and the iron oxide cluster. Instead of $Fe(OH)_3(H_2O)_3$, we used $Fe(OH)_3(H_2O)_2(Nmol)$ cluster to represent the oxide surface because one $Fe-H_2O$ bond needs to be replaced by the $Fe-Nmol$ bond. Table V.1 lists the $Fe(OH)_3(H_2O)_2-H_2O$ bond energy calculated using the three basis set schemes. The LACV3P* basis set (including an explicit treatment of the $3s$ and $3p$ core electrons of Fe) is the most accurate one among the three; however, the result of H_2O shows that LAV3P* leads to similar bond energies within 1 kcal/mol. The outmost core electrons of Fe appear to play a minimal role in bonding energy, which can be excluded from the valence space without losing much accuracy. Thus the simple treatment of only the eight valence electrons on the Fe should be adequate. Similarly the smaller LANL1DZ basis set gives results (for H_2O and OI) comparable to the more extensive LAV3P* basis. This indicates that within the scope of Hartree-Fock approximation and current basis sets, the extensiveness of basis set does not really have a significant effect on the energy

results. Therefore, we used LAVL1DZ to carry out further calculations.

The bond energies calculated (UHF/LANL1DZ) for various N-containing molecules are also listed in Table V.1. The snap bond energy reflects the electronic effects without steric factors. With NH_3 the snap bond energy is 28.8 kcal/mol . compared to the snap bond energy 24.9 kcal/mol of H_2O calculated at the same level. These results are expected for Lewis acid-base bonds since NH_3 is a stronger Lewis base than H_2O. The calculated adiabatic bond energies for NH_3 and H_2O are 12.2 and 11.7 kcal/mol, respectively, indicating the importance of steric effects. These calculations show that the N_{sp^2} ligand $NH{=}CH_2$ makes compatible or slightly stronger bond to $Fe(OH)_3(H_2O)_2$ than the N_{sp^3} ligand $NH_2{-}CH_3$, but both are much stronger ligands than the N_{sp} ligand $N{\equiv}CH$. Calculations show an exceptionally large snap bond energy of 41.77 kcal/mol (adiabatic bond energy 14.76 kcal/mol) for the N_{sp^2} of imidazoline bonding to the Fe atom of $Fe(OH)_3(H_2O)_2$, indicating a special role of the imidazoline ring which we believe makes the N_{sp^2} an even stronger electron donor. This strong bonding is consistent with the excellent corrosion inhibition for OI compounds.

V.5.2 Binding of OI

On the surface of Fe_2O_3 we expect the OI to bond strongly as a Lewis base to the Fe^{3+}. In aqueous environments we assume that on the surface it must displace a surface H_2O in order to make bond to Fe. From the optimized structure of $Fe(OH)_3(H_2O)_2$(OI), we calculated the average $Fe{-}OH$ distance to be 1.930Å (an increase of 0.014 Å) with an $O{-}Fe{-}O$ angle of 105.97° (a decrease of 3.3°). The average DA bond is 2.358 Å to H_2O (an increase of 0.20 Å) with an $Fe{-}$OI bond of 2.161 Å.

Using the more accurate LAV3P* energy results, the snap bond energy (no change in other ligands) is about 37.0 kcal/mol for OI compared to 22.3 kcal/mol for H_2O. This indicates that the dative bond due to the N_{sp^2} lone pair orbital of

Table V.1. Quantum Mechanical Calculation of Bond Energy Results for $Fe(OH)_3(H_2O)_2 - (molecule)$

	LANL1DZ	LAV3P*	LACVP*
(a) Cluster $Fe(OH)_3(H_2O)_2 - OH_2$			
Bond Energy $(Fe \cdots OH_2)$			
Snap	24.94	22.28	22.46
Adiabatic	11.72	12.88	11.75
(b) Cluster $Fe(OH)_3(H_2O)_2 - NH_3$			
Bond Energy $(Fe \cdots NH_3)$			
Snap	28.82		
Adiabatic	12.24		
(c) Cluster $Fe(OH)_3(H_2O)_2 - NH_2CH_3$			
Bond Energy $(Fe \cdots NH_2CH_3)$			
Snap	30.14		
Adiabatic	12.28		
(d) Cluster $Fe(OH)_3(H_2O)_2 - NHCH_2$			
Bond Energy $(Fe \cdots NHCH_2)$			
Snap	29.46		
Adiabatic	12.49		
(e) Cluster $Fe(OH)_3(H_2O)_2 - NCH$			
Bond Energy $(Fe \cdots NCH)$			
Snap	11.85		
Adiabatic	0.44		
(f) Cluster $Fe(OH)_3(H_2O)_2 - OI$			
Bond Energy $(Fe \cdots OI)$			
Snap	41.77	36.89	
Adiabatic	14.76	16.57	

OI is considerably stronger than that of the O_{sp^3} lone pair orbital of H_2O.

Allowing the ligand and the oxide cluster to relax after breaking the bond (the adiabatic bond energy), the desorption energy for OI is 16.6 kcal/mol versus 12.9 for H_2O. The decreased adiabatic bond energy versus the snap bond energy reflects crowding in the six coordinate site.

Combining these quantities we estimate the energetics in (V.1)

$$Fe(OH)_3(H_2O)_3 + OI \rightarrow Fe(OH)_3(H_2O)_2(OI) + H_2O \qquad (V.1a)$$

$$\Delta E^{AD} = -3.7 \text{ kcal/mol (exothermic)} \qquad (V.1b)$$

$$\Delta E^{snap} = -14.7 \text{ kcal/mol.} \qquad (V.1c)$$

Removing an H_2O from the OI complex, leads to (V.2)

$$Fe(OH)_3(H_2O)_2(OI) \rightarrow Fe(OH)_3(H_2O)(OI) + H_2O \qquad (V.2a)$$

$$\Delta E^{AD} = +9.7 \text{ kcal/mol (endothermic)} \qquad (V.2b)$$

$$\Delta E^{snap} = +20.6 \text{ kcal/mol} \qquad (V.2c)$$

These calculations indicate that OI adsorbs to the iron cluster more strongly than water. On the Fe_2O_3 surface, constraints due to the Fe_2O_3 framework should lead to energetics intermediate between snap (which allows no ligand rearrangement) and adiabatic (allowing full rearrangement). In addition, we expect that the Fe for the Fe_2O_3 surface will be more positive than in the cluster (since neighboring Fe are more electron-positive than H), leading to larger bond energies. This agrees with the experimental observation that OI molecules absorb rapidly on the iron oxide surface.[14]

V.6 Conclusion

In this chapter we have developed a GVB cluster model of crystalline $\alpha-Fe_2O_3$. With such a simple model we are able to describe the local geometry and bonding of Fe in the bulk oxide. Using quantum mechanical calculations on the $Fe(OH)_3(H_2O)_2$ cluster, we have determined the orientation of OI molecule bonding to the oxide surface. We found that the N_{sp^2} in the imidazoline ring is the reaction center. We have also determined the relative binding strength of OI and other nitrogen containing molecules to the iron oxide surface and concluded that OI molecules bond very strongly to the Fe on the surface. In aqueous environments they are able to replace water on the surface so that they can form a protective layer to prevent corrosion.

Chapter V References

1. A. Edwards, C. Osborne, S. Webster, D. Klenerman, M. Joseph, P. Ostovar, and M. Doyle, *Corros. Sci.* **36**, 315, 1994.
2. P. J. Hay and W. R. Wadt, *J. Chem. Phys.* **82**, 299, 1985.
3. A. D. McLean and G. S. Chandler, *J. Chem. Phys.* **72**, 5639, 1980.
4. (a) N. M. Ringnalda, J. M. Langlois, B. H. Greeley, R. B. Murphy, T. V. Russo, C. Cortis, R. P. Muller, B. Marten, R. E. Donnelly, D. T. Mainz, J. R. Wright, T. Pollard, Y. Cao, Y. Won, G. H. Miller, W. A. Goddard III, and R. A. Freisner, PS-GVB v2.2, Schrodinger, Inc.: Portland, OR, 1995; (b) B. H. Greeley, T. V. Russo, D. T. Mainz, R. A. Friesner, J. M. Langlois, W. A. Goddard III, R. E. Donnelly, and M. N. Ringnalda, *J. Chem. Phys.* **101**, 4028, 1994.
5. J. C. Scully, *The Fundamentals of Corrosion*, 3rd ed., Pergamon Press, Oxford, 1990.
6. H. H. Uhlig and R. W. Revie, *Corrosion and Corrosion Control*, 3rd ed., Wiley, New York, 1985.
7. R. L. Blake, R. E. Hessevick, T. Zoltai, and L. W. Finger, *Amer. Mineral.*, **51**, 911, 1966.
8. F. W. Bobrowicz and W. A. Goddard III, *Modern Theoretical Chemistry: Methods of Electronic Structure Theory*, H. F. Schaefer, 3rd ed., Plenum, New York, 1977.
9. M. Joseph, J. Hodge, and D. Klenerman, *Faraday Discuss* **94**, 273, 1992.
10. E. Stupnisek-Lisac, M. Metikos-Hukovic, D. Lencic, J. Vorkapic-Furac, and K. Berkovic, *Corrosion Science* **48**, 924, 1992.
11. W. B. Jensen, *Chem. Rev.* **78**, 1, (1978).
12. R. G. Pearson, *J. Am. Chem. Soc.* **85**, 3533, (1963).
13. S. Ramachandran, B. L. Tsai, M. Blanco, H. Chen, Y. Tang, and W. A.

Goddard III. *Langmuir* **12**, 6419, (1996).

14. D. Klenerman, J. Hodge, M. Joseph, *Corros. Sci.***36**, 301, 1994.

Appendix D: Correlation Between Electronegativity and Bond Angle

D.1 Introduction

Electronegativity (EN) is an intuitive concept that can provide chemists with explanations for a wide range of molecular properties. It plays a prominent role in all elementary chemistry courses and has become part of the daily thinking pattern of most practicing chemists. The chemical concept of EN was originally introduced in Pauling's 1932 paper[1]: the difference in electronegativity between atoms A and B in a molecule determines the polarity of the A−B bond, i.e., its ionic character. Pauling developed a relative scale based on empirical thermochemical data for heats of formation and defined EN, a unitless parameter that can nevertheless be related to energies, as "the power of an atom in a molecule to attract electrons to itself".[2] Because the definition of EN is only a qualitative one, there have been numerous improved or alternative scales developed since Pauling's.[3] Even though these scales agree generally in their relative ordering of elements, it is only true in the broadest sense. Inconsistencies often exist and there has not been agreement on which scale provides the best description of EN.

EN is clearly a molecular property as described in Pauling's definition (i.e. "in a molecule"). However for obvious practical reasons, electronegativities have always been tabulated as atomic (or hybrid atomic orbital) values. Observable quantities such as bond distance and energy,[4,5] dipole moment polarizability,[6] ionization energy (IE) and electron affinity (EA),[7] have been directly or indirectly linked to the scale of EN and are often served to evaluate the numerous existing EN scales. Many of the observable (or closely related quantities), nevertheless, are also used in the definitions of various EN scales and therefore cannot be objective measures of these scales.

From the iron oxide cluster study in Chapter V, we have discovered that the $Fe{-}O{-}H$ bond angle value appears to depend on the charge nature of the Fe. This angle is found to be 129° for ferrus Fe^{2+} and 122° for ferric Fe^{3+}. To rationalize this observation, if we consider the bond angle to be mainly determined by the hybridization of O bond orbitals, since the $2s$ orbital is more electronegative than the $2p$ orbital, energetically it is more favorable for O to use $2s$ orbital to make bond to an electropositive atom (such as Fe) where electron transfer to O is likely to occur. The more O_{2s} character involved in the bonding will result in a larger bond angle. Since Fe^{2+} is more electropositive than Fe^{3+} (it is easier for Fe^{2+} to loose another electron than Fe^{3-}), the above molecular orbital analysis can explain why Fe^{2+} has a larger $Fe{-}O{-}H$ bond angle. Theoretically the bond angles for O under normal bonding conditions can range from 90° (p^2 hybrid) to 180° (sp hybrid). If we can correlate the O bond angle with the EN of the atom O bonds to, with bond angle 90° being the electronegative limit and 180° being the electropositive limit, we may have a well-defined and directly measurable (or at least easily calculable) quantity that can serve to independently evaluate EN scales or even become a correlational device of EN for atoms or molecular groups.

To study the correlation between O bond angle and EN, we have carried out *ab initio* calculations on main group elements. In the following section, Section 2 describes the computational details. The results and discussion are in Section 3 and 4. Application is discussed in Section 5. Conclusion is in Section 6.

D.2 Computational Method

To calculate the bond angle of A$-O-H$ where A is a main group element, the compound with formula H_nA$-OH$ was used. The value of n was taken to be either (i) (group number $-$ 1) for Group 1 $\sim$ 4 elements, or (ii) (7 $-$ group number) for Group 5 $\sim$ 7 elements. This way all the elements are in their full valence-satisfied states. Noble gases were not included in this study since they do not form bond

with $-OH$. Calculations were performed on elements in the first 5 rows from the periodic table. Geometries of H_nA$-OH$ compounds were fully optimized at the HF level with LAV3P* basis sets[8] using PSGVB program. Energy calculations for Section 5 were done at the MP2 level using all electron MSV basis sets[9] augmented with two sets of p, d, or f polarization functions.

D.3 Result

Bond angle calculation results are listed in Table D.1. It is a well-known fact that the atom becomes more electronegative across each period of the periodic table because of the corresponding increase in effective nuclear charge. The calculated $\angle H_n$A$-O-H$ decreases monotonously across each period, which is consistent with the EN trend. The real test of the correlation between $\angle H_n$A$-O-H$ and EN would be to compare all atoms, not just the ones in the same period. One way to do the comparison is to plot out all $\angle H_n$A$-O-H$ against an accepted EN scale. Since among the numerous scales there is no consensus on which one is the best, we therefore have investigated several popular EN scales. These are

(a) χ_P – Pauling's scale derived from bond energies. We used the corrected Pauling values (with better thermodynamic data) from Allred.[10]

(b) χ_{AR} – an empirical scale from Allred and Rochow.[11] It regards EN as a electrostatic force and is a function of atom's size and effective nuclear charge (Z_{eff}).

(c) χ_S – another scale based on charge and size from Sanderson.[12] It differs from Allred and Rochow's in that relative electron density instead of Z_{eff} was used.

(d) χ_{Spec} – an alternative spectroscopic scale from Allen.[13] It is based on the average one-electron energy of valence electrons in the ground-state free atom.

(e) χ_M – the theoretical and absolute scale from Mulliken revised by converting to Pauling units.[14] It is the average of ionization potential (IP) and electron

Table D.1. Various EN Scales *vs.* Calculated $\angle H_n\text{A}{-}O{-}H$ for Atom A

Atom A	χ_P^a	χ_{AR}^b	χ_S^c	χ_{Spec}^d	χ_M^e	$\angle H_n\text{A}{-}O{-}H$
H	2.20	2.20	2.59	2.30	3.06	105.5°
Li	0.98	0.97	0.89	0.91	1.28	179.9°
Be	1.57	1.47	1.81	1.58	1.99	137.4°
B	2.04	2.01	2.28	2.05	1.83	114.0°
C	2.55	2.50	2.75	2.54	2.67	109.0°
N	3.04	3.07	3.19	3.07	3.08	104.1°
O	3.44	3.50	3.65	3.61	3.22	102.1°
F	3.98	4.10	4.00	4.19	4.44	99.8°
Na	0.93	1.01	0.84	0.87	1.21	180.0°
Mg	1.31	1.23	1.32	1.29	1.63	173.5°
Al	1.61	1.47	1.71	1.61	1.37	124.0°
Si	1.90	1.74	2.14	1.92	2.03	117.1°
P	2.19	2.06	2.52	2.25	2.39	110.0°
S	2.58	2.44	2.96	2.59	2.65	107.4°
Cl	3.16	2.83	3.48	2.87	2.54	103.7°
K	0.82	0.91	0.45	0.73	1.03	180.0°
Ca	1.00	1.04	0.95	1.03	1.30	179.8°
Ga	1.81	1.82	2.42	1.76	1.34	119.7°
Ge	2.01	2.02	2.62	1.99	1.95	116.1°
As	2.18	2.20	2.82	2.21	2.26	110.6°
Se	2.55	2.48	3.01	2.42	2.51	108.4°
Br	2.96	2.74	3.22	2.69	3.24	105.2°
Rb	0.82	0.89	0.31	0.71	0.99	180.0°
Sr	0.95	0.99	0.72	0.96	1.21	179.8°
In	1.78	1.49	2.14	1.66	1.30	121.1°
Sn	1.80	1.72	1.49	1.82	1.83	118.9°
Sb	2.05	1.82	2.46	1.98	2.06	113.4°
Te	2.10	2.01	2.62	2.16	2.34	111.0°
I	2.66	2.21	2.78	2.36	2.88	108.0°

[a] Pauling values.

[b] Allred-Rochow values.

[c] Sanderson values.

[d] Allen values.

[e] Mulliken values.

affinity (EA) of the ground state atom or orbital.

The calculated $\angle H_n\text{A}{-}O{-}H$ result ranges from 100° (F atom) to 180° (alkali metals), corresponding to the two electronegativity extremes for atoms in the periodic table. When $A = H$, the calculated angle is 105.5°, suggesting H is more electronegative than C (109.4°). This obviously does not agree with experimental observations. The failure to determine H electronegativity also occurs among several other EN scales such as Allred-Rochow (H value is close to zero; uses Pauling's value instead) and Mulliken (H is also more electronegative than C). The problematic nature of H may be due to its small size and lack of core electrons. This is manifest in its ambiguous placement in the periodic table as head of Group I or Group VII or often slightly to the left of carbon. We have regarded H as a special case and have plotted out $\angle H_n\text{A}{-}O{-}H$ against EN scales for all the other atoms investigated but H. One more point to note is that, to test the angle values against a scale presumably implies verification of the validity of the scale in question, which is not true in this case. Of the five EN scales listed above, each has its own share of critics. When evaluating these plots, an independent judgment should always be maintained.

In Figure D.1 the calculated $\angle H_n\text{A}{-}O{-}H$ values are plotted against the Pauling electronegativities. A correlation between $\angle H_n\text{A}{-}O{-}H$ and EN is clearly shown for atoms across the four periods. Even though there are two minor misorderings: $\chi_P(I) > \chi_P(S)$ while $\angle I{-}O{-}H > \angle S{-}O{-}H$; $\chi_P(Ga) > \chi_P(Sn)$ while $\angle Ga{-}O{-}H > \angle Sn{-}O{-}H$, it may also be argued that the errors are due to χ_P since the first misordering would have disappeared if any one of the χ_{AR}, χ_S, and χ_{Spec} had been used instead. The same would have happened for the second misordering if χ_{Spec} or χ_M had been used. The point to note here is that a few glitches in the curve does not mean the correlation fails, especially when the EN scale itself is not perfect. The degree of correlation should be observed from a bigger picture,

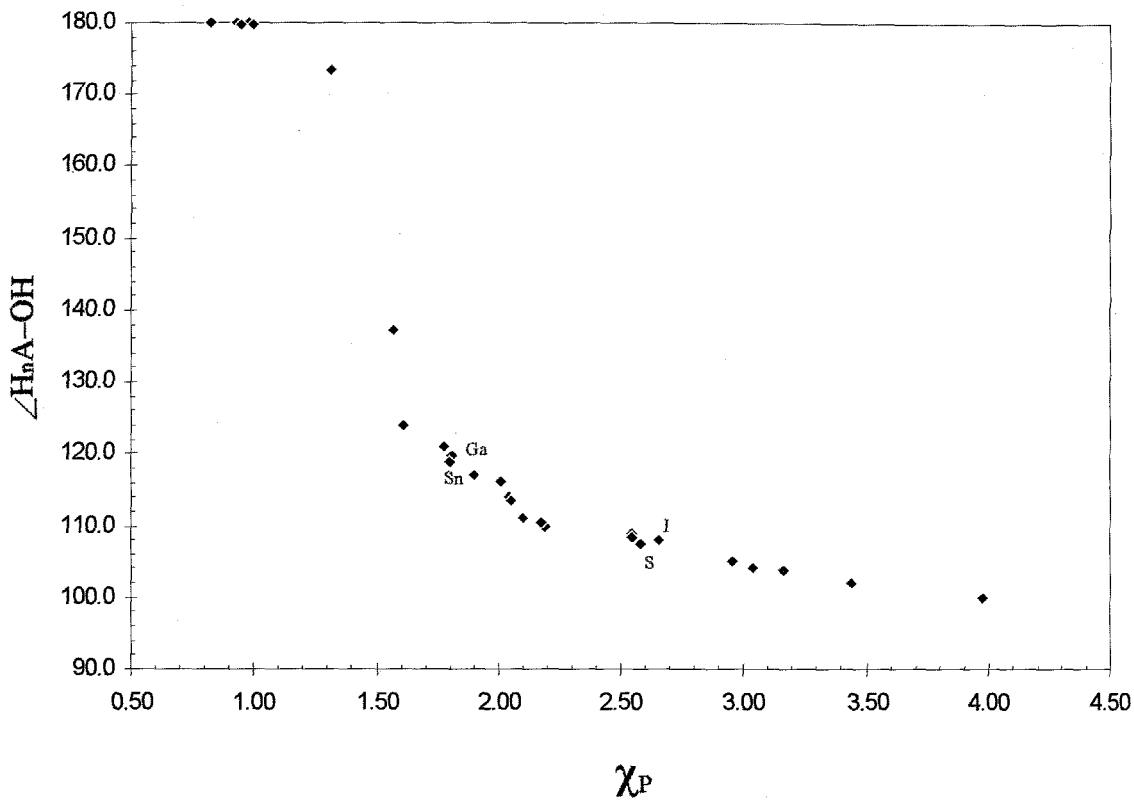

Figure D.1. Calculated $\angle H_nA–OH$ vs. Pauling EN scale.

which is very high in this case. The correlation curve does not appear to be very "smooth," which may be improved if better basis sets and theories are used in the calculation, but the overall angle and EN agreement is very well, considering all the atoms come from different groups and periods, and have different bonding states.

Figure D.2~D.5 are plots of $\angle H_n\text{A}{-}O{-}H$ against χ_{AR}, χ_S, χ_{Spec}, and χ_M, respectively. The misordering errors are quite large for Allred-Rochow and Sanderson scales (Figure D.2 and D.3) compared to Pauling scale even though strong angle *vs.* EN correlations do exist for these two. This disagreement is probably due to the fact that both scales are based on ground state atomic properties (charges and radii) and do not have good description of atoms in molecular bonding, which should be a determining factor of the angle value. The Allen scale is based on the one-electron energy averaged over valence shells and thus reflects the EN of the bonding orbital. The agreement shown in Figure D.4 is indeed quite well. For Mulliken scale (Figure D.5) the main deviation comes from Group II atoms (Be,Mg), which is due to the intrinsic error in the definition of EN for these atoms. The ground state atomic s^2 configuration is normally used to obtain the IP and EA needed to define the EN for Group II in Mulliken scale. This definition obviously is not entirely correct since when the Group II atom is engaged in molecular bonding, a considerable p contribution is involved. In Section 5 we will discuss how this problem can been addressed through molecularly derived IP and EA.

D.4 Discussion

We think that we have established an unambiguous correlation between the bond angle $\angle H_n\text{A}{-}O{-}H$ and the electronegativity of atom A. The physics behind this correlation is that the hybridization of the two O bonding orbitals will adjust themselves to reach a optimal state (depending on the electron attracting or withdrawing ability of A) when OH makes bond to A. The more electronegative A is, the more O_{2p} character will result in the hybridization (smaller $\angle\text{A}{-}O{-}H$) and

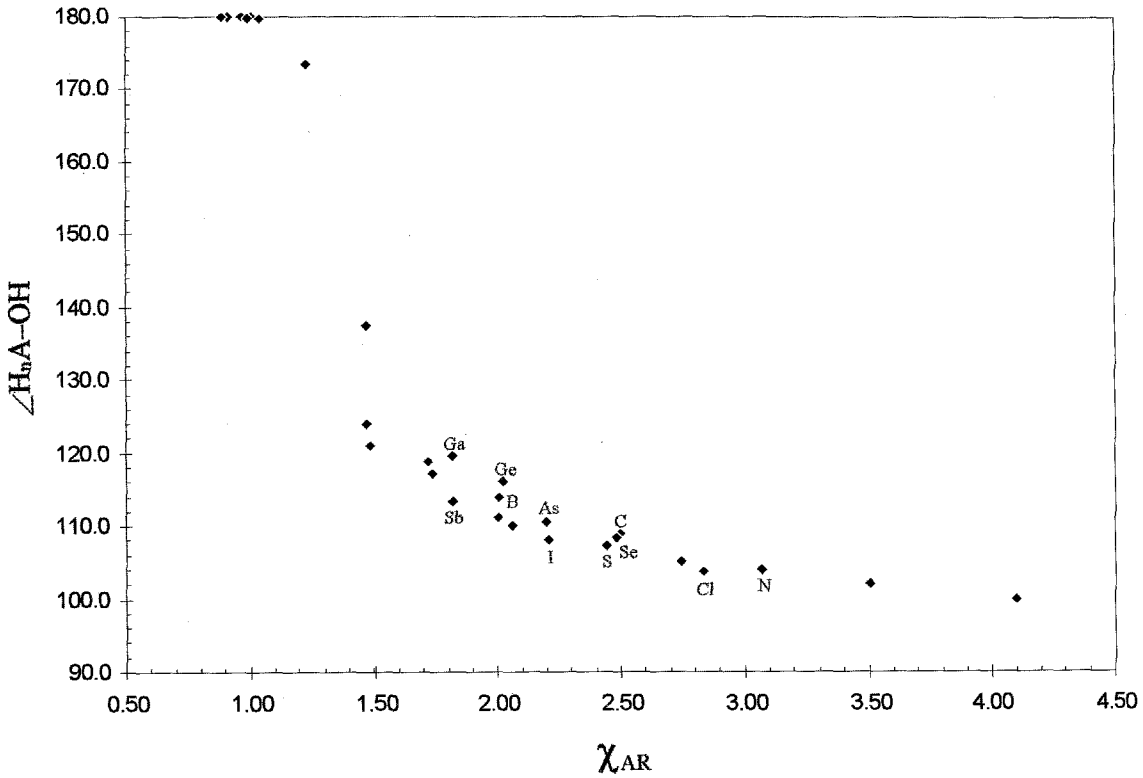

Figure D.2. Calculated $\angle H_nA–OH$ vs. Allred-Rochow EN scale.

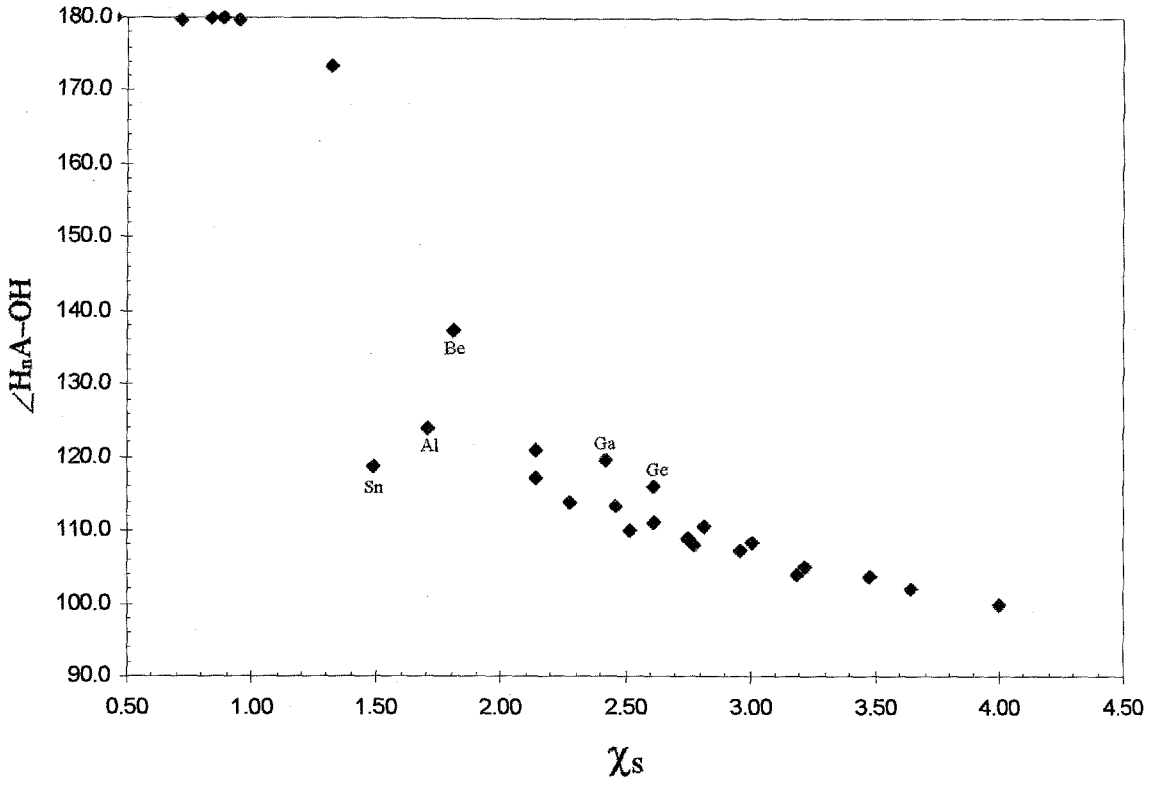

Figure D.3. Calculated $\angle H_nA–OH$ vs. Sanderson EN scale.

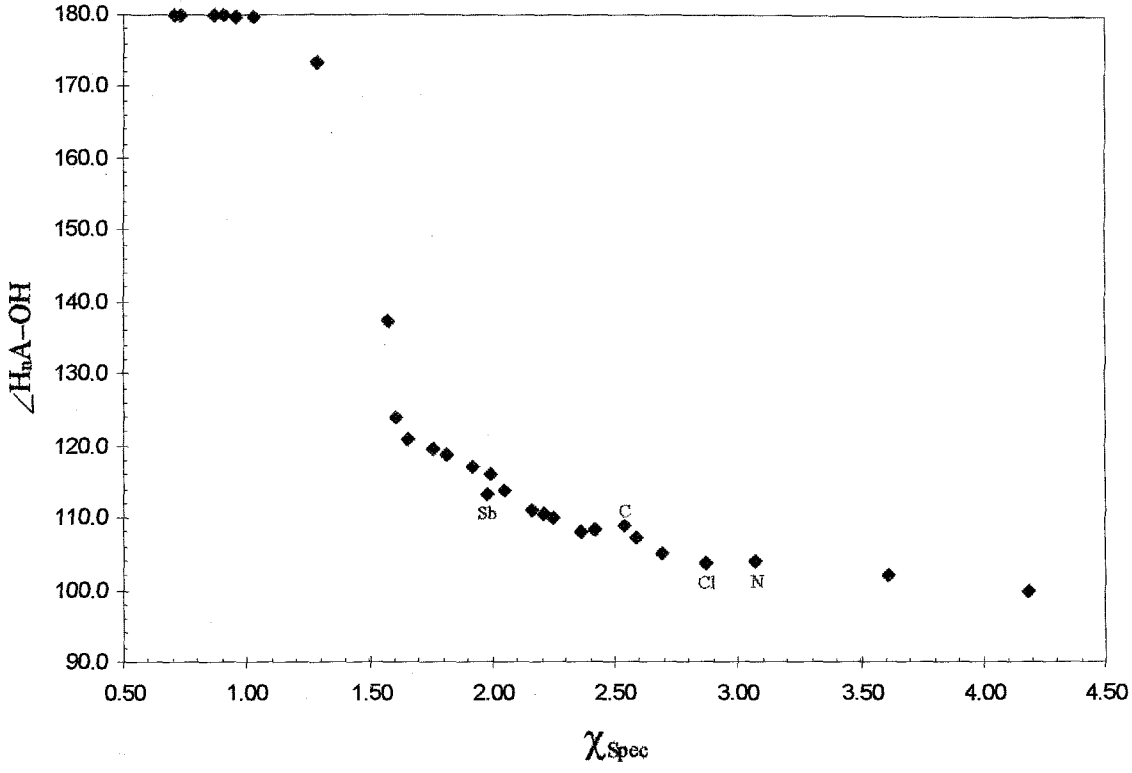

Figure D.4. Calculated $\angle H_nA–OH$ vs. Allen EN scale.

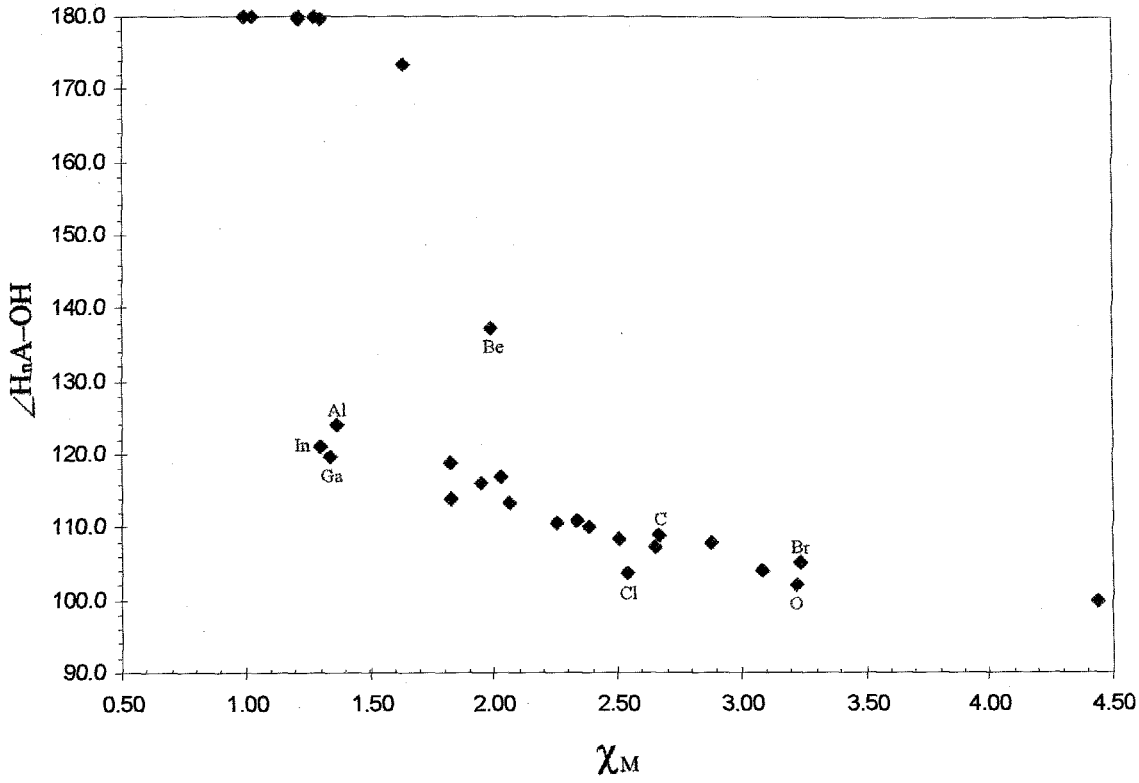

Figure D.5. Calculated $\angle H_nA–OH$ vs. Mulliken EN scale.

vice versa. This leads to an angle window of 90° (from 90° to 180°) to accommodate the entire electronegativity spectrum.

Even though Pauling's EN scale was first introduced 65 years ago, currently it is still the most accepted scale and has been frequently and systemically employed by chemists and physicists to guide them in answering practical problems in chemical bonding. The fact that $\angle H_n\text{A}{-}O{-}H$ correlates excellently with the χ_P of A would provide a useful corelational tool for determining the relative electronegativities among atoms and molecules. The ability to predict such quantities prior to synthesis is of great importance in optimizing any system for both organic and inorganic chemists. The value of $\angle H_n\text{A}{-}O{-}H$ does not discriminate alkali metals and some Group II metals (Ca, Sr). All of them are very electropositive and lead to an angle of $\sim 180°$. This however does not impose serious limitations on the usage of the angle scale, because most atoms or molecules whose electronegativities are ambiguous or of interest are those with moderate electronic nature.

The angle scale can provide a fast and straight-forward way to determine relative electronegativities. It is well-positioned to be applied to molecular groups and transition metals; both are troublesome cases for the current EN scales. Since we know that EN of an atom is actually a molecular property and depends on the chemical environment the atom is in, the current scales tabulated as atomic values do not take this consideration into account. For example, the C in $C(OH)_3$ is obviously more electronegative than the C in CH_3 and yet none of the existing EN scales can reflect the difference. The $\angle C{-}O{-}H$ calculated for the former is 108° which is smaller than the later (109°), indicating the usefulness of the angle scale to correlate group electronegativities. The electronegativities for transition metals have always been very difficult to determine because of the large errors in thermodynamics data, their multi-valence nature, and the uncertainty in d orbital contribution in bonding. On the angle scale they are treated just like main group

Table D.2. Various EN Scales *vs.* Calculated $\angle HM{-}O{-}H$ for Transition Metal M(2+)

M	χ_P	χ_{AR}	χ_S	$\angle H_n A{-}O{-}H$
Sc	1.36	1.20	1.02	179.9°
Ti	1.54	1.32	0.64	179.9°
V	1.63	1.45	0.69	148.8°
Cr	1.66	1.56	1.24	148.7°
Mn	1.55	1.60	1.66	144.8°
Fe	1.83	1.64	1.64	136.0°
Co	1.88	1.70	1.96	129.0°
Ni	1.91	1.75	1.94	131.9°
Cu	1.90	1.75	2.03	123.6°
Zn	1.65	1.66	2.22	122.5°

elements. The $\angle H_n A{-}O{-}H$ will be decided by the molecule itself through its optimal bonding configuration. We have calculated the bond angle values for the first row transition metals. The M^{2+} state was used for all metals. They are listed in Table D.2 along with available EN scales.

D.5 Application

The concept of electronegativity equalization was proposed by Sanderson[15] in 1951 which states that when atoms are joined together, their initial electronegativities will equalize to the same intermediate EN. Iczkowsky and Margrave[16] suggested that the Mulliken electronegativity, $\chi_M = \frac{1}{2}$ (IP+EA), is equal to the chemical potential $\mu = -\frac{\partial E}{\partial Q}$. In addition to this, Parr and Pearson[17] also identified the physical significance of the quantity (IP − EA) as 2 times the atomic hardness η_A°. Based on these theories, Rappé and Goddard[18] developed a charge equilibration (QEq) approach for predicting charge distribution in molecules for use in molecular dy-

namics simulations. The two main atomic parameters used in this approach are χ_M and J_A =(IP − EA), where IP and EA are taken from atomic data corrected for exchange interactions present in atoms but absent in molecules.[19] The problem with the atomically derived IP and EA (and the Mulliken electronegativities in general) is that they may not represent the valence electrons involved in the actual molecular bonding. Even with the improved form of the Mulliken definition, "valence state χ_v," which identifies a specific atomic hybridization and computes IP_v and EA_v from ground-state IP and EA plus promotion energies to the atomic excited state designated,[20] there is still a major difficulty of this method which is that there is no a priori knowledge on which valence state assignment to make before molecular bonding.

One way to circumvent the above obstacle is to use molecularly derived IP and EA. The molecular IP or EA of atom A can be calculated from H_nA$-O-H$ by removing the $-OH$ and subtracting or adding an electron to the remaining H_nA fragment. There is no pre-defined valence state used for the atom. The IP and EA are thus obtained from the optimal bonding orbital configuration of the atom. The calculated IP and EA along with derived χ_A and η_A are listed in Table D.3. The new η and χ parameters agree well with chemical trends and more importantly, the χ misorderings for Group II elements found in the old parameters are corrected. The QEq parameters for transition metals can be derived in the same way.

Another possible application of this angle-electronegativity correlation is to include the effect in the force field description of the O bond angle terms used in molecular mechanic calculation. Instead of having the equilibrium angle pre-set to be a certain constant, it can be allowed to vary dynamically depending on what atom or group the $-OH$ is bonded to.

D.6 Conclusion

In this appendix, we have reported for the first time the correlation between

Table D.3. Revised QEq Parameters (in ev) for Main Group Elements

Atom A	IP	EA	η	χ	η'^{a}	χ'^{a}
Li	5.34	0.30	2.52	2.82	2.39	3.01
Be	8.24	0.13	4.06	4.19	4.44	4.88
B	9.23	-0.20	4.72	4.52	4.23	4.07
C	10.64	0.21	5.21	5.43	5.06	5.34
N	12.59	0.72	5.94	6.66	5.88	6.90
O	16.13	1.94	7.10	9.04	6.68	8.74
F	21.03	3.56	8.73	12.30	7.47	10.87
Na	4.90	0.29	2.30	2.59	2.30	2.84
Mg	6.83	0.49	3.17	3.66	3.69	3.95
Al	7.74	0.39	3.67	4.07	2.95	3.04
Si	8.86	0.74	4.06	4.80	3.49	4.17
P	9.76	1.10	4.33	5.43	4.00	5.46
S	12.15	2.25	4.95	7.20	4.49	6.93
Cl	15.04	3.63	5.70	9.33	4.95	8.56
K	4.00	0.26	1.87	2.13	1.92	2.42
Ca	5.55	0.20	2.68	2.88	2.88	3.23
Ga	7.82	0.42	3.70	4.12	3.00	3.00
Ge	8.73	0.86	3.94	4.80	3.44	4.05
As	9.28	0.99	4.14	5.13	3.81	5.19
Se	11.19	1.95	4.62	6.57	4.13	6.43
Br	13.40	3.07	5.16	8.23	4.43	7.79
Rb	3.73	0.17	1.78	1.95	1.85	2.33
Sr	5.05	0.18	2.44	2.62	2.44	3.02
In	7.43	0.61	3.41	4.02	2.79	3.00
Sn	8.26	1.03	3.61	4.65	3.12	3.99
Sb	8.56	1.13	3.72	4.85	3.34	4.90
Te	10.13	2.01	4.06	6.07	3.53	5.82
I	11.86	2.98	4.44	7.42	3.76	6.82

[a] Old QEq parameters.

electronegativity of atom A and the angle value of $\angle H_n$A$-O-H$. The angle scale can be regarded as a scale based upon a molecular property which can be measured or computed accurately and interpreted rigorously in terms of the electron-attracting abilities of constituent bonded atoms. It can best be used as a correlational tool for determining the relative electronegativities of electronic ambiguous atoms or molecular groups. Based on the same principle, we have also calculated the molecularly derived IP and EP, which can be used to improve QEq parameters for molecular dynamics simulations.

Appendix D References

1. L. Pauling, *J. Am. Chem. Soc.* **54**, 3570, (1932).
2. L. Pauling, *The Nature of the Chemical Bond*; 3rd ed., Cornell University Press, Ithaca, New York, 1960.
3. J. Malito, *Chimica OGGI Chem. Today* **13**, 57, (1995).
4. V. Shomaker and D. P. Stevenson, *J. Am. Chem. Soc.* **63**, 37, (1941).
5. L. Pauling and D. M. Yost, *Proc. Natl. Acad. Sci. USA* **18**, 414, (1932).
6. K. D. Sen, M. C. Bohm, P. C. Schmit, *Structure and Bonding*, K. D. Sen and C. K. Jorgensen, Eds., Springer-Verlag, New York, 1987.
7. J. Robles and L. J. Bartolotti, *J. Am. Chem. Soc.* **106**, 5482 (1984).
8. For $H \sim He$ 6-31G* basis sets were used; for $Na \sim I$, DZ basis sets and effect core potentials from (a) P. J. Hay and W. R. Wadt, *J. Chem. Phys.* **82**, 270, (1985) and (b) P. J. Hay and W. R. Wadt, *J. Chem. Phys.* **82**, 284, (1985) were used.
9. A. K. Rappé and W. A. Goddard III, unpublished.
10. A. L. Allred, *Inog. Nucl. Chem.* **17**, 215, (1961).
11. A. L. Allred and E. G. Rochow, *Inog. Nucl. Chem.* **5**, 264, (1958).
12. R. T. Sanderson, *Inog. Chem.* **2**, 660, (1963).
13. L. C. Allen, *J. Am. Soc. Chem.* **111**, 9003, (1989).
14. For ionization potentials, C. E. Moore, *Atomic Energy Levels*, National Bureau of Standards Curcular 467, Vol. III, (1958); for electron affinities,H. Hotop and W. C. Lineberger, *J. Phys. Chem. Ref. Data* **14**, 731, (1985).
15. R. T. Sanderson, *Science* **114**, 670, (1951).
16. R. P. Iczkowsky and J. L. Margrave, *J. Am. Soc. Chem.* **83**, 3547, (1961).
17. R. G. Parr and R. G. Pearson, *J. Am. Soc. Chem.* **105**, 1503, (1983).
18. A. K. Rappé and W. A. Goddard III, *J. Phys. Chem.* **95**, 3358, (1991).

19. A. K. Rappé and W. A. Goddard III. *Generalized Mulliken-Pauling Electronegativities*, unpublished work.

20. S. G. Bratsch, *J. Chem. Ed.* **65**, 34, (1988).